MECHANISM OF SOLID ELECTROLYTE INTERPHASE FORMATION ON LITHIUM ANODES STUDIED BY MOLECULAR DYNAMICS SIMULATIONS

A Dissertation

by

SAMUEL BERTOLINI DA SILVA OLIVEIRA

Submitted to the Office of Graduate and Professional Studies of
Texas A&M University
in partial fulfillment of the requirements for the degree of

DOCTOR OF PHILOSOPHY

Chair of Committee,	Perla Balbuena
Committee Members,	Raymundo Arroyave
	Sarbajit Banerjee
	Amine Benzerga
Head of Department,	Ibrahim Karaman

August 2018

Major Subject: Materials Science and Engineering

ABSTRACT

The precipitation of various organic and inorganic products on the Li-metal anode surface, due to electrolyte decomposition, produces a solid-electrolyte interphase (SEI) that controls the battery`s performance. The initial stages of the SEI formation on the Li metal anode surface of lithium-sulfur (Li-S) batteries is studied using First Principles calculations including density functional theory (DFT) and ab initio molecular dynamics (AIMD), and classical molecular dynamics using reactive force fields (ReaxFF).

The reactivity of polysulfides (PS) on the lithium-metal bare surface and on a thin SEI layer covering the anode was studied using AIMD simulations in order to illuminate the degradation of the anode by the PS shuttled from the sulfur cathode in Li-S batteries. The simulations indicate high surface reactivity associated with long-chain PS decomposition on the Li-metal surface. Additionally, the studies suggested a change in reactivity driven by surface orientation. In the presence of a thin SEI layer, the AIMD calculations reveal PS decomposition. The reactivity of PS depends on the nature of the SEI film (e.g. Li_2O, LiF), the thickness, and the exposed facet of the SEI layer. Moreover, the PS reactivity changes while it decomposes over the surface and it can stabilize over a period of time, depending on the SEI species formed. The density of states (DOS) calculations indicates a change in the SEI electronic structure, after PS decomposition.

We investigated the initial formation of the SEI on lithium-metal anodes in presence of several electrolyte compositions using ReaxFF, in absence of a bias potential. We observed the formation of well-defined regions with different density and oxidation states of Li. Dissolution of Li metal atoms results in an uneven distribution of Li in the liquid phase. The electrolyte decomposition mechanism was studied for various electrolyte mixtures. Overall, the reaction mechanisms observed with ReaxFF are in good agreement with previous reports using DFT. However, we found some discrepancies in specific predictions by the ReaxFF that should be addressed in future work.

ACKNOWLEDGMENTS

I would like to express my very appreciation to my advisor Dr. Perla B. Balbuena for her patient guidance, encouragement, continuous support and useful critiques of this research. I would also like to thank the committee members, Dr. Banerjee, Dr. Arroyave and Dr. Benzerga for the support.

I have a special gratitude to the members of Balbuena`s group for the long discussions, sharing their time and helping each other to do a better research. I had a good time with my friends at Texas A & M University and in College Station. Thanks for CAPES for the financial support through Science without Borders. I am really thankful to my family, they have been extremely important in this process, and everyone who has positively contributed to achieving my goals.

CONTRIBUTORS AND FUNDING SOURCES

This work was supervised by a dissertation committee consisting of Prof. Perla B. Balbuena, Prof. Raymundo Arroyave, Prof. Sarbajit Banerjee and Prof. Amine Benzerga from the department of materials science and engineering. Graduate study was sponsored by the CAPES Foundation, Ministry of Education of Brazil, for support as Bolsista da CAPES-Proc BEX 11941/13-8.

TABLE OF CONTENTS

LIST OF FIGURES

FIGURE Page

LIST OF TABLES

1. INTRODUCTION

Lithium batteries (LiBs) have an important economic role, with applications in many different areas, where it is necessary to use a device to store energy. LiBs are used in electronic devices such as cell phones, electric cars, or in renewable power generators[1-7]. In devices based on solar energy, the extra amount of energy produced during the day can be stored in LiBs to be used during the night. LiBs are rechargeable, and during cycling, the electrodes are degraded. After a certain number of cycles, the battery needs to be replaced. Thus, two important aspects of the LiBs are specific capacity and cyclability. The specific capacity is related to the amount of energy that can contain per mass of the electrolyte, therefore if the specific capacity increases, the battery can be used for a longer time without being recharged. The cyclability is related to the battery life, in other words, it is associated with the number of cycles that a battery can have. Therefore the demand is to increase the specific capacity and cyclability of the LiB.

Lithium ion batteries using graphite as anodes are nowadays the most commercialized LiBs, which have a specific capacity of 387 $Wh.g^{-1}$. Lithium-metal anodes have a potential to replace Lithium-ion batteries due to their higher specific capacity of 3860 $Wh.kg^{-1}$ [8-12]. Although lithium-metal anodes have a higher specific capacity, one of the disadvantages that need to be solved, is the formation of dendrites over the anode surface. The space between the dendrites branches is filled by the electrolyte, and the dendrite growth produces a high volumetric expansion of the anode. Thus, the dendrites grow fast in direction of the cathode and may create a short-circuit.

This phenomenon reduces the LiBs life and can produce explosive reactions, creating a hazard environment and even produce flames due to combustion of the non-aqueous electrolyte[13-16].

The lithium metal can transfer electrons to the electrolyte and produce decomposition of the electrolyte. In LiBs, the electrolyte reacts with the bare metal surface due to the narrow stability windows of the electrolyte components. The reactions between the anode and electrolyte happen if the chemical potential of the anode is above the lowest unoccupied molecular orbital (LUMO) of the electrolyte. And the cathode reacts with the electrolyte if the chemical potential of the cathode is below the highest occupied molecular orbital (HOMO)[17]. Some products of the decomposition of the electrolyte remain attached to the surface as insoluble lithium salts or polymers. This mechanism creates a passivate layer so-called solid-electrolyte interphase (SEI), which prevents continuous corrosion of the anode. The components present in the SEI depend on the composition of the electrolyte, but in the most common organic electrolytes (ether base solvents, that include as salts LiTFSI (Lithium bis(trifluoromethanesulfonyl)imide) or lithium trifluoromethanesulfonate(LiTriflate) etc.)[18-22] due to the decomposition of the electrolyte, inorganic and organic salts, such as Li_2O, LiF, $LiCO_2$ and polyofenes[23-40] are formed. The inorganic part of SEI is more stable and is created faster than the organics part of the SEI. However, the organic components of the SEI have a higher diffusion of lithium ions and can better accommodate morphological changes in the SEI[41]. Additionally, in the inorganic part of the SEI, the capacity of transport of lithium atoms can be improved by changing the distribution of the insoluble salts deposited over the

SEI. Consequently, the properties of the SEI can be modified by engineering the electrolyte, through the solvent or through the soluble salts existing in the electrolyte. The composition of the SEI will directly affect the diffusion of lithium ions in the bulk SEI[42]. Thus, the SEI will dictate the behavior of the LiB.

The dendrite formation is directly correlated with the transformations that occur in the SEI. In the conventional model[43,44], initially the electrolyte decomposes over the lithium bare phase, creating a pristine inorganic layer, composed normally of Li_2O, LiF, Li_2S, and Li_2CO_3 (electrolyte composition dependent). The pristine inorganic layer is partially dissolved during cycling and can be replaced by decomposition of the additional electrolyte. The species present in the surface keep decomposing, building new phases in regions closer to the bulk lithium phase; these phases have species with low oxidation states. The continuous precipitation and dissolution of the species on outer layer create a porous phase. The dissolution (oxidation) and deposition (reduction or plating) of lithium, produced when the electric field is applied, produce morphological changes in the anode. At low current density, lithium ions can diffuse through the SEI, and the SEI can adapt to the morphological changes of the anode. In high current density, during discharge, any heterogeneity in the SEI (e.g grain boundary) can create a preferential path for lithium to diffuse. In this situation, the high current density will force lithium to massive diffusion in a specific path and eventually will induce damage to the SEI. During charge at high current, the deposition of lithium in the anode deforms the SEI, which can eventually break, exposing the anode bare surface and creating a site where the dendrite grows. Moreover, at high current charge rates, the time for Li to

deposit is shorter and smaller grains are deposited over the anode than in low current regimes.

Another model proposed for the formation of dendrites in Lithium batteries is the porous phase model[45]. In this model, the anode passes through a morphological change, evolving from a dense phase (bulk lithium metal) to a porous phase. In this porous phase, lithium has an uneven distribution, what will also generate an uneven distribution of the electric field through this phase[46]. Moreover, the density profile of lithium in the SEI is not continuous and increases as it gets closer to the bulk lithium anode. Inside of the porous phase, decomposed species of the electrolyte coexist with intact electrolyte species. The electrolyte consumes the dense phase (bulk lithium metal) to produce a porous phase, consequently expanding the anode's volume. During charge and discharge, a denser phase can be consumed and the porous phase increased. The buildup of this phase will eventually form isolated clusters of lithium metal, forming the so-called "dead lithium". During the stripping process, the SEI is partially oxidized at high oxidation potentials, thus disrupting the SEI and permitting penetration of the electrolyte with Li metal. At high current regimes in the porous phase model, different from the conventional model, the cell failure happens before the dendrite formation. The structure formed over the grains prevents the complete dissolution of the grains.

On the macroscopic aspects observed by Wood[47,48], during the first half-cycle of a Li/Li battery, the dendrites deposit randomly over the cathode and grow faster than new dendrites are nucleated. Also, there is a drop of voltage while the dendrites grow, indicating a reduction in the energy barrier to lithium deposition. When the electric field

is reversed, the dendrites present in the anode (cathode during first half-cycle) start to be dissolved and new dendrites nucleate in the cathode. Due to an energy barrier of dissolution and deposition of lithium in the dendrites, there is a drop of the voltage intensity. Because the dendrites grow in the cathode, the dendrites from the anode can be totally consumed and eventually detach from the anode. Thus the energy barrier for dissolution in the anode increases, also increasing the voltage intensity. Finally, when the available lithium on the dendrites are consumed, other regions of the anode start to be consumed, forming pits on the surface and dead lithium attached to the surface, produced from the partially dissolved dendrite. Once the pits are formed, the voltage intensity again decays. Moreover, pits have a higher energy barrier for dissolution than the dendrite, but smaller than the non-damaged SEI surface.

There are three strategies that can be taken to suppress the dendrite growth in Li-metal anodes. These strategies are based on modifying the separator, the anode, the electrolyte, or the operating parameters of the battery[49]. Moreover, the different approaches can be combined in order to obtain a better result.

The separator is responsible for preventing the short-circuit formation between the cathode and the anode, also the separator allows the transport of ions between them. The interaction between the dendrite growth and the separator happens in different regimes: the suppression regime, where the growth of dendrite is thermodynamically unfavorable; the permeable regime, where the dendrite grows up to the first layer of the separator; the penetration regime, where the dendrite is stable in the channels of the porous separator; and the short-circuit regime, where the dendrite grows beyond the

separator. The regime will be governed by the characteristic of the porous phases and fibers configurations[50]. The current density that passes through the dendrites can overheat locally due to Joule effect, degrading the separator or start runaway reactions with the electrolyte[51,52]. The separator works as a mechanical barrier for the dendrite to grow, but the porous separator still has current intensity limitations. Solid state electrolyte and gel-polymers electrolyte prevent the dendrite formation, but it limits the transport capability of lithium ions. The strategy of using a special separator to mitigate dendrite growth is applied in different experiments and have demonstrated improvement of cyclability when present in the LiBs[53-57].

Another strategy to suppress the dendrite growth is to modify the anode, or by acting on the collector or changing the lithium metal surface. Chi et al. [58] used a foam Ni collector, which form Ni-Li composites on the surface, but also entrapping the dendrites that grew on the porous phase. The disadvantages of changing the collector 3D configuration are: The dendrites can block porous structures of the anode and forbid access to lithium ions to deposit in other regions of the collector; while dendrites still can grow in direction of the cathode. Another way to modify the anode surface is by depositing a coating on the lithium metal surface[59-62] or creating an artificial SEI[63], which will allow a homogeneous deposition of lithium ions. However, once the coating is damaged during the battery cycles, it will again create a preferential path for the dendrite to grow.

The strategies to engineering the electrolyte in order to suppress dendrite growth are: Create an SEI over the anode that will mitigate the dendrite growth; have an

electrolyte that will fast repair a damaged SEI; or act on the path for lithium ions to diffuse. One approach is to use the so-called ionic liquid electrolyte, which includes liquid salts (e.g LiTFSI) that have a good ionic conductivity, non-flammability and can create a passive layer with the anode. The efficiency of the ionic liquid electrolyte can be increased by the addition of ether solvents. Although the ionic liquid electrolyte has a good efficiency to suppress dendrites, it is nowadays economically unviable. The electrolyte can also be modified with additives in the electrolytes and/or controlling the solvent mixture or using different salts. The modification of the liquid electrolyte to form a SEI that will allow a more homogeneous deposition have been used in different ways[19-22,64-72]. The electrolyte can be engineered in a way to generate more elastomers to accommodate morphological changes in the SEI and improve its ionic conductivity, but also having electrolytes whose decomposition products are inorganic salts that have good ionic conductivity.

One important mechanism to prevent dendrite is the self-healing electrostatic shield mechanism (SHES). The cesium ions, preferentially deposit over defective rugosities (protuberances) present in the anode surface, which also represent the nuclei for dendrite growth. It is proposed that a cation will cover preferentially the Li protuberance and form an electrostatic shield over this protuberance preventing further Li deposition and inhibiting a dendritic growth by forcing the Li to deposit in other points. In the SHES mechanism, Cs will deposit preferentially in low coordinated sites, located on the protuberances, where the dendrites grow. The cesium ions, when deposited over the surface, remain with a positive charge. Thus, the Li ions will avoid to

deposit over positively charged sites, therefore inhibiting the dendrites growth from the protuberances. Ding et al. [73] used the salt $CsPF_6$ at 0.05M and low concentration of 1 M $LiPF_6$ /PC and observed that not only it prevents the dendrite to grow, but it also heals dendrites already formed. Although SHES has many advantages, it is still less effective at elevated current densities.

Lithium-metal anode can be used also in lithium-sulfur batteries, with sulfur incorporated in an electrical conductive host such as graphite. Sulfur is a promising material for cathode due to its high theoretical capacity of 2567W.h.kg^{-1}. Nevertheless, the cathode suffers of volume expansion during cycles and polysulfide dissolution[74-77]. During lithiation of sulfur, intermediate salts of polysulfides (PSs), Li_2S_x ($3 < x < 8$), are soluble in ether-based electrolytes and will shuttle in the direction of the anode[22,78]. The PS reacts with the metal, depositing Li_2S, which is insoluble in the electrolyte. The deposited Li_2S can degrade the anode and form a passive layer that will act as an insulator[79-81]. Long polysulfide chains can shuttle back to the cathode and cause self-discharge of the battery[82,83].

The main strategies to reduce the effect of PSs are by modifying the cathode, the separator, or use of additives in the electrolyte. On the strategy of modifying the cathode, the structure of the graphite is important to allow the polysulfides to remain a longer time closer of the cathode and consequently giving more time of PSs to form Li_2S and deposit on the host material. The porosity of the graphite is important to encapsulate the active material. Different structures of the graphite were largely researched on the literature, such as carbon nanotubes, microporous carbon, hollow carbon spheres, etc[84-

[98]. The cathode can also be modified by adding additives or composites such as oxides, which will trap the PSs by adsorption[99-103]; or by encapsulating the host material with a polymer that will allow electrons and Li-ion conductivity[104,105]. The strategy over the separator consists in use membranes that will reduce the transportation of PSs through this material[106,107]. The electrolyte can be modified by adding additives which will produce a passive SEI at the Li metal anode which will act against PSs decomposition. $LiNO_3$ is one additive that has been added to the electrolyte and has passivating effects on the anode against PSs degradation, but also reducing dendrite formation. Decomposition of $LiNO_3$ in presence of PSs, induces a SEI which allows a high ionic conductivity. $LiNO_3$ reacts with the anode and the PSs to form species such as Li_3N, Li_2SO_x ($1 < x < 4$), Li_2O and LiN_yO_x [33,67,71,108,109]. However, due to high reactivity of $LiNO_3$, the additive can be completed consumed or due to continuous consumption of the anode, $LiNO_3$ can degrade irreversibly a huge amount of Li metal.

2. METHODOLOGIES

2.1. COMPUTATIONAL MATERIAL SCIENCE

The goal of computational materials science (CMS) is to understand the behavior and properties of materials by using algorithms, based on physical, chemical and mathematical theories; these algorithms can be implemented in computer software. Because CMS virtually uses the material to describe its properties, some problems such as handling toxicity substances, cost of the product, environmental hazards and others are not part of the CMS. Moreover, CMS can identify atomistic phenomena that cannot be detected by the actual experiments due to resolution or time, such as X-ray diffraction or Transmission electron microscopy. The method to be applied in CMS depends on computational resources, accuracy, and scale to represent the phenomena. Large-scale bulk materials properties can be calculated by finite element analyses and continuum models. Atomistic simulations yielding both bulk and interfacial properties can be carried out by classical molecular dynamics (CMD) and First Principle Calculations. The more accurate is the method, more computationally demanding it is. First Principles can calculate electronic, optical and magnetic properties of the material, chemical reactions, etc. But First Principles, due to their computational demand, can calculate a lower number of atoms when compared with CMD[110].

2.2. CLASSICAL MOLECULAR DYNAMICS

CMD is a good method to calculate structure and mechanical properties, thermal expansion, melting point, phase diagram, defect structure, thermodynamics properties,

diffusion, etc. In CMD atoms are considered as point mass bodies, which interact with each other by creating repulsion or attraction force. The forces between atoms depend on the distance between the atoms and consequently it can create an energy profile that follows the **Equation 2.1**. Given an initial position, the velocity and the interaction forces between atoms, it can describe the time evolution trajectories of the atoms and the energy of the ensemble. The solution of the **Equation 2.1** gives what is called "molecular dynamics" [111].

$$F = ma = m\frac{\partial v}{\partial t} = m\frac{\partial^2 r}{\partial t^2} = \nabla U \qquad \text{Equation 2.1}$$

Where F is the force between atoms, m is the mass of an atom, a is the acceleration, v is the velocity, t is time, r is the atomic position and U is the potential energy as a function of the atomic positions. Each atom interacts with all the atoms around, and the interaction can in principle be represented by pair-interactions, triplets-interactions and so forth, such as in the **Equation 2.2**. The most common potentials used in CMD are Lennard-Jones, Morse, embedded atom method, Tersoff, reactive force fields (ReaxFF), etc.

$$U = \sum_{i<j}^{N} U_2(r_i, r_j) + \sum_{i<j<k}^{N} U_3(r_i, r_j, r_k) + \cdots \qquad \text{Equation 2.2}$$

Once the potential energy is calculated, the integration of Newton`s equation of motion is carried out at each time step usually by the Verlet algorithm[112-115] as described in **Equation 2.3**, **Equation 2.4** and **Equation 2.5**.

$$r(t+\Delta t) = r(t) + v(t)\Delta t + {}^{1}/_{2}\, a(t)\Delta t^{2} \qquad \text{Equation 2.3}$$

$$a(t+\Delta t) = -m^{-1}\frac{\partial U[r(t+\Delta t)]}{\partial t} \qquad \text{Equation 3.4}$$

$$v(t+\Delta t) = \frac{a(t)+a(t+\Delta t)}{2}\Delta t \qquad \text{Equation 3.5}$$

The most computationally demanding part of the CMD calculation is the computation of the forces generated by the potential energy interaction. When the distance between two atoms is long enough, the forces are negligible. Therefore, in order to reduce the number of calculations, a cutoff distance is applied where the potential is tapered. The truncated portion of the potential represents a very small amount of the energy and can be recovered by addition of a constant value [116].

2.3. CONTROLLING MOLECULAR DYNAMICS PARAMETERS

In order to simulate extended materials, it is necessary to apply periodic boundary conditions to the simulated cell. Periodic boundary conditions extend the central cell generating an infinite number of images, identical to the cell, around the simulated cell. The atoms in the cell interact with the atoms of each of the images, and

thus the self-interaction is canceled by symmetry. Since a cell can be represented by 3 vectors, the position of the atoms in the image can be calculated by adding or subtracting the cell`s vector from the atom in the cell[117].

The total energy of the system is calculated by the sum of the potential energy and the kinetic energy. The potential energy is given by applying the force field method to describe all the relevant interactions. As in the experiments, the simulations in molecular dynamics run in a temperature range preset. In agreement with statistical thermodynamics, the temperature can be computed in terms of the scaled velocity of atoms, as in the **Equation 2.6**. The average velocity distribution of particles follows the Maxell-Boltzmann distribution[118]. Thus, the kinetic energy of the system can be calculated by the temperature dependence, accordingly with the **Equation 2.7**. The total energy of the system is the sum of the potential energy and the kinetic energy. The pressure of the system is calculated by the change of the total energy when the volume of the cell changes, as in the **Equation 2.8**.

$$T = \frac{1}{3NK_b}\sum_i^N \frac{1}{2} m_i (v_i . v_i) \qquad \text{Equation 2.6}$$

$$E_{kin} = \frac{3NK_b}{2} \qquad \text{Equation 2.7}$$

$$P = \frac{1}{V}\left[NK_bT - \frac{1}{3}\sum_i^N \sum_{j>i}^N r_{ij} f_{ij}\right] \qquad \text{Equation 2.8}$$

Where T is the temperature, N is the number of particles, K_b is the Boltzmann constant and E_{kin} is the kinetic energy of the system, E is the total energy and P is the pressure.

The parameters of the cell are controlled by thermostat and barostat algorithms, which control respectively temperature and pressure of the system. Different ensembles can be chosen in a molecular dynamics simulations, depending on what type of ensemble is being simulated[111]. The constraints applied on the ensemble allows obtaining particular thermodynamic properties such as entropy, Gibbs free energy, chemical potential, etc. In the microcanonical ensemble (NVE), the number of particles, the volume of the cell and the total energy of the system are held constant over time; in the canonical ensemble (NVT) the number of particles, the volume and temperature remain constant over time; in the isothermal-isobaric ensemble (NPT), the number of particles, pressure and temperature are constant over time; and in the grand canonical ensemble (μVT) the chemical potential, the volume, and the temperature are fixed. The temperature in canonical, isothermal-isobaric and grandcanonical ensembles are controlled by the temperature of the bath. There are several thermostats and barostats to control the ensemble[119-124], and Nose-Hoover is a common thermostat applied in molecular dynamics. The Nose-Hoover thermostat uses a friction parameter to accelerate or slow down the particles` velocity in accordance with the bath temperature, see **Equation 2.9** and **Equation 2.10**. The Hamiltonian energy or the energy function fluctuates, but the total energy of the system and bath are held constant.

$$m_i \frac{\partial^2 r_i}{\partial t^2} = f_i - \xi m_i v_i \qquad \text{Equation 2.9}$$

$$\frac{\partial \xi(t)}{\partial t} = \frac{1}{Q}\sum_i^n m_i \frac{{v_i}^2}{2} - \frac{3N-1}{2} K_b T \qquad \text{Equation 2.10}$$

Where Q is a constant that determines the relaxation of the dynamics of the friction coefficient ξ. The barostat is controled by the motion equations of Shinoda et al. [125], which combine the strain energy proposed by Parrinello et al.[126] and the hydrostatic equations of Martyna et al[127].

2.4. REACTIVE FORCE FIELDS

The ReaxFF describes the energy of the system by summing various energy terms involved in a chemical bond interaction that may allow bond breaking or bond forming and the Equation for ReaxFF was derived for van Duin et al.[128]. The assumption is that bond order can be calculated from an interatomic distance between atoms, and consequently the bond order (BO') will be the contribution of sigma bonds (BO^{σ}), pi bonds (BO^{π}) and double pi bonds ($BO^{\pi\pi}$), as in the **Equation 2.11**.

$$BO'_{ij} = BO'^{\sigma}_{ij} + BO'^{\pi}_{ij} + BO'^{\pi\pi}_{ij} = exp\left[p_{bo1} \cdot \left(\frac{r_{ij}}{r_o}\right)^{p_{bo2}}\right] + exp\left[p_{bo3} \cdot \left(\frac{r_{ij}}{r_o}\right)^{p_{bo4}}\right] + exp\left[p_{bo5} \cdot \left(\frac{r_{ij}}{r_o}\right)^{p_{bo6}}\right] \quad \text{Equation 2.11}$$

The **Equation 2.11** gives an uncorrected bond order, which defines an uncorrected overcoordination function (Δ'_i), given by the difference between the total number of bonds from **Equation 2.11** with the valence bond of each atom, as in the **Equation 2.12**.

$$\Delta'_i = -Val_i + \sum_n^{neighbours(i)} BO'_{ij}$$ Equation 2.12

ReaxFF use a softened function to correct the bond orders of BO'_{ij} and for atoms bearing a lone electron pair, a second overcoordination definition (Δ'^{boc}_i) is used as defined on **Equation 2.13**. This allows atoms which bear lone electron pairs after filling their valence, to separate these electrons and involve them in bonding without obtainining a full bond order function. The softened equations are described in **Equations 2.14-18**.

$$\Delta'^{boc}_i = -Val^{boc}_i + \sum_n^{neighbours(i)} BO'_{ij}$$ Equation 2.13

$$f_1(\Delta'_i, \Delta'_j) = \frac{1}{2}\left(\frac{Val_i + f_2(\Delta'_i, \Delta'_j)}{Val_i + f_2(\Delta'_i, \Delta'_j) + f_3(\Delta'_i, \Delta'_j)} + \frac{Val_i + f_2(\Delta'_i, \Delta'_j)}{Val_j + f_2(\Delta'_i, \Delta'_j) + f_3(\Delta'_i, \Delta'_j)}\right)$$

Equation 2.14

$$f_2(\Delta'_i, \Delta'_j) = exp(-p_{boc1}\Delta'_i) + exp(-p_{boc1}\Delta'_j)$$ Equation 2.15

$$f_3(\Delta'_i, \Delta'_j) = \frac{1}{p_{boc2}} ln\left\{\frac{1}{2}\left[\left(exp(-p_{boc2}\Delta'_i) + exp(-p_{boc2}\Delta'_j)\right)\right]\right\}$$

Equation 2.16

$$f_4(\Delta'^{boc}_i, .BO'_{ij}) = \frac{1}{1 + exp\left(-p_{boc3}\left(p_{boc4}.BO'^{\,2}_{ij} - \Delta'^{boc}_i\right) + p_{boc5}\right)}$$

Equation 2.17

$$f_5\left(\Delta'^{boc}_j,.BO'_{ij}\right)=\frac{1}{1+exp\left(-p_{boc3}\left(p_{boc4}.{BO'_{ij}}^2-\Delta'^{boc}_j\right)+p_{boc5}\right)}$$

Equation 2.18

The correction of the bond order, the correction on the overcoordination (Δ_i) and the bond energy are defined as in the **Equations 2.19-23**.

$$BO^{\sigma}_{ij}=BO'^{\sigma}_{ij}\cdot f_1\left(\Delta'_i,\Delta'_j\right)\cdot f_4\left(\Delta'^{boc}_i,.BO'_{ij}\right)\cdot f_5\left(\Delta'^{boc}_j,.BO'_{ij}\right)$$

Equation 2.19

$$BO^{\pi}_{ij}=BO'^{\pi}_{ij}\cdot f_1\left(\Delta'_i,\Delta'_j\right)\cdot f_1\left(\Delta'_i,\Delta'_j\right)\cdot f_4\left(\Delta'^{boc}_i,.BO'_{ij}\right)\cdot f_5\left(\Delta'^{boc}_j,.BO'_{ij}\right)$$

Equation 2.20

$$BO^{\pi\pi}_{ij}=BO'^{\pi\pi}_{ij}\cdot f_1\left(\Delta'_i,\Delta'_j\right)\cdot f_1\left(\Delta'_i,\Delta'_j\right)\cdot f_4\left(\Delta'^{boc}_i,.BO'_{ij}\right)\cdot f_5\left(\Delta'^{boc}_j,.BO'_{ij}\right)$$

Equation 2.21

$$BO_{ij}=BO^{\sigma}_{ij}+BO^{\pi}_{ij}+BO^{\pi\pi}_{ij}$$

Equation 2.22

$$\Delta_i=-Val_i+\sum_n^{neighbours(i)}BO_{ij}$$

Equation 2.23

$$E_{bond}=-D^{\sigma}_e\cdot BO^{\sigma}_{ij}\cdot exp\left(p_{be1}\left(1-\left(BO^{\sigma}_{ij}\right)^{p_{be2}}\right)\right)-D^{\pi}_e\cdot BO^{\pi}_{ij}-D^{\pi\pi}_e\cdot BO^{\pi\pi}_{ij}$$

Equation 2.24

In order to calculate the lone pair energy, it is necessary to determine the number of lone pairs around an atom. The difference between the total number of outer shell electrons (Val^e_i) and the sum of bond orders gives Δ^e_i as in the **Equation 2.25**. This allows calculating the number of lone pair ($n_{lp,i}$) as in the **Equation 2.26**. As the total

bond order associated with a particular atom causes a lone pair to gradually break up, causing a deviation ($n_{lp,i}$), from the optimal number of lone pairs ($n_{lp,opt}$), as calculated on **Equation 2.27**. This deviation causes an energy penalty of lone pairs calculated on **Equation 2.28**.

$$\Delta_i^e = -Val_i^e + \sum_n^{neighbours(i)} BO_{ij} \qquad \text{Equation 2.25}$$

$$n_{lp,i} = int(\Delta_i^e/2) + exp\left[p_{lp1} \cdot \left(2 + \Delta_i^e - 2 \cdot int(\Delta_i^e/2)\right)^2\right] \qquad \text{Equation 2.26}$$

$$\Delta_i^{lp} = n_{lp,opt} - n_{lp,i} \qquad \text{Equation 2.27}$$

$$E_{lp} = \frac{p_{lp2} \cdot \Delta_i^{lp}}{1 + \exp\left(-75 \cdot \Delta_i^{lp}\right)} \qquad \text{Equation 2.28}$$

When the atom is overcoordinated ($\Delta_i > 0$), an energy penalty should be applied to the system. If the atom contains a broken-up lone pair, the degree of overcoordination is decreased. The correct overcoordination number (Δ_i^{lpcorr}) is changed in agreement with the optimal number of lone pairs, as calculated in **Equation 2.29**. With the correction in overcoordination, the overcoordination energy can be calculated as in the **Equation 2.30**.

$$\Delta_i^{lpcorr} = \frac{\Delta_i^{lp}}{1+p_{ovun3}\cdot exp\left(p_{ovun4}\cdot\left\{\sum_j^{neighbours(i)}\left(\Delta_j-\Delta_i^{lp}\right)\cdot\left(BO_{ij}^{\pi}+BO_{ij}^{\pi\pi}\right)\right\}\right)}$$

Equation 2.29

$$E_{over} = \frac{\sum_j^{nbond} p_{ovun1}\cdot D_e^{\sigma}\cdot BO_{ij}}{\Delta_i^{lpcorr}+Val_i}\cdot\Delta_i^{lpcorr}\cdot\left[\frac{1}{1+exp\left(p_{ovun2}\cdot\Delta_i^{lpcorr}\right)}\right]$$

Equation 2.30

If the atom is undercoordinated, the energy contribution for the resonance of the π-electrons between the undercoordinated atomic centers is calculated by the **Equation 2.31**. Undercoordinated energy is important for the atoms that have partly π-bond character.

$$E_{under} = p_{ovun5}\cdot\frac{1-exp\left(p_{ovun6}\cdot\Delta_i^{lpcorr}\right)}{1+exp\left(p_{ovun2}\cdot\Delta_i^{lpcorr}\right)}\cdot$$

$$\frac{1}{1+p_{ovun7}\cdot exp\left[p_{ovun8}\cdot\left\{\sum_j^{neighbours(i)}\left(\Delta_j-\Delta_i^{lp}\right)\cdot\left(BO_{ij}^{\pi}+BO_{ij}^{\pi\pi}\right)\right\}\right]}$$

Equation 2.31

The angle formed between three atoms has an optimum size, thus the angle energy is associated with the geometric configuration of the atomic arrangements. Thus the penalty energy contribution from the valence angle terms, as well as the bond order in the valence angle goes to zero. The valence angle (Val^{angle}), as described in the **Equation 2.32**, is the same as valence of bond order (Val^{boc}) for non-metals, but applied to the atom j. The equilibrium angle (Θ_0) for the angle formed between three

atoms (Θ_{ijk}) depends on the sum of π-bond order (SBO) around the atom j, as described in the **Equation 2.33**. To avoid singularities a second function that depends on the sum of the π-bond order (SBO2), as calculated on **Equation 2.34a-d**, is used with a constant value ($\Theta_{0,0}$) to lead from 180° to the equilibrium angle as shown in **Equation 2.35**. The equilibrium angle changes accordingly with the sp hybridization around the values 109.47 for sp^3, 120 for sp^2 and 180 for sp. Once the optimum angles are obtained, the softened functions can be calculated as in the **Equations 2.36-37** and used in the **Equation 2.38** to calculate the energy penalty associated with the valence angle energy.

$$\Delta_j^{angle} = -Val_j^{angle} + \sum_n^{neighbours(j)} BO_{ij} \qquad \text{Equation 2.32}$$

$$SBO = \sum_n^{neighbors(j)} \left(BO_{jn}^{\pi} + BO_{jn}^{\pi\pi}\right) + \left[1 - \prod_n^{neighbours(j)} exp\left(BO_{jn}^{8}\right)\right] \cdot \left(-\Delta_j^{angle} - p_{val8} \cdot n_{lp,j}\right) \qquad \text{Equation 2.33}$$

$$SBO2 = 0 \; if \; SBO \leq 0 \qquad \text{Equation 2.34a}$$

$$SBO2 = SBO^{p_{vap9}} \; if \; 0 < SBO < 1 \qquad \text{Equation 2.34b}$$

$$SBO2 = 2 - (2 - SBO)^{p_{vap9}} \; if \; 1 < SBO < 2 \qquad \text{Equation 2.34c}$$

$$SBO2 = 2 \; if \; SBO > 2 \qquad \text{Equation 2.34d}$$

$$\Theta_0 = \pi - \Theta_{0,0} \cdot \{1 - exp[-p_{val10}(2 - SBO2)]\} \qquad \text{Equation 2.35}$$

$$f_7(BO_{ij}) = 1 - exp\left(-p_{val3} \cdot {BO_{ij}}^{p_{val4}}\right) \qquad \text{Equation 2.36}$$

$$f_8(\Delta_j) = p_{val5} - (p_{val5} - 1) \cdot \frac{2 + exp\left(p_{val6} \cdot \Delta_j^{angle}\right)}{1 + exp\left(p_{val6} \cdot \Delta_j^{angle}\right) + exp\left(-p_{val7} \cdot \Delta_j^{angle}\right)} \qquad \text{Equation 2.37}$$

$$E_{val} = f_7(BO_{ij}) \cdot f_7(BO_{ik}) \cdot f_8(\Delta_j) \cdot \left\{ p_{val1} - p_{val1} \cdot exp\left(-p_{val2} \cdot \left(\Theta_0 - \Theta_{ijk}\right)\right)\right\}$$ Equation 2.38

When an atom in a valence angle shares two double bonds, it is necessary to apply a penalty energy to stabilize the system. The softened function, **Equation 2.39**, deals with over or undercoordination to calculate the energy penalty as described in the **Equation 2.40**.

$$f_9(\Delta_j) = \frac{2+exp(-p_{pen3} \cdot \Delta_j)}{1+exp(-p_{pen3} \cdot \Delta_j)+exp(p_{pen} \cdot \Delta_j)}$$ Equation 2.39

$$E_{pen} = p_{pen1} \cdot f_9(\Delta_j) \cdot exp\left(-p_{pen2}\left(BO_{ij} - 2\right)^2\right) \cdot exp\left(-p_{pen2} \cdot \left(BO_{jk} - 2\right)^2\right)$$ Equation 2.40

To calculate the effect of a conjugated system, which connects p-orbitals with delocalized electrons, it is necessary to apply a three-body conjugation term as described in the **Equation 2.41**. The maximum contribution of three-body conjugation is achieved when the bond order is 1.5. This term is used to describe the stability of NO_2 groups.

$$E_{coa} = p_{coa1}\frac{1}{1+exp\left(p_{coa2}+\Delta_j^{val}\right)}\cdot exp\left[p_{coa3}\left(-BO_{ij}+\sum_n^{neighbours(i)}BO_{in}\right)^2\right]\cdot$$

$$exp\left[p_{coa3}\left(-BO_{jk}+\sum_n^{neighbours(i)}BO_{kn}\right)^2\right]\cdot exp\left[-p_{coa4}\cdot\left(BO_{ij}-1.5\right)^2\right]\cdot$$

$$exp\left[-p_{coa4}\cdot\left(BO_{jk}-1.5\right)^2\right] \qquad \text{Equation 2.41}$$

In the same way, as two atoms are associated in bond energy and three atoms define a valence angle energy, four atoms have an energy associated with the torsion angle (w_{ijkl}). The energy is softened by **Equations 2.42-43** to achieve optimum torsion energy, as calculated by **Equation 2.44**, which is influenced by the bond order of four atoms involved in the torsion, as well as in over and undercoordination.

$$f_{10}\left(BO_{ij},BO_{jk},BO_{kl}\right) = \left[1-exp\left(-p_{tor2}\cdot BO_{ij}\right)\right]\cdot\left[1-exp\left(-p_{tor2}\cdot BO_{jk}\right)\right]\cdot$$

$$\left[1-exp\left(-p_{tor2}\cdot BO_{kl}\right)\right] \qquad \text{Equation 2.42}$$

$$f_{11}\left(\Delta_j^{angle},\Delta_k^{angle}\right) =$$

$$\frac{2+exp\left(-p_{tor3}\cdot\left(\Delta_j^{angle}+\Delta_k^{angle}\right)\right)}{1+exp\left(-p_{tor3}\cdot\left(\Delta_j^{angle}+\Delta_k^{angle}\right)\right)+exp\left(-p_{tor4}\cdot\left(\Delta_j^{angle}+\Delta_k^{angle}\right)\right)} \qquad \text{Equation 2.43}$$

$$E_{tor} = f_{10}\left(BO_{ij},BO_{jk},BO_{kl}\right)\cdot sin\left(\Theta_{ijk}\right)\cdot sin\left(\Theta_{jkl}\right)\cdot\left[\frac{1}{2}V_1\cdot\left(1+cos\left(w_{ijkl}\right)\right)+\right.$$

$$\frac{1}{2}V_2\cdot exp\left\{p_{tor1}\cdot\left(B_{jk}^{\pi}-1+f_{11}\left(\Delta_j^{angle},\Delta_k^{angle}\right)\right)^2\right\}\cdot\left(1-cos\left(2w_{ijkl}\right)\right)+\frac{1}{2}V_3\cdot$$

$$\left.\left(1+cos\left(3w_{ijkl}\right)\right)\right] \qquad \text{Equation 2.44}$$

The effect of a conjugated system in the energy conjugation, as done before for three-body interactions, also it needs to be done by four-body interactions. The softened function, **Equation 2.45**, is used to calculate the four-body conjugation energy, as described on **Equation 2.46**.

$$f_{12}(BO_{ij}, BO_{jk}, BO_{kl}) = exp\left[-p_{cot2} \cdot \left(BO_{ij} - 1.5\right)^2\right] \cdot exp\left[-p_{cot2} \cdot \left(BO_{jk} - 1.5\right)^2\right] \cdot exp[-p_{cot2} \cdot (BO_{kl} - 1.5)^2] \quad \text{Equation 2.45}$$

$$E_{tor} = f_{12}(BO_{ij}, BO_{jk}, BO_{kl}) \cdot p_{cot1} \cdot \left[1 + \left(cos^2(w_{ijkl}) - 1\right) \cdot sin(\Theta_{ijk}) \cdot sin(\Theta_{jkl})\right] \quad \text{Equation 2.46}$$

The energy associated with hydrogen depends on the bond-order between the atoms participating of the hydrogen bridge. The hydrogen bond energy is calculated as on the **Equation 2.47**.

$$E_{Hbond} = p_{hb1} \cdot [1 - exp(p_{hb2} \cdot BO_{XH})] \cdot exp\left[p_{hb3}\left(\frac{r_{hb}^0}{r_{HZ}} + \frac{r_{HZ}}{r_{hb}^0}\right)\right] \cdot \sin^8\left(\frac{\Theta_{jkl}}{2}\right) \quad \text{Equation 2.47}$$

ReaxFF predicts that two carbons in a C_2 molecule form a very strong triple bond, while the triple bond is stabilized by terminal radical electrons. This overestimation is corrected by the calculation of C2 correction energy as described on **Equation 2.48a-b**.

$$E_{C2} = k_2 \cdot \left(BO_{ij} - \Delta_i - 0.04 \cdot \Delta_i^4\right)^2 \; if \; BO_{ij} - \Delta_i - 0.04 \cdot \Delta_i^4 > 3$$

Equation 2.48a

$$E_{C2} = 0 \;\; if \;\; BO_{ij} - \Delta_i - 0.04 \cdot \Delta_i^4 \leq 3$$ Equation 2.48b

The triple bond that is possible to form in a CO molecule needs to be stabilized by addition of the triple energy calculation, as described in the **Equation 2.49**.

$$E_{trip} = p_{trip1} \cdot exp\left[-p_{trip1} \cdot \left(BO_{ij} - 2.5\right)^2\right] \cdot \frac{exp\left[p_{trip4} \cdot \left(\sum_k^{neighbours(i)} \left(BO_{ik} - BO_{ij}\right)\right)\right] + exp\left[p_{trip4} \cdot \left(\sum_k^{neighbours(j)} \left(BO_{jk} - BO_{ij}\right)\right)\right]}{1 + 25 \cdot exp\left[p_{trip3}\left(\Delta_i + \Delta_j\right)\right]}$$

Equation 2.49

Beyond the energy attributed to valence interactions which depend on the overlap, there are also repulsive and attractive forces related with van der Waals, Coulomb and the Pauli principle of orthogonalization, which are included in every pair interaction. To eliminate discontinuities in the energy calculation, when charged species move in or out of a non-bounded cutoff distance, a taper correction is added as in the **Equation 2.50**. The van der Waals interactions used in ReaxFF is based on Morse-potential as **Equation 2.52**, and with the inclusion of shielded interactions calculated by the **Equation 2.51**. High repulsions between bonded atoms and atoms sharing a valence angle are avoided. The Coulomb energy is calculated by the **Equation 2.53** which

includes van der Waals forces. The atomic charges are equilibrated based on Electronegativity equalization method [129] (EEM). EEM uses a similar approach to the charge equilibration scheme (QEq-scheme), but uses a more rigorous approach for charge overlap.

$$Tap = 20 \cdot \left(\frac{r_{ij}}{R_{cut}}\right)^7 - 70 \cdot \left(\frac{r_{ij}}{R_{cut}}\right)^6 + 84 \cdot \left(\frac{r_{ij}}{R_{cut}}\right)^5 - 35 \cdot \left(\frac{r_{ij}}{R_{cut}}\right)^4 + 1$$

Equation 2.50

$$f_{13}(r_{ij}) = \left[r_{ij}^{p_{vdW}} + \left(\frac{1}{\gamma_w}\right)^{p_{vdW}}\right]^{p_{vdW}}$$ Equation 2.51

$$E_{vdWaals} = Tap \cdot D_{ij}\left\{exp\left(a_{ij}\left[1 - \frac{f_{13}(r_{ij})}{r_{vdW}}\right]\right) - 2 \cdot exp\left(\frac{a_{ij}}{2}\left[1 - \frac{f_{13}(r_{ij})}{r_{vdW}}\right]\right)\right\}$$ Equation 2.52

$$E_{vdWaals} = Tap \cdot C \cdot \frac{q_i q_j}{r_{ij}^3 + \left(\frac{1}{\gamma_{ij}}\right)^3}$$ Equation 2.53

2.5. FIRST PRINCIPLE METHODS

In quantum mechanics, the dynamics of the particles are described by wave functions accordingly with Schrodinger`s equations. Particles such as electrons are considered as waves, and by Heisenberg principle, the position and momentum of the particle cannot be determined at the same time, also the energy and position cannot instantaneously be measured. Thus operators and eigenvalues have uncertainties

involved on the calculated values. However, the errors involved in the method are higher than the uncertainty existent due to Heisenberg theory[130]. Since the mass of the particles is small, the gravity force can be neglected. Except for heavy atoms, the relativistic effects also can be neglected; moreover, relativism can be incorporated in pseudopotentials for treating core electrons and heavy atoms. Restricting the calculations to the ground-state energy of electrons, the energy during a time-step is calculated as the average energy in a period of time. Because the mass of the nuclei are considerably bigger than those of the electrons, once the nuclei move the electrons adapt to the new ground-state, as proposed by the Born-Oppenheimer approximation. The majority of the methods in first-principles calculations neglect the excited states.

The wave function described by the Schrodinger equation can be expressed by a linear interpolation of exponential functions (eigenstates) with different wave factors, producing a superposition of the wave functions. To solve the Schrodinger equation in a system with several numbers of electrons, it is extremely difficult. The Hartree method brings this problem down, where instead of calculating the interaction of one electron with the other electrons in the system, a mean average field produced by the other electrons with an individual electron is taken into account. The problem of Hartree method is that it does not consider the Pauli Exclusion Principle and the exchange and correlation energies. Different from the Hartree method, the Hartree-Fock method accounts the spin variability and the exchange of energy(when two electrons exchange position). Because the Hartree-Fock method is built in a Slater matrix, it considers asymmetric wave functions. But, the effect of parameters such as Coulomb correlations

is not considered, thus the Hartree-Fock method overestimates the energy of the system. This excess energy is called correlation energy. However, the Hartree-Fock method accounts for some of the correlation energies. The problem is solved by the self-consistent method, where an approximate Hamiltonian is used to solve the Schrödinger equation, obtaining a more accurate set of the wave function. Then with the new set of wave function, another Hamiltonian is generated, until it converges to the approximate correct result.

2.6. DENSITY FUNCTIONAL THEORY

The density of states (DOS) is an energy per volume, that can be extracted from the k-space (k is the wave vector) in a spherical shell parabolic band dispersion relation, as in the **Equation 2.54**. Hence to include the spin the DOS needs to be multiplied by 2, from the density in k-space, giving the DOS as in **Equation 2.55**.

$$\frac{\partial k}{\partial E} = \frac{1}{2}\sqrt{\frac{2m}{\hbar}}\frac{1}{\sqrt{E-V}} \qquad \text{Equation 2.54}$$

$$g(E) = \frac{1}{2\pi}\left(\frac{2m}{\hbar}\right)^{1.5}(E-V) \qquad \text{Equation 2.55}$$

Where $\hbar$ is the Plank constant, V is an external potential, E is the energy and g is the density of state function.

In the Density Functional Theory (DFT) instead of computing all the electron-electron interactions, the electron density is set as a function of functions called Kohn-

Sham orbitals, where the integral of the DOS gives the number of electrons. The DFT energy calculation can be split into kinetic energy, external energy, Hartree energy, exchange energy and correlation energy. The kinetic energy is counted as the non-interactive electrons within the nucleus. The external energy is the interaction of the electrons with other nuclei. The Hartree energy is the interaction between the electron and the mean electron density. The exchange energy is the sum of the four-center integrals as functions of the single-particle orbitals, as described in **Equation 2.56**, given by the exchange between two electrons position, where $\emptyset$ is the Kohn-Sham orbital[131]. The correlation energy is associated with the Coulomb repulsive interaction between electrons changing the overlapping of the electron density. The Kohn-Sham orbitals are built from the electron density and do not have the same physical meaning as the Hartree-Fock orbitals. The antisymmetry is assured by placing the Kohn-Sham orbitals in a Slater matrix. The Kohn-Sham eigenvalue is equivalent to the chemical potentials and represent energies of the orbitals[132].

$$E_X = \frac{1}{2}\sum_{ij}^{n} \int \int \frac{\emptyset_i(r)^* \emptyset_j(r\prime)^* \emptyset_i(r\prime)\emptyset_j(r)}{|r-r\prime|} \qquad \text{Equation 2.56}$$

One way to approach DOS is considering that the electron interacts with the local density of states and thus do not see a change in the derivations on the density of electrons (the density of electrons in locally constant), this is the so-called local density approximation (LDA) method. The LDA can be derived from a homogeneous electron

gas model. LDA works well when applied in the covalent system and simple metals. However, LDA overestimates the bond energy, cohesive energy, bulk modulus and adsorption energy. LDA also underestimates the diffusion barrier and the band gap, gives bad predictions of magnetic behavior, etc. Therefore, LDA does not calculate accurately exchange and correlation energies. The accuracy of DOS calculations can be improved by the generalized gradient approximation (GGA), which considers non-local changes in the density of electrons, but also it considers a semi-localized density of electrons by considering gradient changes on the density of electrons. Methods based on meta-GGA consider not only the first derivative of the density of electrons but also the second derivative, third and so forth. This allows the electrons to have a semi-nonlocal classification. Hybrid functions have a better accuracy on the calculations of energy, where not only higher gradient orders are calculated, but also a certain amount of non-local Hartree-Fock energy.[133] GGA works well with the majority of the systems giving a small amount of error in the energy calculation; it also improves the calculation of energy barrier, cohesive energies, lattice parameters, etc. However, GGA still does not calculate accurately band-gap values. Hybrid functions give better band gap values, which can also be improved with Green functions and screened interactions, accounting consequently many-body interactions[134].

The Kohn-Sham equations are solved by self-interaction, subject to two main constraints: 1) the total number of electrons must be constant (**Equation 2.57**) the Kohn-Sham orbitals must to be orthonormal (**Equation 2.58)**. At the ground state, the electron density corresponds to a minimum in energy. For small systems the Kohn-Sham

equations can be solved by diagonalization of the Hamiltonian matrix; however, the method becomes inefficient when the system is large and it is necessary to apply the pseudo-potential approach. The interactive diagonalization of the Kohn-Sham equations is initialized by superposing the electron density of each atom in its isolated state. The exchange-correlation energy, external potential energy, and kinetic energy are evaluated to build the Kohn-Sham Hamiltonian matrix. After the diagonalization of the matrix, a new set of Kohn-Sham orbitals are calculated and mixed with the old set of orbitals. The interactions stop when the change of energy of the system is small enough, giving the single-point energy by satisfying the "electronic minimization" procedure. Finally, the position of the atoms is updated in agreement with the forces present in the system. The ground-state is found when the force is small enough and then the electronic and ionic minimizations are done.

$$n = \int p(r)\partial r \qquad \text{Equation 2.57}$$

$$\int \emptyset_i^*(r)\emptyset_j(r)\partial r = \delta_{ij} \qquad \text{Equation 2.58}$$

To reduce the computation demand when treating a large number of electrons, mainly in solid structures, the pseudopotentials approach can be used. This approach reduces the total number of electrons by mimicking the potential created by all electrons through a freezing core electrons shell and valence electrons. Therefore, instead of treating n electrons in the core-shell, the electrons in the core-shell are treated as a one-electron function. This is justified because the valence electrons are the ones that interact

with other atoms and are the responsible electrons for bonding formation, conduction, etc. Thus, the valence electrons are treated as n electrons in a pseudopotential. The pseudopotentials are obtained from the all-electron potential, the electrons core shell is fitted to obtain at a specific distance from the nucleus (r_c), the same wave function value, same first derivative and second derivative of the wave function, and consequently guaranteeing correct scattering characteristics and similar energy values at r_c. For distances smaller than r_c the core electrons in the pseudo potential are frozen, nodeless and smooth. For distances bigger than r_c, the all electrons and pseudopotential wave functions are equal and have the same energy. Core potential and valence potential can be treated by the projector-augmented wave (PAW) potential, which maps the core shell and the valence electrons in parts (inter waves and net waves). The core waves are projected on a radial grid and the inter waves are treated by a plane waves expansion. The overlapping after additive augmentation is fitted to the PAW.

When handling materials that can be represented by periodicity in cells with periodic boundary conditions (e.g. solids), electrons are treated in the reciprocal space with the wave vector k and lattice vector. The first Brillouin zone is reduced to the irreducible Brillouin zone and gridded with k-points. When the number of k-points increases, it improves the accuracy because it gives smother wave functions between the k-point, although it is more computationally demanding. The Monkhorst–Pack method allows creating an even grid of k-points. Due to periodicity, accordingly, with Bloch theorem, the pseudopotential can be calculated by the sum of a periodic wave function with the wave vectors. Since the lower energy states are the first to be occupied, it is

possible to use a cutoff energy that can well represent the occupied waves. In some cases, the charge density does not decay smoothly to zero up to the band gap, and the occupancy drops fast, thus the smearing functions with a sigma thickness are used to guarantee a smooth change on the Fermi level. Large smearing gives a wrong energy calculation and small smearing needs a finer k-points mesh. The smearing function can have a Gaussian-type delta function, which creates a fictitious electronic temperature and thus expands the energy levels around the Fermi level[135].

The most common use methods to solve electronic minimization are the Davidson method and residual minimization method (RMM). Davidson diagonalizes a subspace of the matrix instead of the entire matrix, to finally creating the diagonalized matrix is slower then RMM, however, is more reliable. RMM does not direct diagonalize the Hamiltonian but minimizes a residual vector using a precursor matrix. Normally the minimization of the electronic steps can be done by starting with Davidson method and then move to RMM[136].

2.7. OTHER MATHEMATICAL METHODS

The Radial Pair Distribution Function (RPDF) describes the probability to find an atom relative to the ideal gas phase; it describes how density varies as a function of distance, as described in **Equation 2.59**. The RPDF gives how the structure of the material studied is. The RPDF gives an average structure of the material, thus another parameter to characterize the structure of the material is given by the local density profile, which gives the local structure of the material as described in the **Equation 2.60**.

One method that allows obtaining the self-diffusion coefficient is by the mean square displacement (MSD) that can be calculated as in the **Equation 2.61**. The MSD and time parameters have, after stabilization, a linear relation with time; therefore the self-diffusion coefficient is the slope of the MSD over time.

$$g_{ab}(r) = \frac{1}{N_a N_b} \sum_1^{N_a} \sum_1^{N_b} \left(\partial \left(r_{ij} - r \right) \right) \qquad \text{Equation 2.59}$$

$$\rho(z) = \langle \frac{1}{\sqrt{2\pi\Delta z}} \sum_i exp\left(- \frac{(z - z_i)^2}{2\Delta z} \right) \rangle \qquad \text{Equation 2.60}$$

$$MSD = \frac{1}{N} \sum_1^N \left(x_i(t) - x_i(0) \right)^2 \qquad \text{Equation 2.61}$$

3. OBJECTIVES

Lithium batteries are important devices to store energy and are used in many different applications, such as cell phones, cars, renewable power generator, etc. Due to reactions between the electrolyte and the electrode, a passivation layer is formed during battery cycling, which is called solid-electrolyte interphase (SEI). The performance of the Lithium battery is dependent on the structure of the SEI. In other words, the SEI is expected to block further decomposition of the electrolyte and anode dissolution, also it should allow diffusion of lithium atoms to be deposited or dissolve into the anode, and affect the modes of Li deposition, in some cases leading to the formation of dendrites. The goals of this work are to develop a detailed atomistic-level understanding of the initial steps of the SEI formation, as well as details about the electrolyte decomposition, and their influence in the initial stages of dendrite formation. Specific objectives include identifying the distribution of the various SEI chemical components and characterizing models that can better explain the experimentally observed behavior.

4. REACTIVITY OF POLYSULFIDES AND LITHIUM SULFIDE FORMATION ON LITHIUM-METAL ANODE SURFACE[1]

4.1. SYNOPSIS

The precipitation of lithium sulfide (Li_2S) on the Li metal anode surface adversely impacts the performance of lithium-sulfur (Li-S) batteries. In this study, the first-principles approach including density functional theory (DFT) and *ab-initio* molecular dynamics (AIMD) simulations are employed to theoretically elucidate the Li_2S/Li metal surface interactions and the nucleation and growth of a Li_2S film on the anode surface due to long-chain polysulfide decomposition during battery operation. AIMD simulations reveal the role of the anode surface structure and the origin of the Li_2S formation via decomposition of Li_2S_8 polysulfide species formed at the cathode side and dissolved in the electrolyte medium in which they travel to the anode side during battery cycling.

4.2. INTRODUCTION

[1] Reprinted with permission from Luis E. Camacho-Forero, Taylor W. Smith, Samuel Bertolini, and Perla B. Balbuena. "Reactivity at the Lithium–Metal Anode Surface of Lithium–Sulfur Batteries." The Journal of Physical Chemistry C 2015, 119, 26828-26839. Copyright 2015, American Chemical Society.

Reprinted with permission from Zhixiao Liu, Samuel Bertolini, Perla B. Balbuena, and Partha P. Mukherjee. "Li2S Film Formation on Lithium Anode Surface of Li–S batteries." ACS Applied Materials & Interfaces 2016, 8, 4700-4708. Copyright 2016 American Chemical Society

Lithium batteries used in renewable power, electric vehicles and electronic devices to store energy. Conventional Li-ion Batteries have a small specific capacity (150W.h.Kg^{-1}) to supply the demand of higher specific capacity. Lithium-sulfur batteries appear to a promising candidate for the next generation of batteries due to a high energy density of 2567 W.h.Kg^{-1}, low price of sulfur and absence of toxic elements[1,3,64,137-147].

Although Li-S batteries have the prospective capacity to replace Li-ion batteries, there are still critical limitations to surpass. One of the problems to overcome is the shuttle of polysulfides (PS) from the cathode to the anode. The shuttled PS reacts with the anode producing insoluble Li_2S over the surface. This produces a volume expansion, insulate, degrade the lithium-metal surface, consume active lithium metal, and reduce the diffusion of Li-ions. Also, PS can shuttle back to the cathode, producing self-discharge of the battery[79,81,148-156].

We use density functional theory (DFT) and *ab initio* molecular dynamics (AIMD) simulations to characterize surface reactions and reduction mechanisms of the various electrolyte components including the presence of polysulfide species. We hope that a deeper theoretical understanding of the way these species interact will allow real-world Li-S systems to be better engineered to meet and overcome the challenges facing the commercialization of this technology.

4.3. COMPUTATIONAL METHODS AND SYSTEM DETAILS

Investigated in preview studies by Camacho-Forero et al.[27] using DFT calculations, Li-bulk was found to have a lattice parameter of 3.442Å in good agreement

with theoretical values[157,158]. From the Li-bulk, a cleavage on [100], [110] and [111] surfaces was produced and the calculated surface energies were 0.029, 0.031 and 0.033eV/Å, respectively. The solvents studied were 1, 3-Dioxolane (DOL) and 1, 2-Dimethoxyethane (DME) and ethylene carbonate (EC) in presence of 1M Bis(trifluoromethane)sulfonimide lithium salt (LiTFSI). The electrolyte molecules were optimized using the Gaussian 09 (G09) package [159] with a hybrid functional B3PW91 and the 6-311++G(p,d) basis set. [160,161] The anion $TFSI^-$ was optimized for the more stable symmetry, C_2[162-164], where Li coordinates with two oxygen atoms rather than to the nitrogen atom. The density of liquid-phase solvents was estimated by placing randomly of EC (density = 1.32 g/cm^3), and DOL (density = 1.06 g/cm^3) in contact with the model anode surface, respectively.

In our recent report explored by Liu et al.[165], it was investigated the adsorption of Li_2S over a lithium slab model cleavage in the [110] and [111] and the film formation over the anode.

4.3.1. COMPUTATIONAL METHODS OF REACTIVITY OF POLYSULFIDE OVER [110] SURFACE

Calculations were performed using the Vienna *Ab Initio* Simulation Package (VASP). [166-168] Electron-ion interactions were described by the projector augmented wave (PAW) pseudopotentials [169,170] as provided in the VASP databases. The Perdew-Burke-Ernzerhof generalized gradient approximation (GGA-PBE)[171] was selected as the exchange-correlation functional. The energy cut-off for the plane-wave basis expansion

was chosen to be 400 eV. A conjugate-gradient algorithm was employed to relax the ions into their instantaneous ground state. A Gaussian smearing with a width of 0.05 eV was also utilized. For the surface Brillouin zone integration, a 2×2×1 Monkhorst-Pack [172] k-point mesh was used. The convergence criteria for electronic self-consistent iteration and ionic relaxation were set to 10^{-4} and 10^{-3} eV, respectively.

The stability of the solvent in contact with the lithium-metal anode was studied with AIMD-based simulations performed on the optimized model lithium-metal surface in contact with a liquid-phase solvent in the *NVT* ensemble at 330 K using a time step of 1 femtosecond. The Nose thermostat was used to control the temperature oscillations during the simulation with a Nose-mass parameter of 0.5. Both pure solvents and mixtures were investigated. Subsequently, the solvent molecules (liquid-phase) were allowed to relax using a classical molecular mechanism for minimization. For the minimization, the consistent valence force field (CVFF) with a conjugate gradient algorithm as implemented in the Materials Studio software was used[173]. The maximum force among all the atoms in the system required for convergence was set to 0.005 kcal mol^{-1} $Å^{-1}$. Charge transfer was investigated by using the Bader charge analysis[174-176]. In this method, the total electronic charge of an atom is approximated by the charge enclosed in the Bader volume defined by zero flux surfaces. We remark that electronic charges are not observables and the results indicating fractional charges are an artifact of the method.

In order to investigate the effect of PS species present at the anode surface due to the shuttle effect, PS molecules were added to the model electrolyte. The lithiated PS

molecules were optimized using the G09 package software at the same level of theory above-mentioned. In addition, the energy of a neutral Li_2S_8 molecule was first calculated, and subsequently, fragments and potential decomposition products were optimized to evaluate the most thermodynamically favorable reduction pathways. Li_2S_8 molecules were then added to the mixtures of solvents and salt, and the effect of the PS on the electrolyte and its decomposition on the lithium-metal anode were investigated using AIMD.

The AIMD methodology was utilized to determine the reactivity of the electrolyte containing PS species on the model lithium metal surface. Van der Waals dispersion corrections were included using the DFT-D3 approximation by Becke-Johnson [177]. In these simulations, a higher PS concentration (3 M) was chosen in order to clearly identify the Li_2S formation. Finally, we also acknowledge that very long and multiple trajectories should be needed to give definite answers of the mechanisms taking place in these complex chemistries; however, AIMD simulations provide accurate trends that as will be shown complement and illuminate the experimental results. The reactivity of PS over [110] was done by using EC as the electrolyte. The slab was represented by using 3 frozen lithium layers in the middle of the slab in a total of 13 layers symmetric placed.

4.3.2. COMPUTATIONAL METHODS OF REACTIVITY OF POLYSULFIDE OVER [111] SURFACE

For the AIMD simulations carried out using the VASP program, an electrolyte solution is built in contact with a lithium metal surface represented by a metal slab. The electrolyte solvent is 1,3 Dioxolane (DOL) with Bis(trifluoromethane)sulfonimide Li salt (LiTFSI) mixed with a long chain PS, Li_2S_8, at concentrations of 1M and 3M, respectively. Higher concentrations of PS species near the anode have been reported from experiments.[178] A Li metal (110) surface slab in contact with ethylene carbonate (EC) instead of DOL as described in the preview section was used for comparison purposes.

4.4. RESULTS AND DISCUSSION

4.4.1. DECOMPOSITION OF POLYSULFIDE REACTION AND LITHIUM SULFIDE FILM FORMATION

Camacho-Forero et al.[27] studied the reaction path and configuration of PS, calculating the energy dissociation with the B3PW91 method in the gas phase and implicit solvent model. Li_2S_8 can have a different configuration, linear or as a ring, which most stable configuration will depend on the solvent environment. In the gas phase, all the decomposition products of PS are more stable as radical instead of being neutral. However, the behavior changes in implicit solvent, where the neutral species become more favorable and can in some cases as in EC become the most stable species. In AIMD, the decomposition of PS is only observed in presence of the Li metal surface,

thus Li_2S_8 fragmentation does not involve delithiation. Ionic delithiation is more like to occur, while neutral delithiation is unfavorable. The solvent helps to dissipate the charge of the species. AIMD suggest that PS decomposition is random, the PS decompose due to charge transfer from the metal to the electrolyte and occurs almost instantaneous (<10ps).

Liu et al.[165] investigated the formation of Li_2S layer over the lithium metal surface and observed that Li_2S adsorb parallel to the Li [110] surface, bend Li [110] surface, and has a strong interaction with the substrate. S stays in the bridge site of two adjacent Li. While in the Li [111] surface, S interact also with a Li sublayer and located at the fcc hollow sites. The attraction between Li_2S and the Li surface is stronger for [111] surface than [100] surface. On charge density difference calculation, electron accumulation is located between S and Li from the slab; Li_2S acts as an electron acceptor. The energy adsorption of Li_2S increases until the surface is fully covered and the literature demonstrates that Li_2S are preferential on the [111] surface[80,179-181].

4.4.2. REACTIVITY OF POLYSULFIDE OVER [110] SURFACE

AIMD simulations showed that the fragments that result from the decomposition of a long-chain PS such as Li_2S_8 are rapidly reduced on the surface, yielding a compact surface layer. In order to identify the exact composition of this layer, new AIMD simulations were performed on a crystal structure exposing a (110) facet (**Figure 4.1**). The complete decomposition of Li_2S_8 on a pure lithium anode surface is observed within the first 1.3 ps, forming an amorphous Li_2S surface according to the estimated

stoichiometry. Analysis of AIMD trajectories shows that the choice of solvent species (DOL or DME) does not affect the time required for PS decomposition. After the decomposition is complete and counting the number of Li atoms in the neighborhood of each S atom, 80% of the S atoms have between 3 and 5 Li nearest neighbors, using a cut-off of the bond distance of 2.53 Å. In a Li_2S crystal, each bulk S is bonded by 4 Li atoms at a distance of 2.47 Å [182]. Thus, **Figure 4.2** reflects the amorphous nature of the nascent Li_2S phase developing on top of the model Li anode.

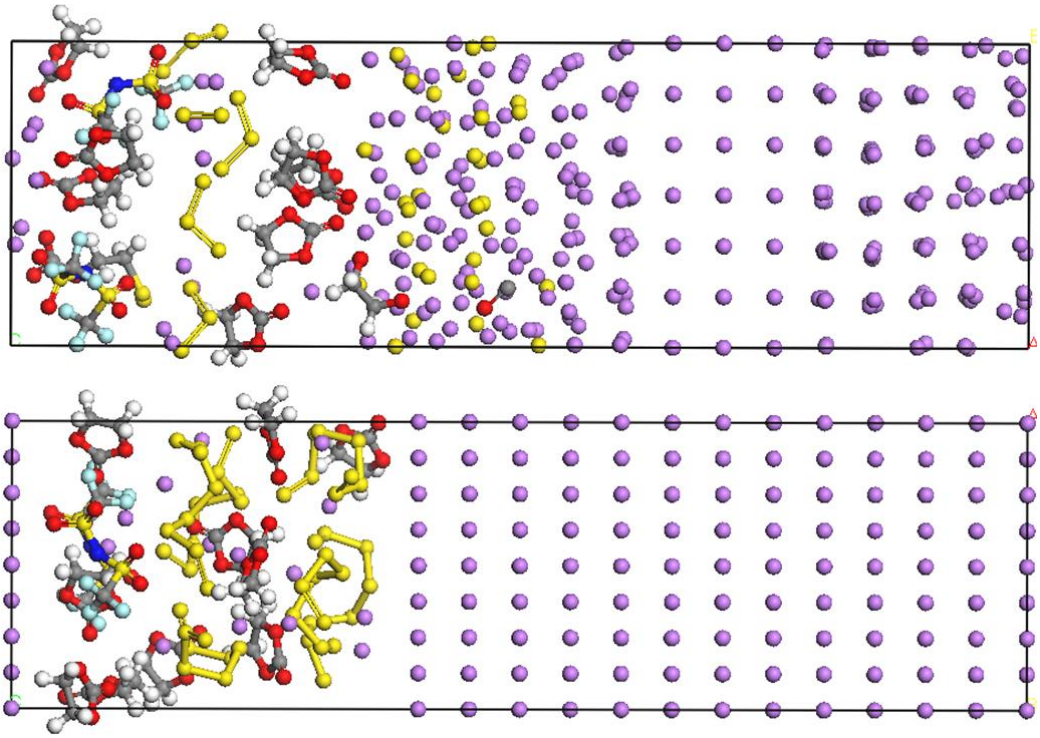

Figure 4.1: Left: Initial configuration of AIMD simulation of 3M PS/Solvent (EC)/1M LiTFSI mixture. Right: Configuration after 15 ps.Color code: Lithium, purple; Oxygen, red; Carbon, grey; Fluorine, light blue; Sulfur, yellow, Nitrogen, blue; Hydrogen, white.

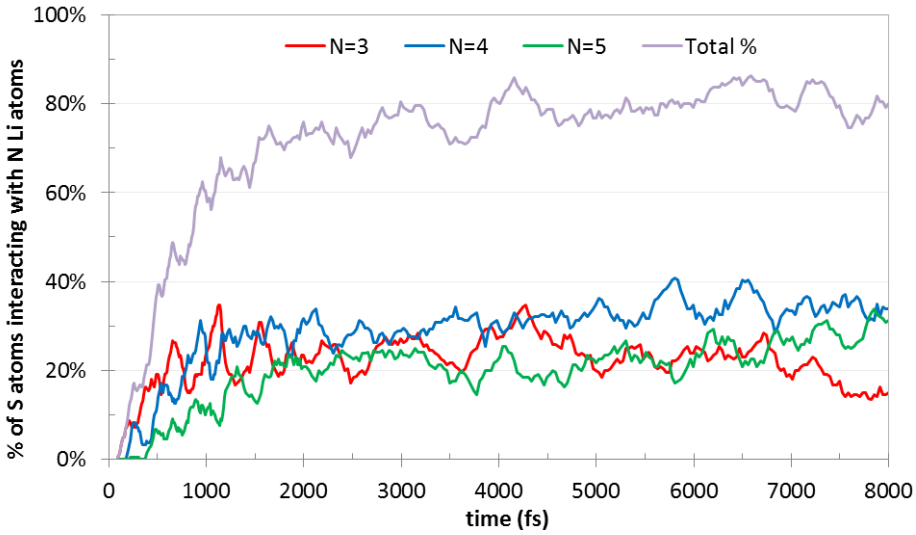

Figure 4.2: Number of Li atoms bonded to a S atom evaluated from the AIMD trajectories of PS decomposition on a (110) Li surface. Note that the decomposition starts after a few fs and after ~ 1000 fs it is practically complete, and the S and Li atoms tend to arrange according to the Li_2S structure and stoichiometry.

Another indicator of the formation of the Li_2S structure is given by the atomic charge of the Li and S atoms. The average charge of the first layer and second layer of lithium atoms is shown in **Figure 4.3**: in both cases, the charges tend to a constant value, although much larger fluctuations are observed in the 2nd layer underneath the top surface. When the outlying values in the 2nd layer are not counted, the charge of the 2nd layer converges to +0.72 |e| at 4 ps, while the charge of the 1st layer converges to +0.82 |e|; after 10ps the 1st and 2nd layer converge to the same value (+0.82 |e|). Moreover, S atoms modify their charge upon reduction until all of them converge to an average value of -1.7 eV, as seen in the charges of a representative Li_2S_8 molecule shown in **Figure 4.4**.

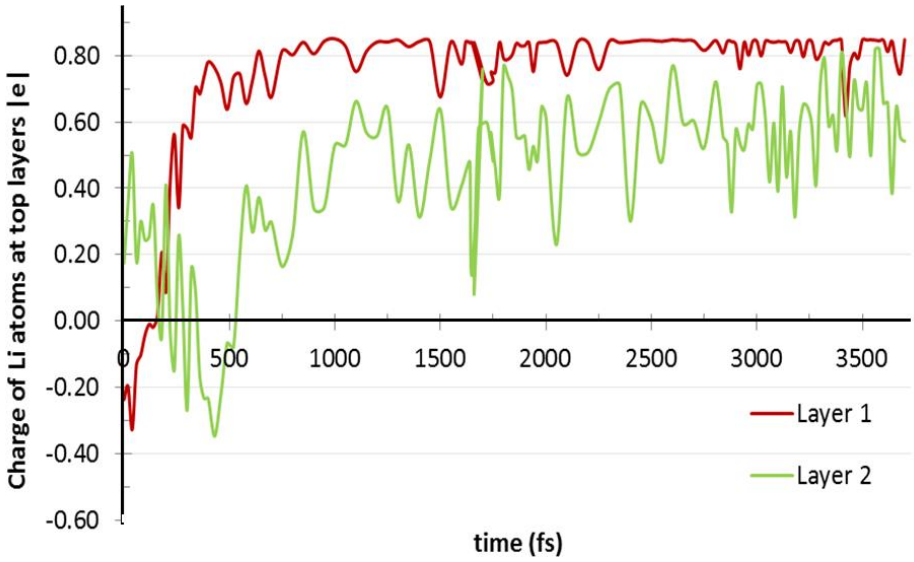

Figure 4.3: Average charge evolution of lithium atoms in surface and 1st subsurface layers of the anode

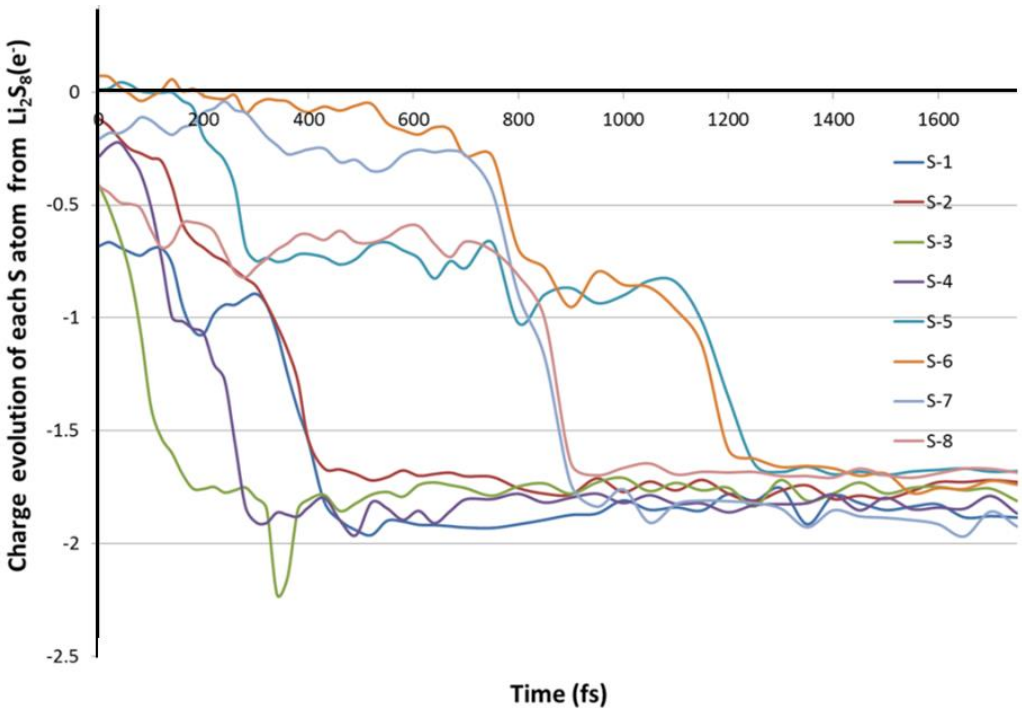

Figure 4.4: Charge evolution of each S atom (labeled 1 to 8) in a Li_2S_8 molecule at the anode surface

The decomposition mechanisms of Li_2S_8 on the surface are a function of the initial positions of each PS molecule in relation to the surface. Three different initial positions were tested with Li_2S_8 close to the surface. The reactions were analyzed based on the time evolution of the chain size (**Figure 4.5**) and also on the time evolution of the charge of each fragment. In all cases, one chain containing five S atoms is formed from the decomposition of the initial chain. S_5 later decomposes into S_3 + S_2, and S_3 into S_2 + S. The mechanism for a S_2 dimer decomposition is the slowest and also is always the last step for the complete PS decomposition. Although the tendency is to reduce the chain size, some mechanisms can involve reconstruction of the PS short chains such as S_3 (see **Figure A.1**).

The plateau in **Figure 4.4** (where the charge tends to a value of ~ -1.8 e) shows charge stabilization occurring for individual sulfur atoms, indicating the end of the reaction decomposition of one PS molecule. This agrees with an accumulation of positive charge on lithium atoms (**Figure 4.3**). The breaking of S-S bonds does not necessarily indicate the formation of two different PS, but in the majority of the cases, there is a cluster formation, where chains share some Li atoms with the anode surface. Cluster formation has been reported to become more stable for more lithiated PS molecules [183,184].

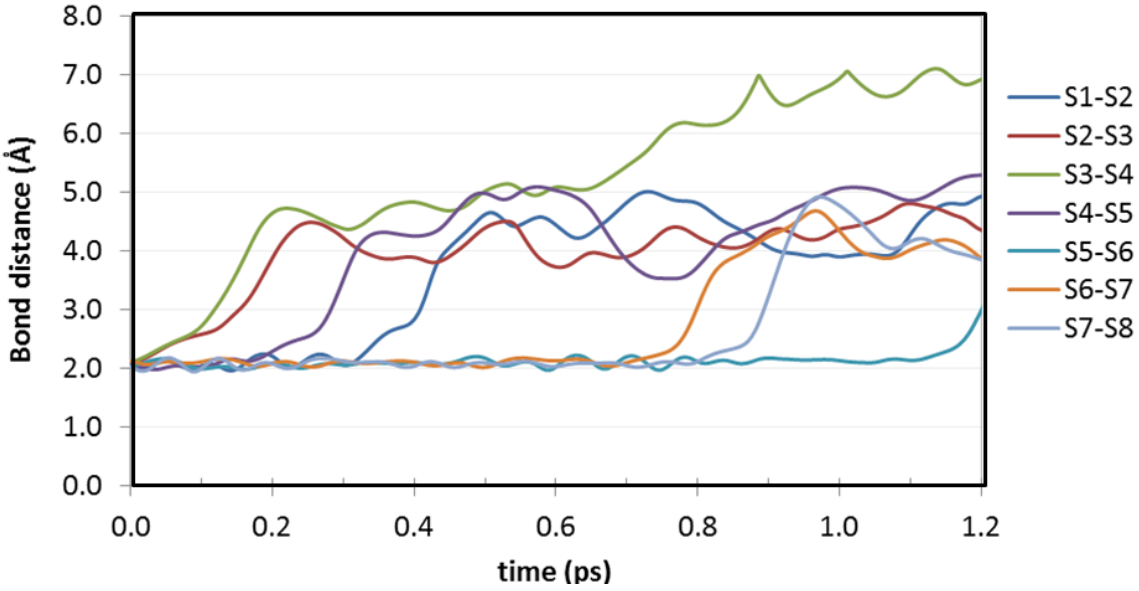

Figure 4.5: Time evolution of S-S bond distances on one Li_2S_8 molecule illustrating PS decomposition at the model anode surface

4.4.3. REACTIVITY OF POLYSULFIDE OVER [111] SURFACE

In the previous section, we analyzed the adsorption and deposition of Li_2S films on Li metal surfaces. In this section, we incorporate the effect of the electrolyte medium where S atoms are generated via decomposition of long-chain PS species on the Li metal surface. AIMD simulations demonstrate rapid decomposition of the dissolved Li_2S_8 species on the Li metal surface. **Figure 4.6** shows the dynamic evolution of Li and S atoms over the first 6.5 ps of simulation time for the Li (111) and Li (110) surface slabs. In order to analyze the results, the PS species were followed in two different groups, molecules closest to the surface (around 5Å) and those farther from it (around 10Å). Similarly, different colors were employed to characterize the trajectories of the Li atoms belonging to the anode (colored purple) and those of the electrolyte (green). On both surfaces the PS species closest to the surface react very rapidly with the Li metal,

tending to form an amorphous Li_2S layer over the outermost layers of the anode, while the farthest PS species stay in the electrolyte phase for longer time and form clusters with other intact or fragmented PS species stabilized by Li ions from LiTFSI and from the original Li_2S_8 molecules.

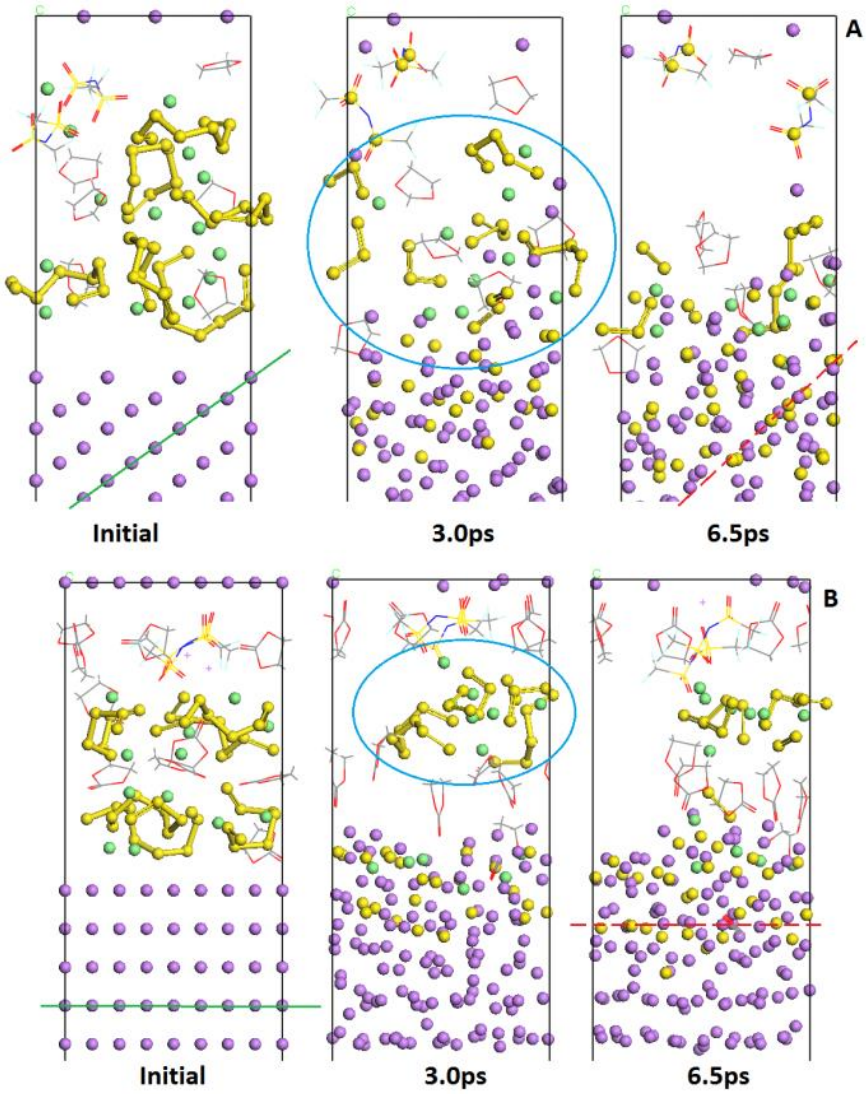

Figure 4.6: Snapshots of the dynamic evolution PS decomposition in contact with Li (111) surface slab (A) and Li (110) surface slab (B). Here, purple, green and yellow spheres represent Li from anode, Li from electrolyte and S atoms, respectively. The DOL solvent is represented in a line display style where O (red) and C (gray) atoms are shown. Green lines indicate the respective crystallography plane; red dashed lines show

the orientation where S atoms tend to accommodate; the blue circle shows where the cluster is localized.

However, the structure of the exposed Li metal facet affects significantly the initial stages of the PS decomposition. On the Li (110) surface slab (**Figure 4.6B**), although initially very fast, the total decomposition of PS species closest to the anode is slower than that on the (111) facet (**Figure 4.6A**) occurring within the initial 4.5 ps of simulation time. This is mainly attributed to a higher amount of S anions and radicals produced by the initial fast decomposition on the (110) facet that accumulates and start Li_2S nucleation on the surface leaving a lower number of exposed active sites available for reaction. In contrast, on the more open (111) facet the reaction is slower initially and the decomposed S atoms migrate easily into the subsurface where they start forming Li_2S. Thus, after the closest PS molecules were reduced, Li atoms from the surface were observed to diffuse in the direction of the electrolyte phase reducing other PS molecules and stabilizing the fragments located farther from the surface. On the (110) facet, after the group of molecules closest to the surface become completely reduced, PS clusters (blue circle in **Figure 4.6** bottom) become stabilized in the electrolyte phase for longer times. Cluster formation is observed mainly after short PS chains ($S < 4$) have been formed as a result of PS decomposition. In these clusters, short S chains share Li atoms, as observed in previous studies.[183-185]

During the initial Li_2S_8 decomposition step, the PS chain reacts with two Li atoms and in most cases, it was observed to break into Li_2S_3 and Li_2S_5. However, this bond scission can also occur simultaneously with another S-S bond of the PS. The

subsequent steps depend on the surface charge transfer, availability of Li atoms and the position of the PS species.[186] Additionally, some reactions may allow a chain to increase (e.g. **Figure 4.7**, S5-S9 bond).

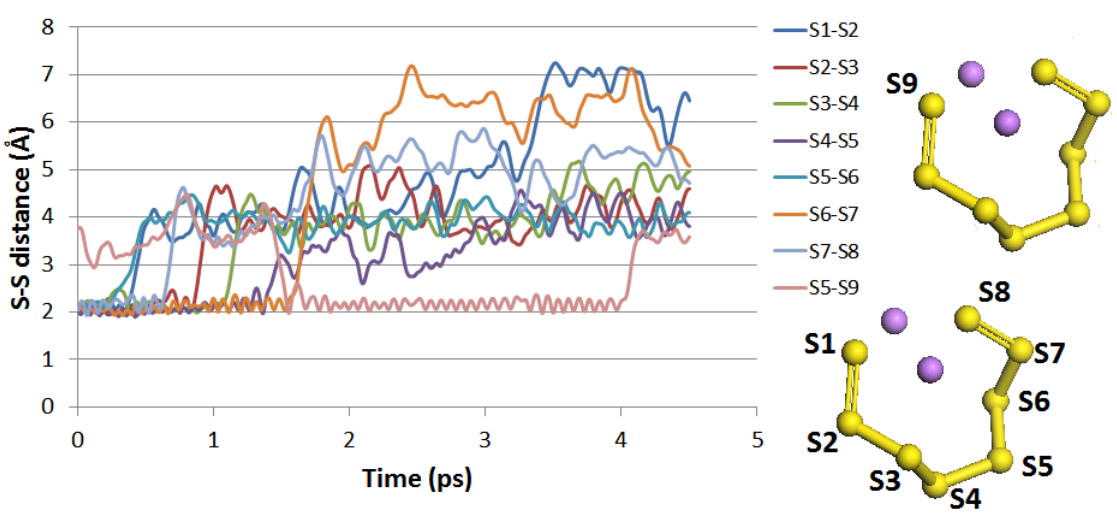

Figure 4.7: Time evolution of a PS decomposition on the Li (111) surface slab. A common shared characteristic is the first bond to break (S3-S4 or S5-S6), while the others depend on the initial position of the polysulfide and surface structure. Reconstruction of the chain can occur, which can be intra- or inter PS (e.g S5-S9).

Bader charge analysis was performed on individual S atoms that belong to a PS species (labeled as in **Figure 4.7**) that completely decompose over the (111) facet. Initial charge accumulates on the S atoms that are located at the ends of the chain, while the other S atoms are almost neutral, with the end S atoms bearing an average charge of -0.67|e| and the remaining S atoms having a charge of -0.08|e|, this difference is due to the direct bond between edge S (S1 and S8) atoms with Li atoms, while the other S atoms (from S2 to S7) are bonded only with S atoms. The Bader charges of S atoms converge to an average value of -1.75|e| for the (111) surface (**Figure 4.8**), as reported

earlier on the (110) surface [186]. It is interesting to note that on both facets, the charge on the surface Li atoms converge faster to a value of approximately +0.80|e|, indicating the formation of Li_2S. The main difference on the Li_2S films that cover each surface is the alignment of S atoms relative to the surface, as seen in Error! Reference source not found.**4.6**. S atoms tend to take the same orientation (red and dashed lines on **Figure 4.6**) of the crystallographic planes, represented by the green lines in **Figure** Error! Reference source not found.**4.6**. It is important to remark that an amorphous structure is observed, given the short time that does not allow the surface to organize. For this reason, a direct comparison with the structures of the Li_2S film[165] is not possible. We note that the surface with a higher surface energy is always more active to interact with adsorbates. In previous work[186] we calculated the surface energies of the Li(110) surface as 0.031 eV/Å^2 and 0.033 eV/ Å^2 for the (111). Hence the (110) surface is slightly more stable than the (111) surface. The more active (111) surface interacts more strongly with Li_2S (adsorption energy of -3.57 eV) than the (110) surface (-3.22 eV). Additionally, the more active (111) surface also facilitates the decomposition of Li_2S_8 to Li_2S as shown by the AIMD simulations. Overall, there are no significant differences in the time for PS decomposition in different solvents. The high reactivity of the Li metal overcomes any other possible interaction for example solvation effects of the Li ions in the proximity of the metal surface.

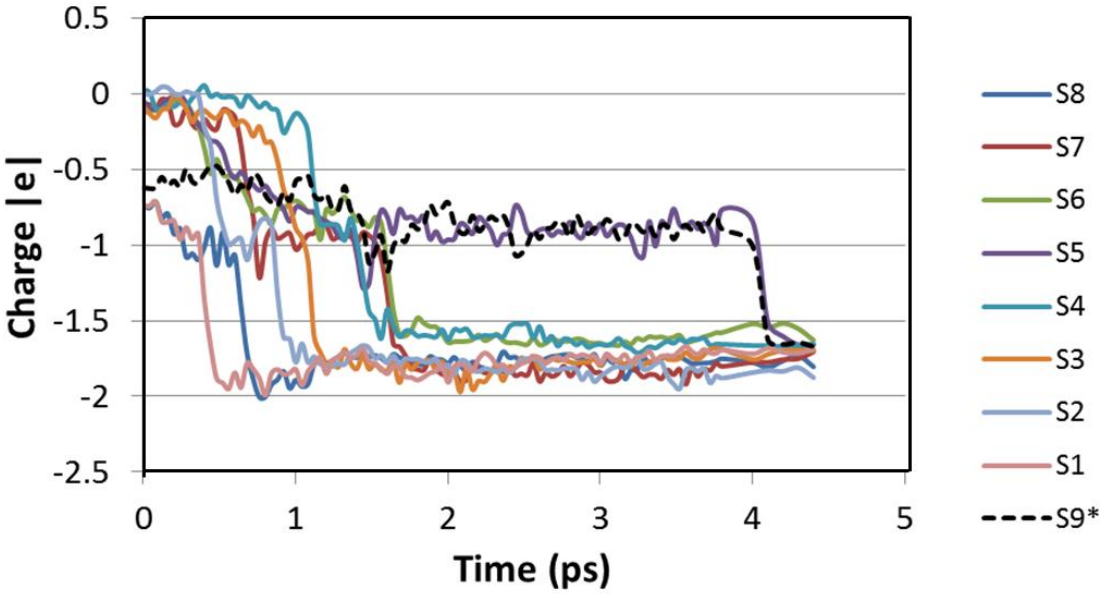

Figure 4.8: Time evolution of the Bader charge of individual sulfur species initially present on the same PS, which completely dissociate by 4.5 ps of simulation time on the (111) surface. S9* represents one S atom from another PS.

4.5. CONCLUSION

The primary method of Li_2S_8 fragmentation away from the anode surface does not involve delithiation; however, the most favorable pathway includes the reaction of the lithiated PS with additional Li atoms, in the gas phase or in presence of the solvent, with four different fragmentation modes found having similar (very favorable) ΔGs of reaction. In contact with the anode surface, the long-chain PS species is completely decomposed despite the solvent used or the PS initial geometry (ring or linear), resulting in the formation of a Li_2S layer that was characterized by analyses of bond distances and atomic charges.

Both the interaction energy analysis and electronic structure analysis suggest that the Li_2S film interacts with the Li anode surface via strong chemical bonds, and the

decomposition of Li_2S film is difficult. The effect of the electrolyte and finite temperature are incorporated via AIMD simulations. Details about the decomposition of Li_2S_8 are followed by analyses of S-S bond distances and charges on the S atoms, both indicating the formation of the Li_2S film. The structure of the Li surface is shown to affect the way the molecules decompose and the rate of Li_2S formation: on the (110) surface although a very fast decomposition is detected initially, the large amount of S atoms interacting with the Li surface atoms impedes the access of new molecules to exposed active surface sites; in contrast the (111) surface let S atoms to go into the subsurface where Li_2S is formed.

The conclusions of this study suggest that inhibiting Li_2S formation strategies should come from various fronts: a) based on new electrolyte formulations that equivalently to the role of $LiNO_3$ would be able to generate a passivation layer that avoids or at least moderates Li_2S decomposition; b) actual modifications to the Li metal surface including physical barriers for diffusion of the long-chain polysulfide species; c) retention of PS species at the cathode via composite electrodes providing physical or chemical barriers to mass transport and/or electrolyte formulations. Successfully implementing these strategies requires a thorough understanding of the chemical, mechanical, and electrochemical implications occurring in the various parts of the Li/S battery, which is the main consequence of this much-interconnected chemistry.

5. EFFECT OF SOLID ELECTROLYTE INTERPHASE ON THE REACTIVITY OF POLYSULFIDE OVER LITHIUM-METAL ANODE[2]

5.1. SYNOPSIS

Lithium metal anodes covered by a thin (6 to 10 Å) solid electrolyte interphase (SEI) film at its initial nucleation stage modeled as a single component (Li_2O, LiF, Li_2SO_4, and Li_3N) are examined with density functional theory and ab initio molecular dynamics simulations. The combined metal anode/SEI surfaces are exposed to an electrolyte containing salt, solvent, and lithium polysulfides. The polysulfide species are found to be easily reduced by the metal slab, even in the presence of the model SEI films. Although the chemical nature of the film and geometry of the exposed facet induces different decomposition kinetics, the reaction mechanisms are shown to be similar for the various SEI models, and end with the formation of Li_2S on the surface of the anode or inside the SEI film. The density of states of the films at this nascent stage of SEI formation in contact with the Li metal surface are very different than those of the bulk crystals, usually showing new intermediate states between the metal and conduction bands, which suggests a change to an electronically conductive character that favors continuous reactivity.

[2] Reprinted with permission from Samuel Bertolini and Perla B. Balbuena. "Effect of solid electrolyte interphase on the reactivity of polysulfide over lithium-metal anode." Electrochimica Acta 2017, 258, 1320-1328. Copyright 2017 Elsevier Ltd.

5.2. INTRODUCTION

The use of batteries and the demand of higher battery performance have grown with the use of electronic devices and hybrid/electric cars [1]. Due to their high theoretical specific energy of ~2600 Wh/kg, lithium-sulfur (Li-S) batteries have a promising potential to replace Li-ion batteries (LIBs), which have a specific energy of ~180 Wh/kg[1]. However, Li-S batteries still have several problems including low electronic conductivity of sulfur in the cathode, polysulfide migration or shuttle from cathode to anode, and low stability of the Li metal anode. Lithium polysulfide (PS) species form at the cathode surface during discharge. Some of the PS are soluble in the electrolyte and shuttle from cathode to anode causing degradation of the Li-metal anode and posterior failure of the battery[147,187-189]. The Li-metal anode instability results in dendrite formation, which can cause a short circuit when the dendrite reaches the cathode, heating up the battery and leading to safety issues[190]. The low electrochemical stability of the electrolyte leads to its decomposition at the Li metal surface yielding Li_2CO_3, LiF, Li_2O, Li_2S, Li_3N, and Li_2SO_4 among other products. These decomposition products nucleate, grow, and eventually form a solid-electrolyte interphase (SEI) layer[191,192] that is usually described as composed of an inner inorganic layer and an outer more porous-like organic layer [193-198]. The SEI layer plays an important role due to its potential to reduce the effects of anode degradation and dendrite formation.[199] $LiNO_3$ has been successfully used as an additive to protect the anode against PS attack and dendrite formation, creating a protective SEI during its decomposition on the anode.[109,200-202] Similar beneficial effects have been attributed to the utilization of a protective artificial SEI layer

composed of Li_3N.[63] $LiNO_3$ in the presence of PS forms a protective SEI layer against PS decomposition[195,203], not observed in electrolytes that do not contain both $LiNO_3$ and polysulfide.

Although the SEI layer is expected to be electronically insulating, therefore a barrier to electron transfer, this may not be the case at the initial stages of nucleation. This is because the structures formed are not "bulk" crystals that would be electronic insulators. Thin films and small clusters can have very different electronic configurations than their bulk counterparts. Changes in electronic conductivity observed in some bulk insulator materials, such as TiO_2, SnO_2, and ZnO, which become semiconductors in ultra-thin films,[204-207] corroborate the assumption that quantum confinement effects may occur in thin SEI films at their nucleating stages (~1nm) covering the lithium metal anode. This is analyzed in this work through the analysis of the density of states and the existence of reactions requiring electron transfer at their surfaces. The ability to conduct electrons of some SEI components nucleated as imperfect crystals or films is one of the reasons why the SEI keeps growing and becomes very thick, up to hundreds of nanometers.

The tremendous impact of first-principles computational studies in advancing many areas of science and engineering of materials, and specifically related to energy storage components[208] is well known. Recently, the effects of various facets on the reactivity of the long-chain polysulfides over the Li-metal anode have been studied.[165] In particular, for the problem of decomposition of polysulfides on Li-metal surfaces and the formation of a multicomponent SEI film ab initio molecular dynamics (AIMD)

predictions[186] were recently confirmed by XPS experiments.[209] It was found that independently of the exposed facet, Li_2S is easily formed on the Li-metal surface due to the decomposition of Li_2S_8 or Li_2S_6 species. Here, to understand how the nature of the exposed SEI layer could affect the decomposition of the PS species, model SEI layers of different compositions emulating the initial nucleation stages were computationally deposited on the anode surface and simulated using AIMD and density functional theory (DFT). A 1,2Dioxolane(DOL)electrolyte containing a Li_2S_8 and Bis(trifluoromethane)sulfonimide lithium salt (LiTFSI) at a 1M concentration were computationally added on top of the SEI layer-covered model anode. The time evolution of the system was investigated using AIMD simulations. The objective is to observe and characterize the behavior of long-chain PS degradation when a thin SEI layer covers the anode surface, aiming to elucidate the effect of the chemical nature of the SEI layer.

5.3. COMPUTATIONAL METHODS AND MODELS

DFT[210,211] calculations within the plane-wave basis set approach[212,213] were performed using the Vienna Ab-initio Simulation Package (VASP).[214,215] A 2×2×1 Monkhorst-Pack k-point mesh[172] was employed to generate k-point grids for the Brillouin zone (BZ) sampling. A 400 eV energy cut-off for the plane-wave basis set is used to achieve both computational accuracy and efficiency. Electron-core interactions were described by the PAW pseudopotentials[169,170] as provided in the VASP database. A conjugate-gradient (CG) algorithm was employed to relax the ions into their ground state. A Gaussian smearing with a width of 0.05 eV was also utilized. The convergence

criteria for self-consistent electronic iteration and ionic relaxation were set to 10^{-4} eV and 10^{-3} eV, respectively. The Li_2S_8 PS species was optimized in the presence of DOL, and van der Waals (vdW) dispersion corrections were included using the DFT-D3 approximation by Becke-Jonson.[177] The DOL molecule was optimized using the Gaussian 09 (G09) package [159] with a hybrid functional B3PW91 and the 6-311++G (p, d) basis set.[160,161] AIMD simulations were carried out in the NVT ensemble at 330 K using a time step of 1 femtosecond. The Nose thermostat was used to control the temperature oscillations during the simulation with a Nose-mass parameter of 0.5.[216-218] A charge analysis is done using Bader calculations, and the Li metal lattice parameter was set to 3.442 Å as calculated in our earlier study.[186]

To represent the anode a 3x3 supercell was used, and the metal was cleaved in the [100] direction. The three bottom layers were fixed to represent the bulk, and the three top layers were allowed to move during the AIMD simulations. One-component thin SEI layers consisted of Li_2O, LiF, Li_3N and Li_2SO_4 respectively. To construct the films, the crystal structures of these materials were cleaved along the [100] and [110] directions. The thickness of the SEI layer between the metal and the electrolyte was modeled to be around 6 Å. The lattice parameters of the inorganic species before surface cleavage are shown in **Table 5.1**. The next step was to perform a geometry optimization of the system to minimize the mismatch between the model SEI film and the Li-metal surface. Then, the electrolyte solution containing a 1M concentration of PS and LiTFSI in DOL was added to the system. To keep the same configuration and position between PS and anode, a molecular mechanics optimization of the electrolyte was first performed

over the surface, keeping the PS, SEI film, and anode atoms frozen. Periodic boundary conditions replicate the anode surface on the top of the simulation cell. To mitigate this effect a fixed monolayer of Helium atoms is included at the top of the simulation cell (the layer was cleaved at the plane (110) of solid He)[219], and a vacuum of 5 Å was left between the anode and the He monolayer. Use of a helium monolayer as a physical barrier to mitigate periodic boundary conditions has already been applied in the literature in a model lithium-ion battery system[220]. The same methodology was applied to a thicker 10 Å SEI layer over the anode, but the cleavage planes ([100] and [110]) were chosen according to the results observed in a thinner SEI layer calculation, as will be described in the results section. Density of States (DOS) were calculated using the Perdew-Burke-Ernzerhof (PBE) functional[171], including the hybrid functional Heyd-Scuseria-Ernzerhof (HSE06) screened Coulomb hybrid density functional as implemented in VASP[221-223]. The exchange part in the HSE06 hybrid functional consists of 25% from Hartree−Fock and 75% from GGA-PBE contributions. The range separation parameter in our calculations with the HSE06 functional was chosen as 0.2[224].

Table 5.1: DFT (using PBE) optimized lattice parameters of crystals used as model SEI layer components.

System*	Space Group	Lattice parameters					
		a (Å)	b (Å)	c (Å)	α (°)	β (°)	γ (°)
Li_2O [225]	Fm-3m	4.574	4.574	4.574	90.0	90.0	90.0
Li_3N [226]	p6/mmm	3.676	3.676	3.836	90.0	90.0	120.0
LiF [227]	Fm-3m	4.028	4.028	4.028	90.0	90.0	90.0
Li_2SO_4 [228]	p121/a1	8.063	4.877	8.336	90.0	107.8	90.0

* The crystal structures were taken from the reference indicated after the respective formula.

5.4. RESULTS AND DISCUSSION

5.4.1. THIN SEI LAYER OVER LI ANODE SURFACE

It has been reported that some additives such as $LiNO_3$ directly affect the PS decomposition, as well as dendrite formation[203] and different structures and compositions of the SEI layer will be formed due to decomposition of the respective salts and additives present in the electrolyte. This was the rationale behind the various models shown in **Figure A.2**. The chemical nature of the SEI layer has a direct impact on the protection against the PS decomposition, since the SEI layer may allow faster or slower transfer of charge from the anode to the PS, inducing their decomposition or passivating the anode. It is expected that the increase of the SEI layer thickness would reduce the reactivity of the PS over the anode, due to a decrease in the film electronic conductivity. Besides the thickness effect, the electronic conductivity may be affected due to the stress present in the SEI film due to the interfacial mismatch, which may create traction or compression. For simplicity, the deformation of the SEI layers was calculated based on the area deformation defined by the **Equation 5.1**, instead of being split into two different dimensions. Area deformation can be used in the analysis of PS decomposition because of the similar values of the lattice vectors of the cleaved surface and also because of the absence of shear deformation. The exception is the case of the Li_2SO_4 [110] facet, where due to the presence of the 105° angle between the two plane vectors, instead of 90° (as in the Li cleavage facet), there is a shear deformation. In Equation 1, D is the area deformation; *a* and *b* are the parameters of the lattice vectors for the SEI film and Li cells.

$$D = \frac{(a_{SEI} \times b_{SEI}) - (a_{Li} \times b_{Li})}{(a_{Li} \times b_{Li})}$$ **Equation 5.1**

During optimization, there is a slight variation in the film thickness with respect to that of the initial optimization, as shown in **Table 5.2**. However, we analyze them considering that for each material the film thicknesses are of comparable size. Surface reactivity is estimated on the basis of the percent of the total PS species that are reduced after 10ps. Taking this estimate, **Table 5.2** shows that for LiF and Li_2O the [100] films are less reactive than [110] ones, and the same trend is found for Li_3N although in this case, the reactivity on both facets is comparable. In contrast to Li_2SO_4, **Table 5.2** suggests higher reactivity on the [100] compared to the [110] facet. This could be due to several reasons including stress, but also electronic and geometric structure (**Figure 5.1**). On the other hand, the magnitude of the area deformation (**Table 5.2**) does not show a clear correlation with the reactivity. The influence of the facet structure on the PS decomposition is also shown in **Figure 5.2**. The simulation cell contains one PS molecule; therefore, a maximum number of seven S-S bonds can be broken. The time evolution of these bonds is followed in **Figure 5.2**, indicating that the most stable facets according to these data are the [100] LiF and the [100] Li_2O facets. Interestingly, these are the facets with the most open structure (**Figure 5.1**) which also expose the electronegative O and F atoms.

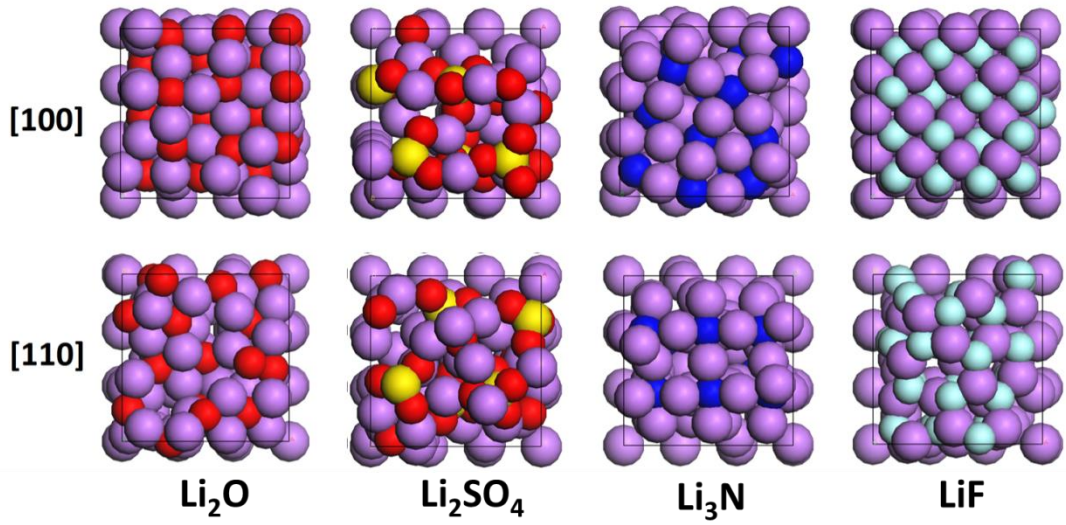

Figure 5.1: Top view of the structure of the exposed facets after DFT optimization in contact with the Li metal anode surface. Color code: Li: purple, O: red, S: yellow, N: blue, F: light blue.

Table 5.2: Area deformation at the interface anode/SEI layer according to Equation (1). Structures of the facets are shown in **Figure 5.1**. Although for each model film there is a slight variation of the thickness as indicated, the average thickness ranges between 6 and 7 Å. The reactivity of the electrolyte in the presence of thin SEI layers along specific facets is characterized by the percent of PS reduced after 10ps.

SEI layer	Facet	Thickness (Å)	Area deformation on XY plane (eqn. 1)	Percent of the PS reduced after 10ps (|e|)
Li_2O	[100]	7.1	-0.103	34.9
	[110]	6.2	-0.155	91.9
Li_3N	[100]	7.8	0.204	84.3
	[110]	8.5	0.390	91.3
LiF	[100]	8.2	0.369	32.6
	[110]	6.3	0.291	58.4
Li_2SO_4	[100]	6.2	-0.217	93.9
	[110]	5.9	0.253	58.2

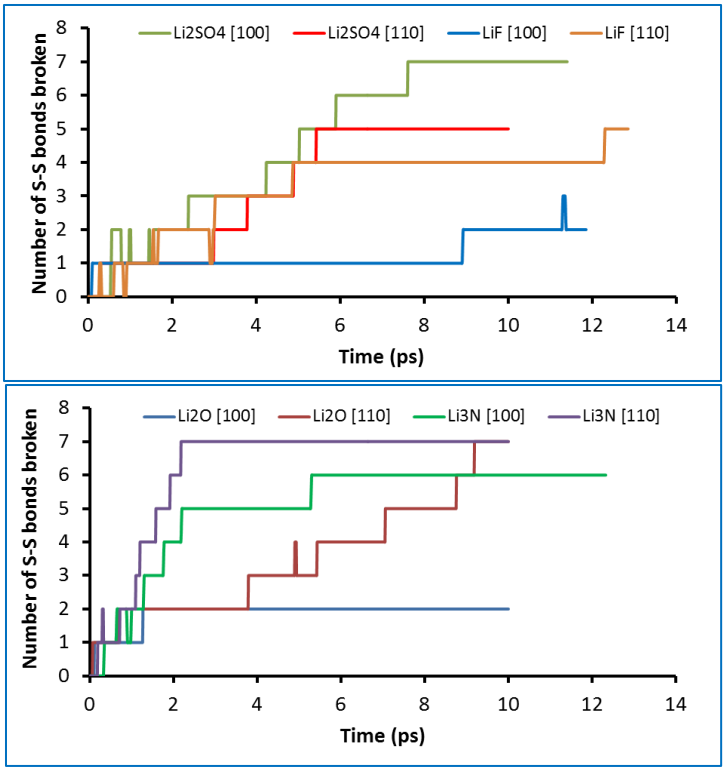

Figure 5.2: Number of S-S bonds broken as a function of time for thin films shown in **Table 5.1** and **Figure 5.1**. Top: for Li_2SO_4 and LiF surfaces. Bottom: For Li_2O and Li_3N surfaces.

5.4.2. THICK SEI LAYER OVER LI ANODE SURFACE

Using the least reactive facet found for the decomposition of the polysulfide in the thinner films discussed in the previous section, new models were built with thicker average thicknesses of 10 Å. Thus, the SEI layers tested were composed by Li_2O [100], LiF [100] and Li_2SO_4 [110], with the PS molecule initially located in the same position and distance from the SEI as in the thin film simulations. **Figure 5.3** depicts the number of S-S bonds broken as a function of time for the PS decomposing over Li_2O [100], LiF [100] and Li_2SO_4 [110] surfaces respectively. Based on this criterium, Li_2O [100] is the most stable surface, followed by Li_2SO_4 and LiF films that comparatively appear less

stable. Note that comparing the decomposition times in **Figures 5.2** and **5.3**, the thicker film does not offer a significantly better resistance to decomposition. Thus, **Figures 5.2** and **5.3** and **Table 5.1** indicate that the chemical nature of the film and its local structure play the major roles as protective layers.

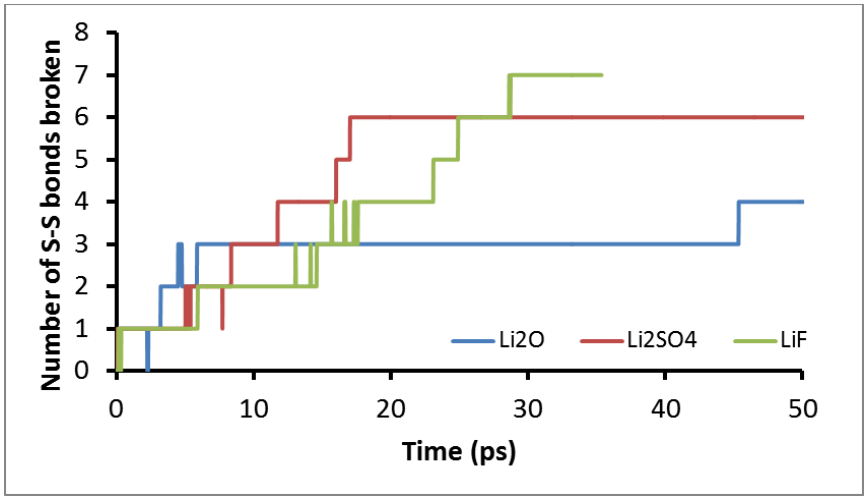

Figure 5.3: PS decomposition over 10-nm thick films of Li_2O [100], LiF [100] and Li_2SO_4 [110] covering the model anode surface as a function of time from the AIMD trajectories.

To understand how the PS decomposes on each surface, we have followed their decomposition mechanisms in three different SEI layer chemistries: Li_2O [100], LiF [100] and Li_2SO_4 [110]. Snapshots that follow the decompositions are depicted in **Figures 5.4**, **5.5**, and **5.6**. The first observation in all cases is that the PS decomposition is always very fast, and precedes those of the anion and the solvent. Here we use the nomenclature PSX to designate the fragments of Li_2S_8 decomposition where X is the number of S atoms in the remaining fragment. For a Li_2O [100] layer (**Figure 5.4**), the PS breaks sequentially. Initially, the first S-S bond breaks forming PS5 and PS3

fragments (anions or radical anions) normally paired with Li ions. At 0.96 ps both PSX fragments are recombined apparently forming a PS8, but in a few picoseconds, the end S atom from PS5 transfers to PS3 forming two PS4 anions. Each of these PS4 fragments later break (~7ps), forming two PS3 and two PS1 anions or radical anions paired with Li ions. Between 7 ps and 50 ps, the system stabilizes, there is no further decomposition of the PS fragments during this period. **Figure 5.4** also shows a certain degree of surface distortion, driven by migration of Li ions that pair the PSX anions. Note that at the end, most of the S anions are already near the surface and nucleation of Li_2S is expected to follow.

Figures 5.5 and **5.6** show the decomposition mechanisms detected for LiF and Li_2SO_4 respectively. In all cases, rapid PS decomposition is observed, with the participation of Li ions from the surface. In comparison with Li_2O (**Figure 5.4**) the surface distortions on LiF and Li_2SO_4 appear larger with surface Li ions migrating towards the electrolyte to combine with PSX fragments. Although the PS decomposition mechanisms shown in each SEI film are different, there are some common points. In the three studied cases, the first formed PS fragments are PS5 and PS3 anions (or radical anions), usually paired with two Li ions, i.e., they are mostly neutral species in solution. However, in the cases when recombination of S-S bonds was observed, there is a deficit or excess of charge in one of the PS fragments. As can be observed in **Figures 5.4** to **5.6**, the surface is able to hook the PS5 fragment (anion or radical anion) formed by the first S-S bond breaking from the PS8 molecule, where the final S in the chain becomes bonded to Li atoms of the surface. Interestingly, the presence of the PS5 species close to

the surface is in agreement with a recent AIMD and XPS study.[209] The largest surface distortion is found on the Li_2SO_4 surface, (**Figure 5.6**) where the separation of SO_3 groups is clearly observed. The Bader electronic charges are shown in **Figures 5.4**, **5.5**, and **5.6** illustrate that the electron transfer from the surfaces is similar independently of the type of SEI film.

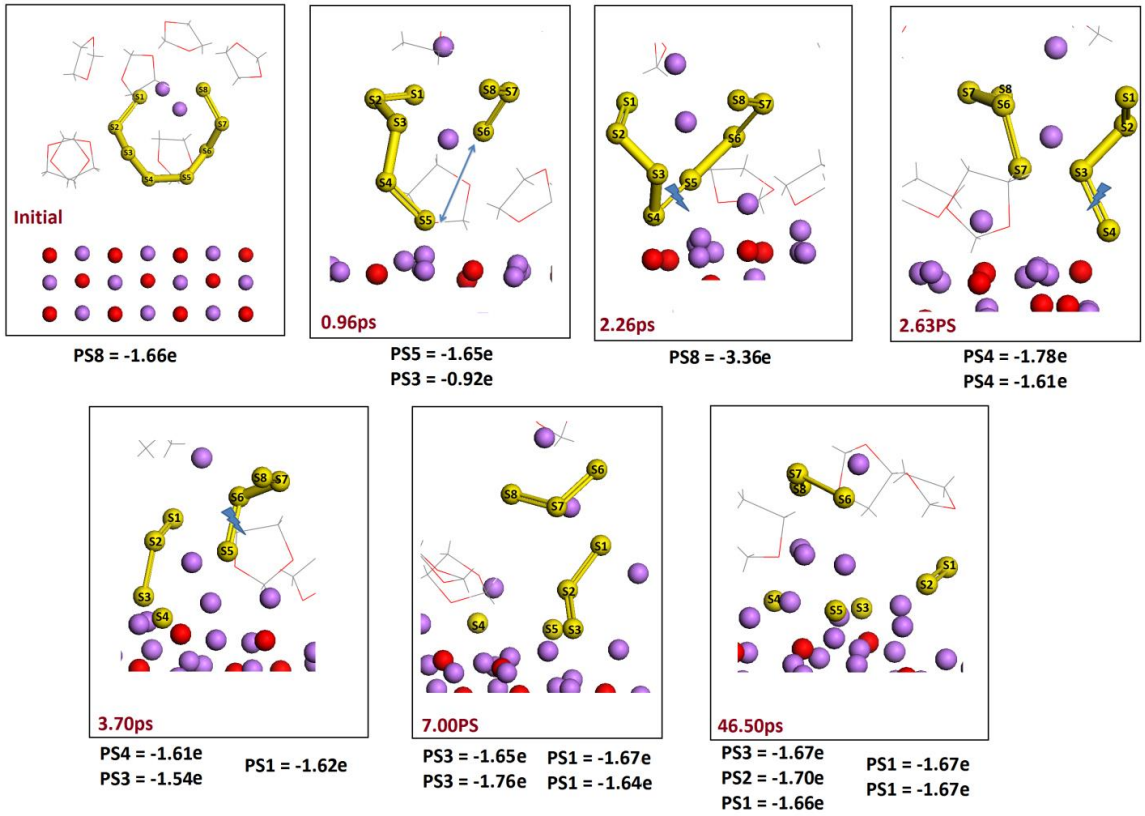

Figure 5.4: Partial sequence of PS decomposition obtained from AIMD for DOL/LiTFSI/PS mixture over a model lithium anode covered by a ~10 nm thick Li_2O [100]. One PS molecule is initially placed close to the surface. There are no changes between 7 ps and 46.5 ps. Bader charges regarding different PS anion fragments are shown at the bottom of each figure. Color code: S:yellow; C: grey; O: red; H: white; Li: purple.

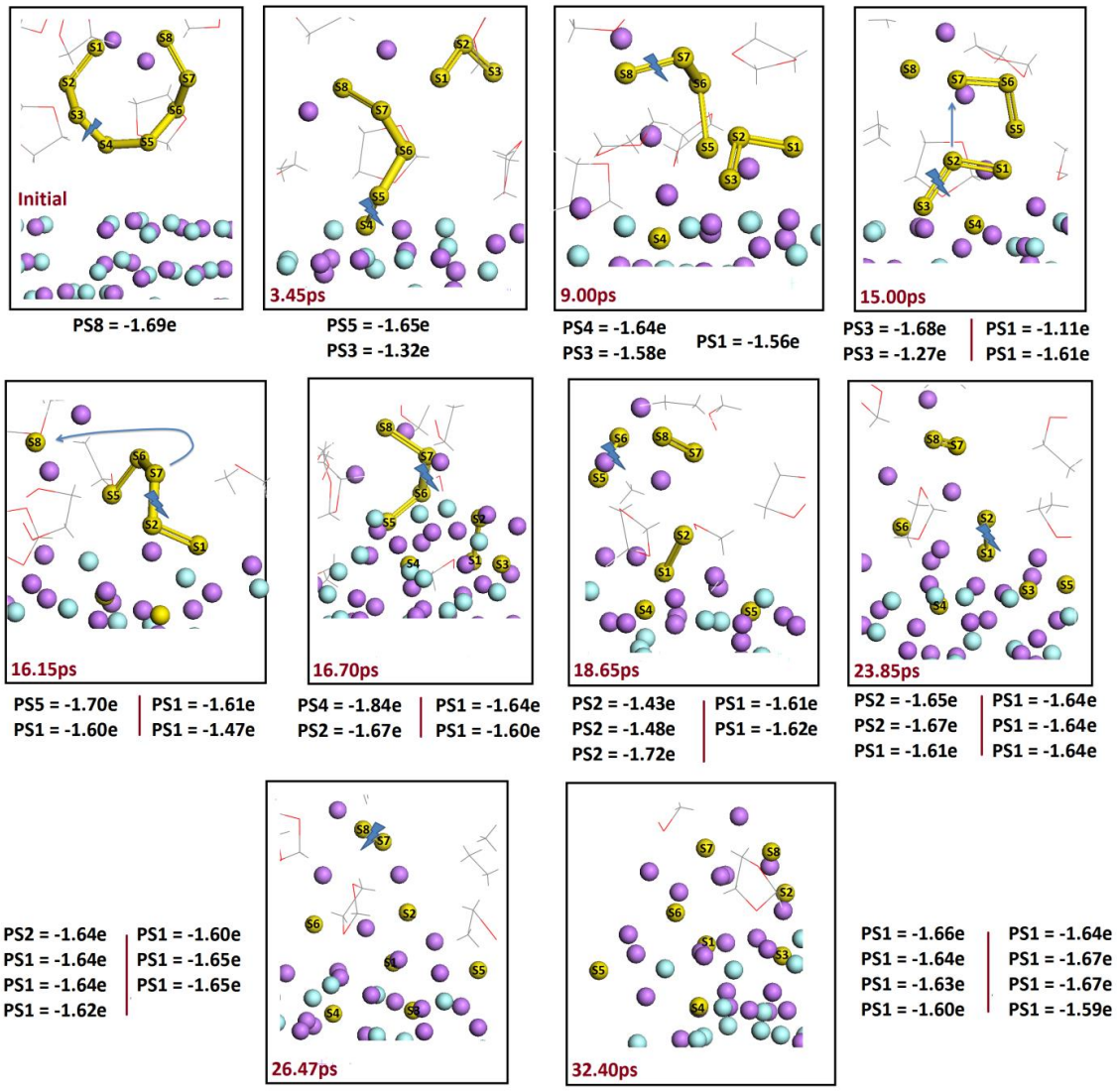

Figure 5.5: Sequence of PS decomposition obtained from AIMD for DOL/LiTFSI/PS mixture over lithium anode covered by LiF [100]. PS is initially placed close to the surface. After 26.47 ps the last S-S bond breaks. Bader charges regarding different PS anion fragments are shown at the bottom of each figure. Color code: S:yellow; C: grey; O: red; H: white; Li: purple.

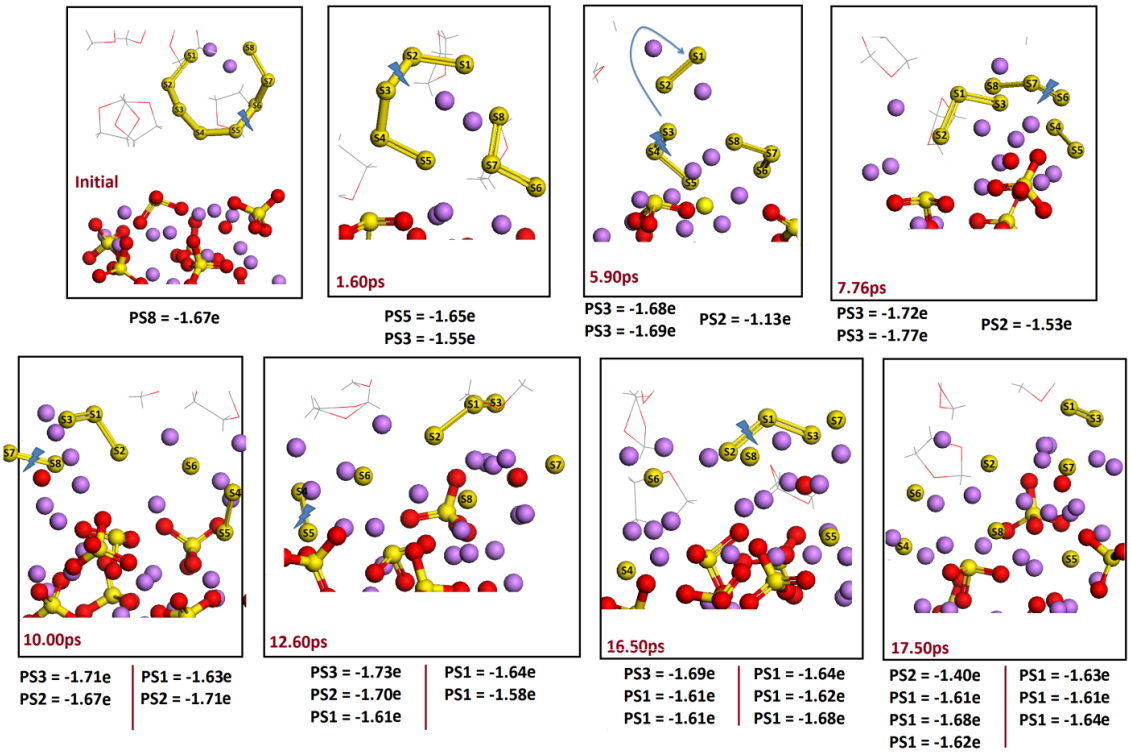

Figure 5.6: Partial sequence of PS decomposition obtained from AIMD for DOL/LiTFSI/PS mixture over lithium anode covered by Li_2SO_4 [110]. PS is initially placed close to the surface. At 16.50ps the last observed S-S bond breaks take place. Bader charges regarding different PS anion fragments are shown at the bottom of each figure. Color code: S:Yellow; C: grey; O: red; H: white; Li: purple.

Comparing the time for breaking of the first two S-S bonds it is found that it takes almost the same time for Li_2SO_4 and LiF, while at the same time there are already four bonds broken for Li_2O (**Figure 5.3**). This could be associated with an initial higher concentration of Li over the surface in the case of Li_2O, due to the structure of the cleavage plane. However, in contrast to the behavior on Li_2SO_4 and LiF surfaces, larger fragments of PS stabilize in Li_2O surfaces for much longer times (~45 ps). Thus, it is suggested that the concentration of Li on the facets plays a role in the first steps of the decomposition, decomposing faster at higher concentration of lithium on the surface,

whereas at longer times, the reactivity is governed by the electronic properties of the SEI film. The assumption that the concentration of Li on the facet initially affects the reactivity of PS is consistent with the observation of different facet reactivity detected in the analysis using thin layers (**Table 5.2**).

The difference in the PS decomposition over the SEI layer should also be associated with the electronic properties of the SEI layer such as their ability to transfer charge to the PS and the diffusion of Li and S through the SEI layer since the structure of the material affects the diffusion of the elements present. Thus, the initially calculated total charge of the S atoms belonging to the PS decays differently over time (**Figure 5.7**). It is found that even though (as discussed above) the Li_2O surface initially induces a faster initial reactivity, the PS fragments are much more stable at longer times on this surface than in the other two surfaces. Comparing the three surfaces, the LiF surface is the first that decomposes the molecule completely, followed by Li_2SO_4, and last Li_2O. Note that total PS decomposition is not necessarily bad for protection; it all depends on the quality of the film formed by Li_2S and LiF in this case. This topic is worthy of further investigation.

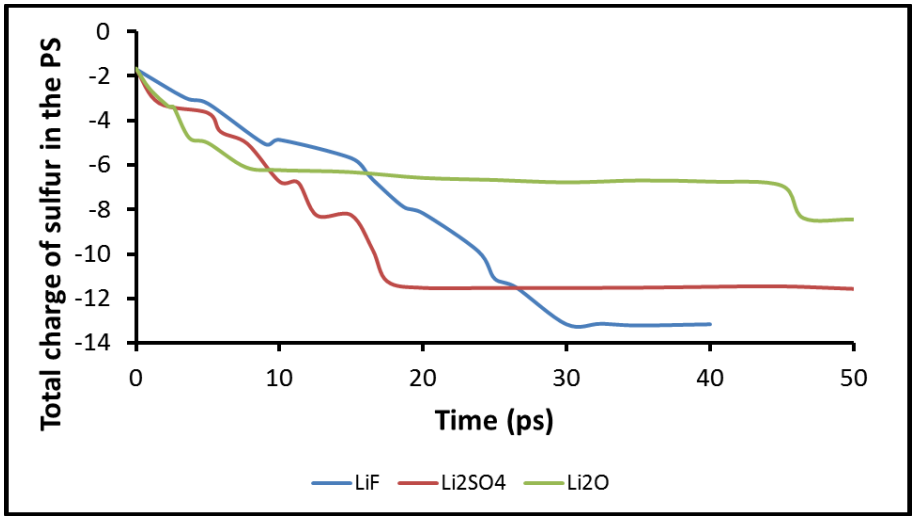

Figure 5.7: Charge evolution of the PS molecule located over a SEI film of ~ 10 Å thickness.

In absence of an electric field, as the PS molecule becomes instantaneously reduced by the surface, the negatively charged PS fragments produced during the decomposition diffuse in the direction of the anode surface while Li ions of the surface move in the direction of the electrolyte (**Figures 5.4** to **5.6**). As in the models, the Li-anode and SEI are periodic in the x and y directions, the penetration of S atoms through the SEI was tracked by changes in the z direction (perpendicular to the anode surface) over time. In **Figure 5.8**, the interface between the SEI film on the anode surface and the electrolyte is set to z =0, and the changes are tracked as the S atoms move through the SEI film in the direction of the anode. Initially, the average of S positions rapidly moves down in the direction the anode surface, and then it oscillates keeping an average position during some time before moving again in the anode direction. This observation can be explained by a S atom or small PS fragment being trapped inside the SEI and then moving down. In Li_2O there is a fast motion of the S or PSX fragments, followed by

formation of stable components that become trapped inside the SEI film. In Li_2SO_4, a fast initial diffusion takes place reaching the z=0 line, which corresponds to the anode surface, thus the S fragments spread over the anode surface. In LiF, the average position of S fragments temporary stabilizes inside the SEI and then spreads over the anode surface. This suggests a very different behavior of the three films: in Li_2O the S atoms may enrich the Li_2O film before migrating towards the anode surface, whereas in Li_2SO_4 and LiF the final deposition of Li_2S will take place right at the anode surface.

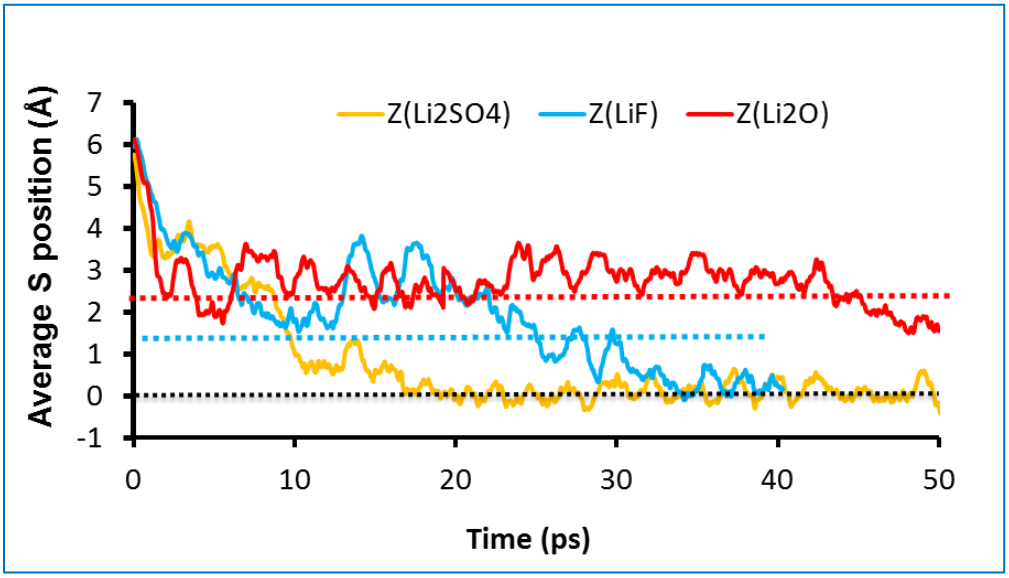

Figure 5.8: Time evolution of the average position of S atoms from the PS decomposition, traveling in the z direction through various SEI materials of ~6 Å thickness. The zero is at the interface between the SEI model and the anode surface.

We have examined the time evolution of the anode and SEI atoms. The sum of all lithium atoms charge in the slab and the SEI over time are displayed in **Figure A.3**. In the three cases (Li_2O, LiF, Li_2SO_4) the charge of Li in the SEI layer is not constant and it oscillates with time. However, the variation of the total charge per Li atom in the

SEI is much smaller than those in the anode (**Figure A.4**). However, the total charge of Li in both parts of the system (anode and SEI) mutually affect each other. When the anode supplies electrons to decompose the electrolyte, an instantaneous modification on the charge of Li in the SEI takes place (**Figure A.3**).

5.4.3. DENSITY OF STATES OF THE SEI FILMS

To understand how the charge is transferred from the metal anode through the SEI layer decomposing the PS species, the density of states (DOS) of each SEI layer (as described in the computational methods section) were calculated using the HSE06 functional as implemented in VASP. The DOS were calculated for the initial frame and also for the last frame of each SEI simulated, as illustrated in Figure III.9 for Li_2O. The DOS graphs for the other two films are shown in **Figures A.5** and **A.6**. The results indicate that there are intermediate states between the valence and conduction band, supporting the hypothesis that the SEI with the thickness used in the simulations have an electronically conductive behavior.

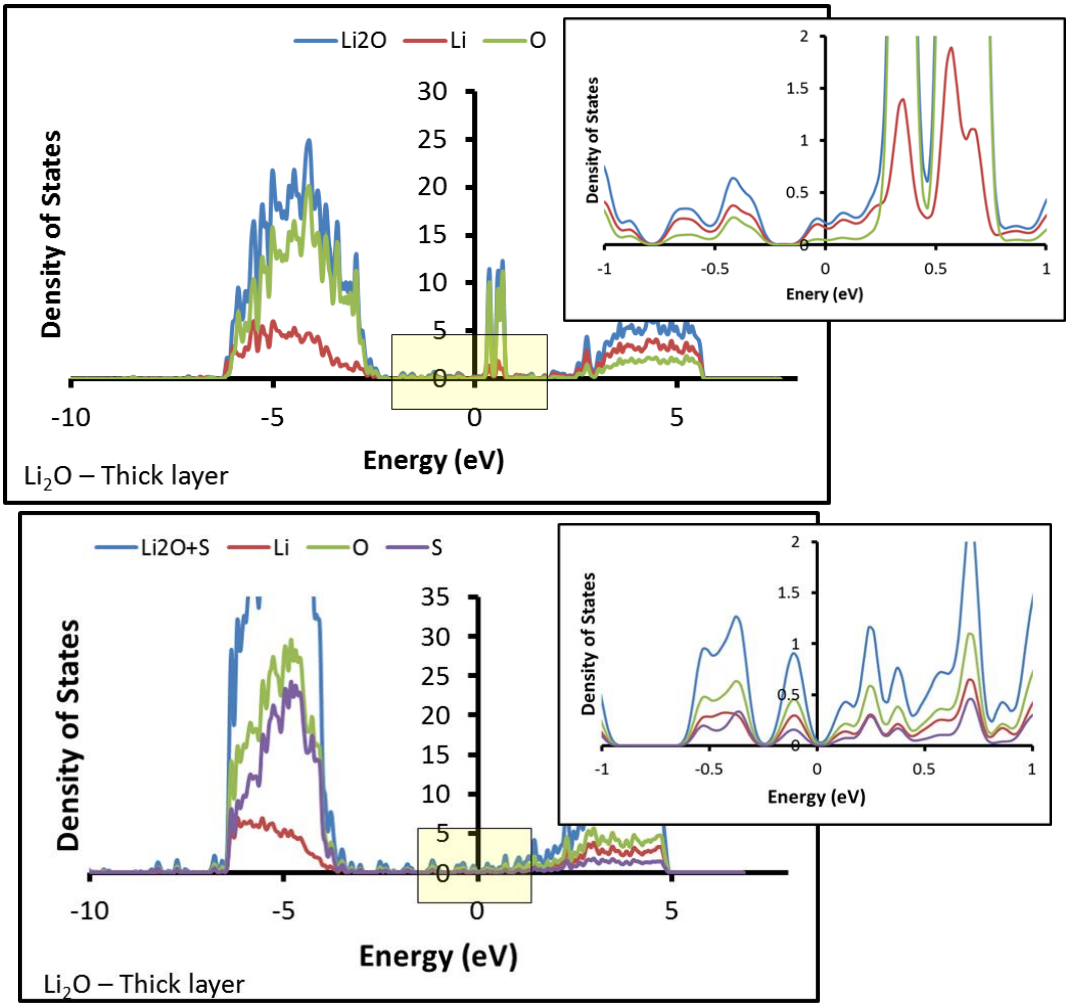

Figure 5.9: DOS of the SEI composed by Li_2O using the HSE06 hybrid functional. The graphs show the presence of intermediate states between the main valence and conduction bands. Fermi level energy is set at 0 eV. The DOS correspond to the 10 Å SEI layer at the beginning and at the last calculated frame in each simulation.

5.5. CONCLUSION

AIMD simulations show that the presence of a thin (1 nm) SEI layer covering the Li metal anode slows down but does not shut down the PS decomposition. Li_2O, Li_2SO_4, Li_3N, and LiF were tested as possible SEI constituents formed during the decomposition of common electrolytes used for Lithium-Sulfur batteries. The results indicate that not

only the chemical nature but also the structure of the exposed facet and the thickness of the film may affect reactivity. A very fast PS decomposition was observed in all cases, always preceding the decomposition of the other components (salt anion and solvent). The individual mechanisms were followed based on the AIMD trajectories. Common patterns were found in all cases such as the initial decomposition into PS5 and PS3 polysulfide fragments that could be anions or radical anions usually paired with Li ions. Li atoms from the surface participate in the reactions, and the surfaces suffer severe reorganizations. The comparison between the performance of 10 Å films of Li_2O, LiF, and Li_2SO_4 model layers suggest that Li_2O is the most effective to slow down total decomposition; however it is noted that once the PS is decomposed to the final Li_2S products the new SEI layer may have better protective effects than the initial one. Future work will focus on further elucidation of the electronic properties of the SEI films and their dependence on the structural characteristics. Moreover, it would be interesting to determine what would be the SEI thickness for typical SEI components that would stop electrolyte decomposition.

6. BUILDUP OF THE SOLID ELECTROLYTE INTERPHASE ON LITHIUM-METAL ANODES: REACTIVE MOLECULAR DYNAMICS STUDY[3]

6.1. SYNOPSIS

Using reactive molecular dynamics simulations we evaluate atomistic-level interactions leading to the formation of surface films on a Li metal (100) surface in contact with an electrolyte solution. We observe the evolution of the interfacial region and the formation of well-defined regions with varying density and oxidation state of Li; the penetration of electrolyte molecules and in some cases their electron transfer-driven decomposition leading to the initial formation of solid electrolyte interphase products. The simulations are done in the absence of a bias potential, and using various electrolyte compositions including highly reactive solvents such as ethylene carbonate and less reactive solvents such as 1,3 dioxolane mixed with a 1M concentration of a lithium salt. The structure and oxidation state of Li and some of the fragments are followed through the metal dissolution process. The results are important to understand the nature of the Li metal anode/electrolyte interface at open-circuit potential.

6.2. INTRODUCTION

The global energy demand has increased steadily in recent decades[229,230]. Mohr et al.[231] forecasted that the fossil fuel consumption will peak in 2025 and it would stagnate for the next 50 years and then strongly decline. This is because the reservoir may

[3] Reprinted with permission from Samuel Bertolini and Perla B. Balbuena. " Buildup of the Solid Electrolyte Interphase on Lithium-Metal Anodes: Reactive Molecular Dynamics Study." The Journal of Physical Chemistry C 2018. Copyright 2018, American Chemical Society.

become technically, energetically, and economically unfavorable for extracting fossil fuels. To replace fossil energy sources, green energy production through wind, solar power, or other sources are being used, although this production has an intermittent nature requiring energy storage[232-234]. Lithium batteries (LiBs) are important component energy storage devices with numerous applications[235]. However, several of these applications need an increase in the specific capacity of the batteries. Current batteries have specific capacities of 3860, 4000, 990, and 370 mAh/g for Li-metal, Li-Si, Li-Sn, and Li-graphite respectively [11,12]. While Li-Si and Li-metal anodes have the problem of dendrite growth during charge, Li-Si also has a problem of high volume expansion of 300% [236], leading to a fast degradation of the anode. The dendrite formation generates short life cycles and safety hazard, because of the contact between the dendrite and the cathode, producing a short circuit, which with flammable solvents, generates exothermic and runaway reactions [14].

In LiBs, electron transfer from the anode surface induces electrolyte decomposition and formation of inorganic and organic components at the interface between the anode and the electrolyte. These electrolyte decomposition products nucleate and grow new phases defining a solid electrolyte interphase (SEI) layer.[237] The products found in the SEI depend mainly on the electrolyte composition. Typical SEI components in Li-metal anodes are Li_2O, Li_2CO_3, and LiF. Alternatively, an artificial SEI layer can be built by pre-treating the anode before the LiBs is assembled and cycled [238,239]. The SEI layer ideally prevents a continuous degradation of the anode and electrolyte, passivating the surface, but also it may affect the behavior of the LiBs by

increasing cycle life and affecting ionic diffusion of Li. Wang et al. [240] observed that using an electrolyte composition of 1,4-dioxane (DX), 1,2-dimethoxyethane (DME), and lithium bis(fluorosulfonyl)imide as salt, dendrite formation is suppressed. Qian et al. [241] also observed the prevention of dendrite formation at high salt concentrations, using 4M LiFSI, or using $LiNO_3$ that induces the formation of a protective SEI layer [109,201,202,242].

Two mechanisms are commonly used to describe the buildup of the SEI layer and the dendrite growth: the conventional model described by Aurbach et al.[43,44,243-245], and the porous model proposed by various authors[45,46]. In the conventional model, the SEI layer is initially formed by the inorganic layer, composed by pristine components such as Li_2O, LiF and Li_2CO_3. Because of a continuous reduction of the species, the inner layers may be in lower oxidation states than in the outer layers of the SEI, where the continuous precipitation and dissolution of lithium forms a porous structure. This is followed by the dissolution of lithium (oxidation) in the electrolyte. Finally, when an electric field is applied, the reduction of lithium ions and deposition of metallic lithium takes place, but the inorganic phases present in the SEI cannot accommodate morphological changes of the lithium deposited or dissolved. These morphological changes make the SEI to break, exposing the lithium bare phase and creating a preferential path for lithium deposition. Therefore, this preferential path will create the sites for dendrite growth [43].

On the other hand, the porous model[45,46] states that a morphological change from a dense to a porous phase takes place. Because of the existence of a porous phase, the

electric field is unevenly distributed and the dendrite will grow from the sites where the electric field concentrates. Not only decomposed electrolyte species stay in the porous phase, but also intact molecules of the electrolyte co-exist. The concentration of lithium is also not homogeneous, and increases in the regions closer to the dense phase. The dense phase is consumed by the electrolyte to form the porous phase, which expands in direction of the electrolyte. It is assumed that the porous phase will grow and reduced Li eventually will form clusters that will stay as dead lithium, while the thickness of the porous phase would keep increasing because of further electrolyte reduction.

The main difference between the porous and the conventional model is the way each model discusses the dendrite growth. Here we focus on the initial stage of formation of surface films, and do not reach to the stage of dendrite nucleation and growth. However, hopefully, understanding the initial state of the surface films provides new insights to elucidate dendrite formation. We simulate the buildup of the SEI layer using classical molecular dynamics calculations. Although ab initio molecular dynamics simulations can predict the chemistry with a higher level of accuracy, they are nowadays restricted to small systems (less than 1000 atoms). However, bigger systems and bond breaking/bond forming events can be calculated by classical molecular dynamics simulations with a reactive force field (ReaxFF).[246] ReaxFF is able to predict the bond order, by calculating the partial energy due to bond kind, over and under coordination, including penalty, lone pair, valence, and torsion energy contributions. ReaxFF also includes contributions from nonbonded energy, such as van der Waals and Coulombic interactions [128]. The interatomic distances are used to calculate the bond order and they

are updated in every simulation step. The Morse potential is used to calculate van der Waals energy, while Coulomb energy uses the charge cquilibration method [247-250] to estimate and update charges during the simulations. Recently, new improvements to the method, named eReaxFF, have been introduced by Islam, van Duin, et al. [251,252] where explicit electrons are simulated within the framework of the ReaxFF methods. We note that such force field should be a more accurate description of the electron transfer reactions than ReaxFF. However, eReaxFF is not yet parametrized for all the atomic interactions analyzed in these simulations. For this reason, we used ReaxFF[128] that has proved to be successful in predicting SEI formation in silicon anodes.[253] To have at least a partial validation of our findings, we compare them with results from our own quantum chemical calculations and ab initio molecular dynamics simulations of smaller systems.

The simulations are done in the absence of a bias potential, and using various electrolyte compositions including highly reactive solvents such as ethylene carbonate (EC) and less reactive solvents such as 1,3 dioxolane (DOL) mixed with a 1M concentration of a lithium salt. The structure and oxidation state of Li and some of the fragments are followed through the metal dissolution process. The results are important to understand the nature of the Li-metal anode/electrolyte interface at open circuit potential.

6.3. COMPUTATION MODEL

The ReaxFF was developed for the atoms C/H/O/S/Li/F/N relations and, the interactions were trained for LiB materials [254,255]. Each cell was built in three different

regions, which represent the solid lithium metal anode, the electrolyte and a bilayer of graphite, see **Figure B.1**. The thin graphite bilayer allows isolating the bottom surface of the lithium anode from the electrolyte phase, which occurs due to the periodic boundary conditions. The anode was obtained from the Li body-centered cubic (bcc) structure with lattice parameter 3.442 Å, then the cell was cleaved along the (100) to build a slab with cell parameters of 55.2 Å x 27.4 Å x 67.2 Å. Different solvents/additives such as DOL, dimethyltrifluoroacetamide (DMTFA), EC, fluoroethylene carbonate (FEC), DME and 1,4 dioxolane DX as solvent, and 1M of Trifluoromethanesulfonate (triflate) as the salt, were used in some of the electrolytes. Electrolytes tested include pure DOL, DOL + 1M Li-triflate, DOL:DMTFA (1:1, molar rate), DOL:EC (1:1), DOL:FEC(1:1), and pure DX, DX + 1M Li-triflate. After assembling the Li metal slab, the electrolyte and the graphite layers (**Figure B.1**), the simulation cell parameters changed to 55.2 Å x 27.4 Å x 164.8 Å .The simulations were carried out in the canonical ensemble at constant number of particles N, volume V, and temperature T. The temperature was kept constant using the Nosé Hoover thermostat[256] with a time step of 0.1 fs and a temperature of 300 K. The simulations were carried out using LAMMPS.[257]

When explicitly mentioned, the charge was studied by density functional theory (DFT) [210,211] calculations within the plane-wave basis set approach [212,213] using the Vienna Ab-initio Simulation Package (VASP) [214,215]. A 2×2×1 Monkhorst-Pack k-point mesh [172] was employed to generate k-point grids for the Brillouin zone sampling. A 400 eV cutoff energy for the plane-wave basis set is used to achieve both computational accuracy and efficiency. Electron-core interactions were described by the projector

augmented wave pseudopotentials [169,170] as provided in the VASP database. The charge analysis from the VASP structures was carried out using Bader calculations [27].

6.4. RESULTS AND DISCUSSION

The simulations reveal that the anode surface starts to be consumed as soon as the Li-metal surface gets in contact with the electrolyte. The Li atoms consumed by the electrolyte produce a new phase, here called porous phase; while the non-consumed part of the anode is called the dense phase. The porous phase is formed by two different regions, the nest and the disperse phase. As shown in **Figure 6.1**, in the nest phase, the Li atoms, although forming an amorphous structure, are connected between themselves and also connected to the dense phase of the anode. Moreover, in the nest phase, Li atoms arrange forming channels filled by the unreacted electrolyte, which can also have intact molecules from the electrolyte. On the other hand, in the disperse phase, Li atoms do not show any connectivity among themselves, instead they are combined with fragments produced by decomposition of the electrolyte as well as with non-reacted species. That is, the disperse phase is where the SEI nucleates. Dissolving Li atoms that migrate toward the electrolyte are oxidized: a positive charge develops on them and increases as they get farther from the dense phase. In the nest phase, the calculated charges vary from +0.15|e| to +0.40|e|, and in the disperse phase, they range from +0.40|e| to +0.65|e|. The charge of Li atoms in the dense phase can be considered as neutral as discussed in a later section.

Although both the conventional and the porous SEI buildup models share several similarities especially in the surface film formation stage, the presence of non-decomposed species of the electrolyte, in the nest phase and in the disperse phase, indicates that the porous model [45] could be more appropriate for describing the buildup of the SEI interphase than the conventional model [43,44,243-245]. In these simulations, the uneven distribution of Li through the so called porous phase and the presence of intact species of electrolyte, corroborate the observations detected by Lu et al. [45]. As proposed in the porous model, our simulations identify not only a porous SEI but also a change in the lithium concentration and oxidation state throughout this phase. The simulations suggest that there is an increase of Li concentration closer to the dense phase (**Figure 6.1**). Also, Li ions and reacted species coexist with intact electrolyte molecules throughout the whole porous phase. Li distribution is more uneven in the nest phase than in the disperse phase. In the nest phase Li atoms organize as nano channels and nano voids. As can be observed in **Figure B.2**, the densities of atoms in the nest phase and in the disperse phase reduce away from the dense phase, with the density of the nest phase being larger than that in the disperse phase. A linear interpolation of the density of atoms through the X direction gives a value of R-square smaller for the nest phase than for the disperse phase, suggesting that the disperse phase is more homogenously distributed than the nest phase. **Figure B.2** also shows that the composition of the electrolyte affects the Li atomic density profile of the cell. The presence of Li- triflate causes volume expansion and also changes the porous phase density. When the electrolyte contains Li-triflate, Li starts to concentrate preferentially in some regions of the disperse phase. With

time, it forms clusters in that region (**Figure 6.1**), and their size grows over time. The clusters formed on the disperse phase have a high concentration of Li atoms interconnected between them, but also have a high concentration of other species, such as O and F based compounds with Li ions, and poly(carbon monosulfide). In the electrolytes containing Li-triflate, the clusters start to form after 1.2ns of simulation. In all the tested cells that contain only the solvent without salt, the formation of a cluster in the disperse phase was not observed in the 500ps of simulation. Therefore, the simulations suggest that the presence of the salt is important to nucleate or accelerate nucleation kinetics of the SEI. As previously mentioned, an uneven distribution of lithium atoms may lead to dendrite growth. **Figure B.3** illustrates the formation of the porous phase, showing the structural changes of the porous phase. Initially, the electrolyte consumes the dense phase of the anode to form the nest phase. The nest phase stabilizes its thickness, while the porous phase keeps growing in the direction of the electrolyte, consuming the dense phase, evolving toward the disperse phase. Around 1 ns, the nucleation of the clusters starts and grows with time. At 2 ns of simulation, only one of the nuclei grows, forming a bigger cluster, around 15Å diameter. The simulations suggest that if the surface has imperfections such as a tip of nanodimensions, see **Figure B.4**, the tip dissolves in the electrolyte to form the nest and disperse phase, and the porous phase grows with a homogeneous thickness over the dense phase. The dissolution of the tip is almost complete at 8 ps of simulation as shown in **Figure B.4**, and is very fast; at 12ps the tip is completely dissolved.

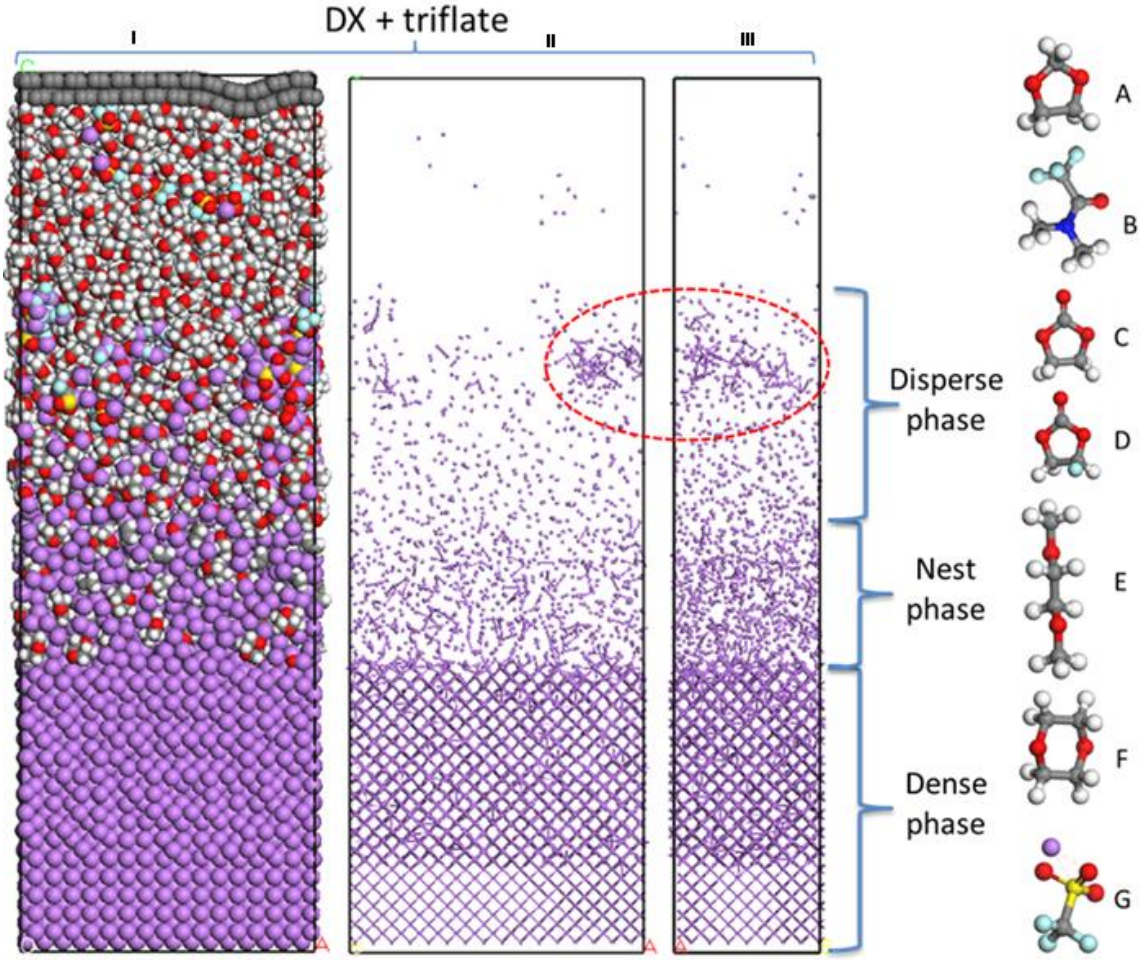

Figure 6.1: Configuration of the cell at 2 ns of simulation, using DX as electrolyte with 1M triflate concentration. Color code: Li: purple, O: red, C: gray, H: white, F: cyan and S: yellow. I) Front side view of the cell showing all the atoms. II) Front side view of the cell showing only lithium atoms, while the other atoms are hidden. III) Side view of the cell showing only lithium atoms. The molecules tested (shown in the structures) were (A) DOL, (B) DMTFA, (C) EC, (D) FEC, (E) DME, (F) DX, (G) Li-triflate

Figure 6.2 depicts the charge distribution of the Li atoms in the simulation cell. As shown in the color spectrum shown in the figure, the charges range from zero to +0.65 e. These charges were calculated using the charge equilibration method as implemented in LAMMPS. As it is well-known, the electronic charges on the atoms or atomic sites are not direct observables, and the fractional numbers are just artifact of the

computational method that assigns a number based on the distribution of electronic density. Thus, the fractional charge does not correspond to a physical quantity, and it only provides an estimate of the oxidation state of the particular atom or atomic site.

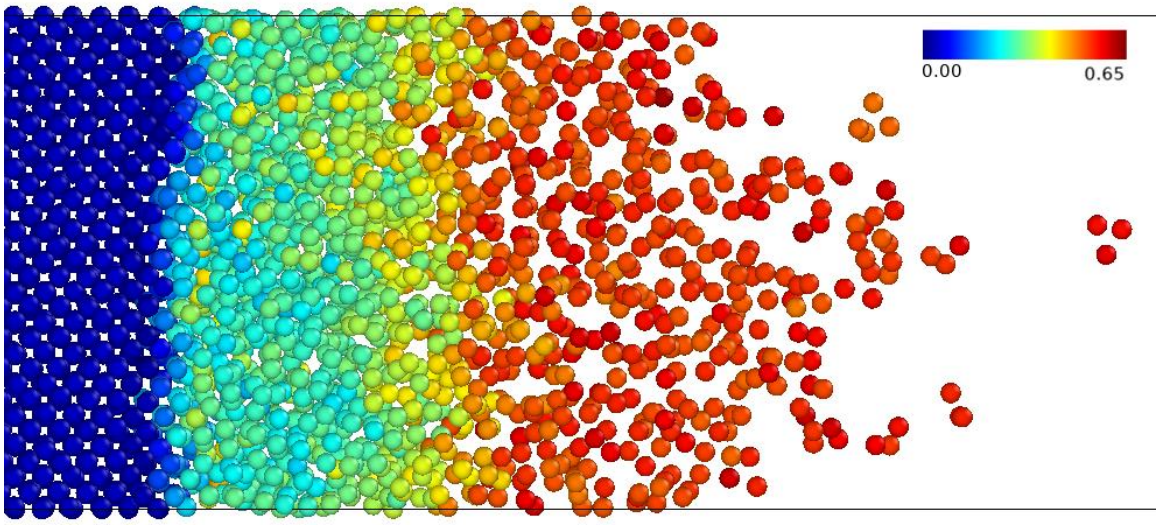

Figure 6.2: Charge spectrum of Li atoms in the dense, nest and disperse phase (see Figure 1 for identification of the phases).

Both in the nest and disperse phases, Li has a very different structure than in the bulk bcc phase. As can be observed in the Li-Li radial pair distribution function (RPDF) (**Figure 6.3**), the nest and disperse phases present a first peak around 3.2 and 3.5Å respectively, for each electrolyte simulated. In the disperse phase, Li may organize mainly in pairs (that form and dissolve over time), with a liquid-like structure, while in the nest phase Li has an amorphous structure, organizing more as a solid. As shown by the RPDF, it is possible to observe a lower density of dissolved Li atoms in pure DME compared with other electrolytes, for both nest (**Figure 6.3a**) and disperse (**Figure 6.3b**) phases. Except for DME, all the electrolytes tested without triflate only slightly affect

the configuration of the nest phase, while DME reduces Li dissolution. The disperse phase, which contains the SEI products, is strongly affected by the nature of the electrolyte (**Figure 6.3b**). The lithium atoms get more sparse in DOL, DME and DOL:DMTFA, while they are more concentrated in electrolytes with DOL:EC, DOL:FEC and DX. This result suggests different reactivities of the two groups of electrolytes, and therefore different SEI products nucleating in such phase. When Li-triflate is added to the electrolyte, a different structure is observed in the nest and disperse phases depending on the solvent species, as shown in **Figure B.5**. With DOL as the solvent, Li-triflate affects the nest phase only at the beginning of the simulation (500ps), and with time it evolves to the same configuration in the case of pure DOL. However, Li-triflate has a strong influence on the disperse SEI nucleating phase. Although in the disperse phase Li, gets sparser with time, the presence of Li-triflate tends to increase the concentration of lithium when compared with pure DOL (see **Figure B.5**). In DX, the effect of Li-triflate is slightly dissimilar, because in the nest phase, it stabilizes a higher concentrated phase in Li; which without the presence of Li-triflate gets more spread out with time. For an electrolyte formed by solvent+ Li-triflate an opposite effect to that in DOL is observed when the solvent is DX; inducing the disperse phase to get sparser.

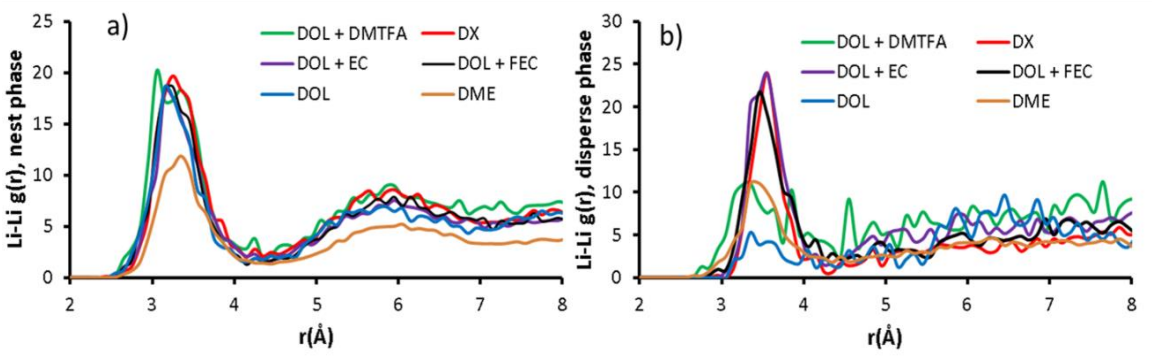

Figure 6.3: Li-Li RPDF (a) in the nest phase and (b) in the disperse phase tested in different electrolytes after 500ps of simulation.

The RPDF and the integral of RPDF of the dense, nest, and disperse phases were done at different times of simulation, where the electrolyte is DX and 1M Li-triflate (**Figure 6.4**). The change in RPDF of the dense phase can be considered negligible over time, keeping the same solid structure, and changing only its thickness that after the initial Li dissolution becomes constant over time. The structure of the nest phase changes at the beginning of the simulation, becoming less dense between 10 and 100ps, and then remaining approximately constant. The change in thickness of the nest phase occurs before 1500ps and then becomes constant over time. This suggests that while the nest phase expands after 100ps, it remains with the same structure most of the time. The SEI-nucleating disperse phase is the one that suffers a large change at the beginning of the simulation, before 100ps. However, it keeps changing slowly after 100ps. Thus, the structure of the disperse phase changes while it expands. The thickness of the porous phase (nest and disperse phase) is further discussed later, via a charge analysis. Both nest and disperse phases, during the regime where their structure is changing, become sparser.

During the decomposition of the electrolytes containing DOL and DX, the most common products observed during 2 ns of simulation are Li_2O, LiF and ethylene. The simulations indicate, as observed in **Figure 6.5**, that the disperse phase will host the inorganic SEI layer, composed mainly of Li_2O and LiF, produced due to the decomposition of the salt (but also solvent) over the anode, and the presence of non-decomposed molecules. Ethylene molecules, produced by solvent decomposition, concentrate mainly at the interface between the nest phase and the disperse phase. Species generated because of partial decomposition of the electrolyte, such as OCH_2CH_2, OCH_2CH_2O and OCH_3, exist in the porous phase in low concentrations during the entire simulation, and they appear during some period of time and fast decompose/recombine forming other molecules or fragments. The polymerization of electrolyte species was not observed in the short 2 ns simulation time. However the polymerization of species is expected, mainly due to the reactions between the electrolyte and species such as ethylene, OCH_2CH_2, OCH_2CH_2O, and OCH_3 that may form the polyolefin species usually found in the SEI.[258-261]

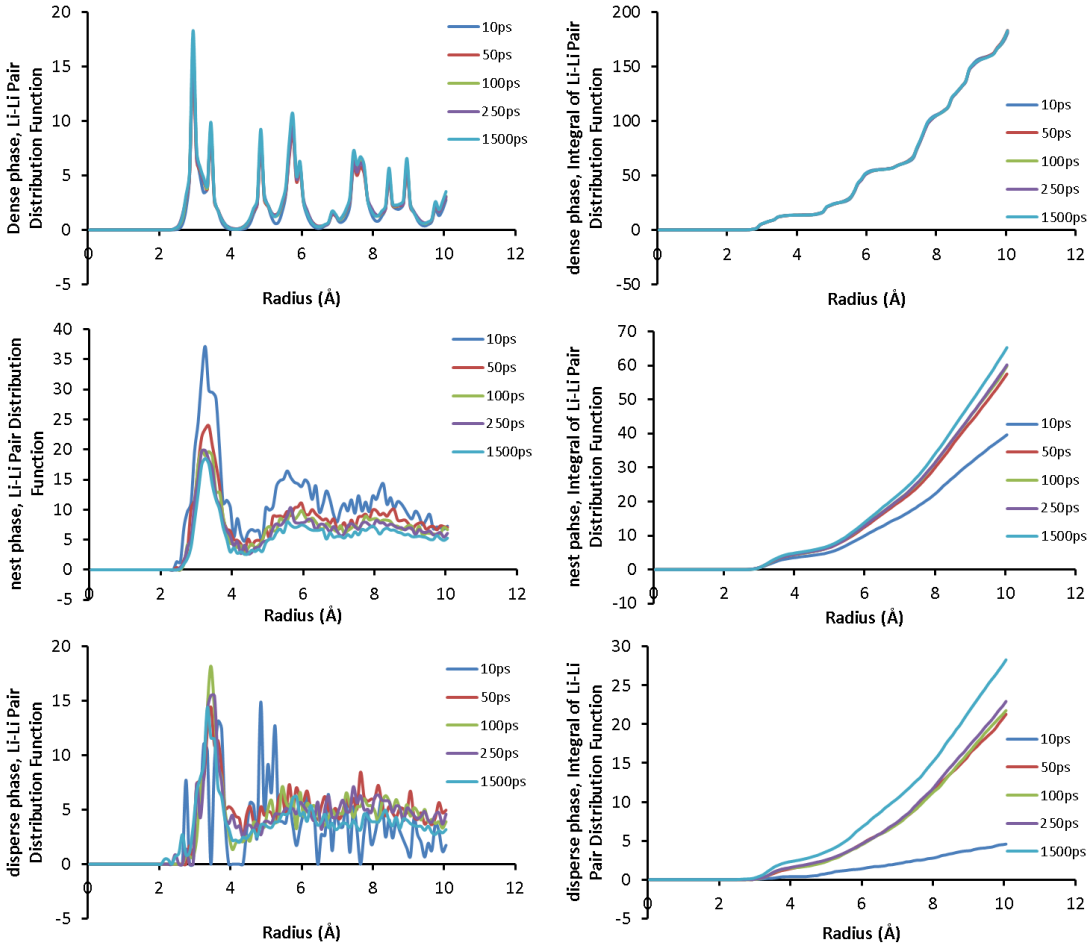

Figure 6.4: Time evolution of the Li structure in the various phases. Li-Li RPDF (left) and integral of RPDF (right) for: dense, nest, and disperse phases, at several simulation times.

Analysis of the charge distribution of ethylene throughout the cell (**Figure B.6**), shows that ethylene migrating to the electrolyte has a neutral charge, indicating the formation of gas, which is observed experimentally[262]. However, the ethylene molecule present in the nest phase is an anion or radical anion with a charge of -1.5e, and the charge decays as it enters the nest phase, mainly when it crosses the disperse phase, becoming finally neutral in the electrolyte. This electron transfer from the radical anion

species to intact electrolyte molecules is part of the SEI growth as suggested earlier.[52] When a group of atoms from the nest phase is extracted to calculate the charge, ethylene presents a charge of -0.5e, showing a negative charge of ethylene radical anions even when part of the electrolyte is isolated from the environment. The presence of non-decomposed electrolyte and the negative charge of ethylene indicate that further SEI growth including polymerization may happen around the nest phase. Previously reported DFT studies[28] showed that electron-rich environments exist previous to the oligomerization between radical ethylene species, as observed in the ethylene molecules present in the cells simulated here by ReaxFF calculations. This agreement supports the accuracy of the force field. At 2 ns, Li_2O and LiF segregate. Li_2O remains mainly at the bottom of the disperse phase, while LiF stays at the top of the same phase (**Figure 6.3**). This separation between nucleating phases may support the SEI distribution multilayer models proposed by Aurbach and collaborators.[43,44,243-245] The cluster that is formed on top the disperse phase retains Li_2O and LiF, but in addition there are compounds formed by polymerization of carbon monosulfide species resulting from the decomposition of Li-triflate. When the electrolyte does not contain Li-triflate, the SEI cluster formation is not observed during 2 ns of simulation, indicating a much slower kinetics in the absence of the salt.

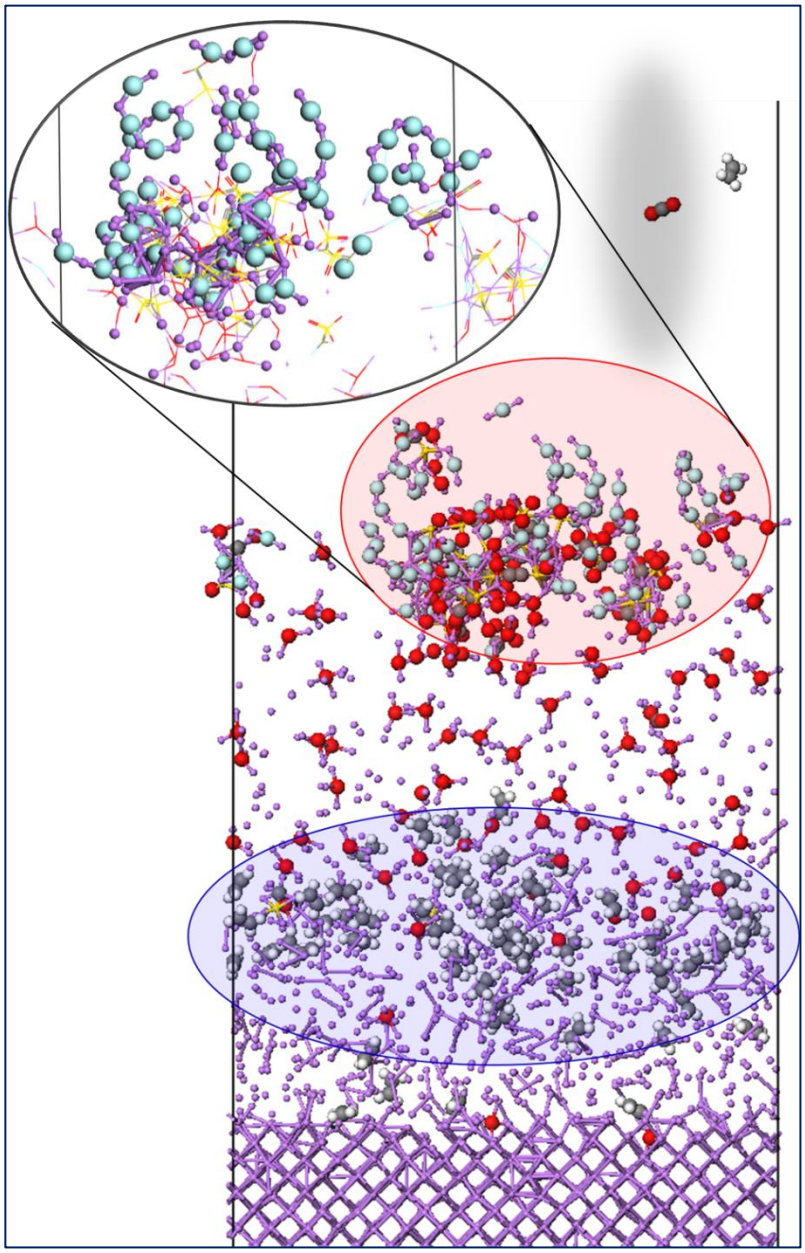

Figure 6.5: Distribution of species in the porous phase at 2 ns of simulation, electrolyte composed of DX and 1M lithium-triflate. Only part of the dense phase is shown at the bottom. The purple ellipsoid shows the presence of ethylene molecules or radicals. The pink circle illustrates the cluster formation integrated by LiF and initial nucleation of Li oxide molecules and C-S chains among other SEI species. Color code: Li: purple, O: red, C: gray, H: white, F: cyan and S: yellow.

The RPDFs of lithium with oxygen, fluorine and sulfur (**Figure B.7**) indicate that the first Li-X coordination shells peak at 3.15 Å, 2.3 Å and 3 Å for X = O, F, and S respectively. The integral of the RPDF from r =0 to the minimum after the first peak indicates that all the average coordination numbers (CNs) are smaller than or slightly above 1 in F and S, and a CN of ~ 4 atoms for O, which is in good agreement with the value obtained from experimental and theoretical calculations in the presence of EC and LiB salts [263-267]. For both F and S, Li coordinates with an average of 1.3 atoms. Higher CN for fluorine appears in longer time of simulations (e.g. 1.5 and 2ns). In the nest and disperse phases, Li and O have a low CN, which indicates that during the first 2 ns Li_2O is not formed, but a lithium peroxide component is formed.

The average charge distribution of Li atoms in the cell (**Figure 6.6**) indicates that the ReaxFF can well differentiate the charge distribution of Li in the different phases. In the dense phase, Li has an average charge smaller than 0.1e, which shows that the calculation identifies the metallic region as a neutral, while the porous phase is positively charged. Therefore, the anode provides the electrons that induce the decomposition and dissolution of the electrolyte. With the exception of 1:1 DOL:DMTFA, the size of the porous phase stabilizes around the same size with time, however, the porous phase grows with different rates depending on the electrolyte that is in contact with the anode. The charge analyses show that an approximate thickness of 20 Å of the dense phase is consumed to generate a porous phase of ~60Å thickness. The porous phase thickness stabilizes at 350, 180, 150, 350 and 200 ps in DOL, 1:1 DOL:DMTFA, 1:1 DOL:FEC, DX and DOL 1M Li-triflate, respectively.

When Li-triflate is present in the electrolyte (**Figure B.8**), the calculated average charge of Li atoms is not good enough to allow distinguishing the separation between the porous phase and the electrolyte (**Table B.1**, Supporting Information). However, it is possible to observe that the average charge in the porous phase is within 0.3-0.4e, while in the electrolyte is in the 0.5-0.6e range. The maximum Li charge in a region shows similar results when compared with the average charge, while the minimum Li charge indicates low values in the porous region, although slightly higher than in the dense phase, which further suggests that part of the porous phase may maintain similar characteristics of the Li-metal anode (e.g. formation of dead Li). The computed total charge helps distinguishing well the porous phase and the electrolyte, because of the high concentration of Li atoms in the porous phase, however the actual value of the total Li charge does not have a meaning itself, because it depends on the cell' size and the number of Li atoms. When analyzing the structure of the cluster presented in DX 1M Li-triflate on **Figure 6.7**, it is possible to observe the high concentration of F and O atoms, non-decomposed or partially decomposed salt, the structure of polymerized C-S monomer chains, and a high concentration of Li atoms. Nucleation of polymer chains from C-S monomers is observed only inside the clusters, indicating that the presence of the CS monomer affects the buildup of the cluster. On the other hand, O and F are inside and outside the cluster. Isolating the cluster from the system and calculating the charge of the elements, there are differences in the charges calculated using the Bader method and that of the ReaxFF (**Table B.1**). The elements S, C, and O present the most critical differences. For example, Bader analyses overestimate the charge of O elements,

although the charges of Li and F present similar results. Because ReaxFF is fitted to all-electron calculations, they could provide at least reasonable approximations [268,269]. However, as discussed in the Introduction, we emphasize that charge transfer effects should be better described by using a pseudoclassical treatment of explicit electrons, as done in eReaxFF.[34,35]

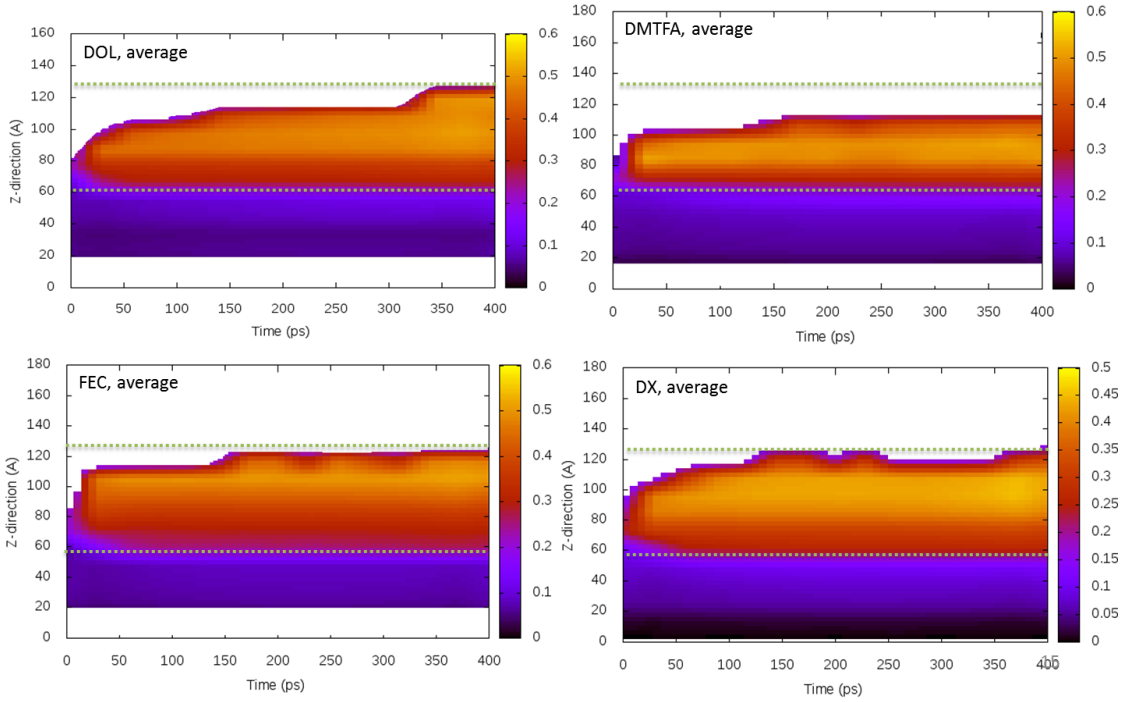

Figure 6.6: Time evolution of the average charge distribution of lithium in the z direction The electrolyte used are DOL, DOL:DMTFA, DOL:FEC and DX. The charges are given in electron units.

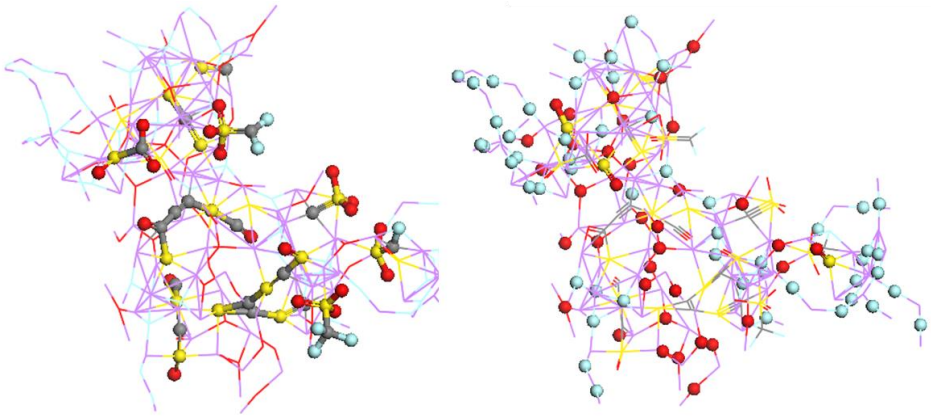

Figure 6.7: Structure of the cluster extracted from the disperse phase. The images highlight the presence of the elements F (light blue) and O (red); and the presence of non-decomposed salt and chains formed by reaction with organosulfides.

6.5. CONCLUSION

The buildup of the SEI layer was studied using ReaxFF in different scenarios to analyze the possible reactions and rearrangements taking place at the interface of the Li-metal anode surface with the electrolyte. The simulations with different electrolytes tested indicate that a porous phase develops immediately above the anode surface, which contains not only decomposed species due to electron transfer from the lithium surface but also intact electrolyte molecules. Over the porous phase, two additional surface films are formed: the nest phase and the disperse phase. The nest phase is an amorphous matrix structure of connected lithium atoms separated by nanochannels, through which the intact electrolyte and other products of its decomposition such as ethylene (molecules and radical anions) diffuse. In the disperse phase (the top layer in contact with the electrolyte), lithium atoms in a higher oxidation state are connected in networks nucleating the SEI blocks such as Li_2O and LiF or more complex structures. For example, at the interface with the electrolyte, a multicomponent cluster with a high Li

concentration was detected. An uneven distribution of Li exists in the nest phase and in the cluster formed in the disperse phase, which may deliver uneven distributions of electric field and consequently may lead to the formation of dendrite structures upon lithium deposition.

We emphasize a couple of points to clarify some limitations of our model. In this study, we identify the formation of nano-porous lithium coexisting with intact electrolyte molecules and species formed because of the decomposition of the electrolyte as described in the porous model. However, the porous structures in Refs. 26-27 are at least 1000 times larger than our observed structures. Thus we are only capturing the very beginning of the nucleation of complex phases. Second, the absence of an electric field in our simulations as discussed in the Introduction, limits our observations to the dissolution of the Li metal in the electrolyte phase. Future work will be focused on the effect of the applied potential and associated phenomena as has been discussed in the literature.[64] Finally, we admit that the length of the reported simulations (2 ns) only allows access to the very initial stages of Li-metal dissolution and reactions with the electrolyte. A dynamic evolution is definitely expected. However, capturing the behavior at this initial stage and the effect of the nature and composition of the electrolyte is important to set the conditions for more extended mesoscopic modeling able to reach longer time and length scales.

7. INVESTIGATION OF REACTIONS BETWEEN LITHIUM METAL ANODE AND THE ELECTROLYTE

7.1. SYNOPSIS

Some of the reactions are involved during the formation of the solid electrolyte interphase over a lithium metal surface, were evaluated using classical molecular dynamics and reactive force fields (ReaxFF) over a virtual lithium metal slab, covered by various electrolytes. The ReaxFF is able to reproduce some reactions that were previously detected using density functional theory. Additional reactions such as those between the fragments liberated by the decomposition of the electrolyte are also characterized. Some reactions were calculated by gas phase electronic structure DFT calculations in an electron-rich environment. Ab initio molecular dynamics simulations of the decomposition of highly concentrated Lithium trifluoromethanesulfonate (triflate) solutions in DOL solvent were carried out over a lithium-metal slab.

7.2. INTRODUCTION

Lithium batteries (LIBs) are used in many applications such as electric vehicles and electronic devices. Although graphite anodes in LIBs have been successfully commercialized, Li-metal anodes may increase the capacity of the anode going from 370 $Wh.kg^{-1}$ in the graphite anode to 3860 $Wh.kg^{-1}$ in the Li-metal anode [8-12]. Although Li-metal anodes have the potential to replace traditional anodes used in LIBs due to their high specific capacity, they pose safety hazards and reduced cycle life due to the formation of dendrites. Li usually has preferential sites to deposit over the anode and it

induces dendrites growth in the direction of the cathode, penetrating the separator and producing a short-circuitand catastrophic failure [13-16].

The solid electrolyte interphase (SEI) is expected to be an insulator film formed between the electrode and the electrolyte due to the decomposition of the electrolyte by Lithium attack. The decomposition reactions occur because the Lithium-metal anode has a chemical potential above the lowest unoccupied molecular orbital of the electrolyte molecules[17], thus the reaction produces species that stay attached to the electrode, forming insoluble salts that start building the SEI. The nature of the SEI plays an important role in the battery performance, and the formation of SEI causes irreversible Li loss, but the SEI usually becomes a protective layer against continuous degradation of the electrode and electrolyte[270]. The first step for the build-up of the SEI is the formation of pristine species such as Li_2O, LiF, and Li_2CO_3, that accumulate near the bulk electrode due to continuous decomposition of the species formed and the continuous solution and dissolution of the present species forms a porous SEI phase. When an electric field is applied, it may break the SEI due to morphological changes that cannot accommodate over the SEI. When the SEI breaks, it exposes the bare phase of the electrode, creating a preferential path for Li deposition, allowing dendrite growth. Thus, an understanding of the reactions that take place on the build-up of the SEI and the distribution of different elements on the SEI is important to understand how dendrite grow or polysulfide reactivity on the lithium-metal anode. The polysulfides, due to the shuttle of soluble lithium-sulfur salts (Li_2S_x, $3 < x < 8$) to the anode, degrade the electrode and create an SEI that has a very low ionic lithium diffusion[27,165,271].

The composition of the electrolyte is important to produce components that will reduce damages on the SEI during cycles. Electrolytes such as 1,3 dioxane (DOL) can form elastomers during the build-up of the SEI[43]. Electrolytes during decomposition, (e.g. DOL), produce radical species such as OCH_2CH_2, OCH_2CH_2O, and OCH_3. [272,273] These species react with the electrolyte and produce polymerization of the species involved in the reaction. This polymerization generates the elastomers that allow the SEI to accommodate to morphological changes[258-261]. In this work, the reactions detected in using ReaxFF were further investigated with electronic structure methods. Ab Initio Molecular Dynamics (AIMD) was used to study to understand lithium Trifluoromethanesulfonate (triflate) decomposition with a 5M concentration in DOL over a lithium-metal surface. A newer technique based on the ReaxFF, the eReaxFF[274,275] are an explicit electron technique coupled within ReaxFF. Although eReaxFF can better-calculated redox potential of species involved in the battery and can predict reactions between radicals that exist in a Li battery, the eReaxFF was not yet trained for atoms as S, F, and N.

7.3. COMPUTATIONAL METHODS

The ReaxFF calculates the partial energy to form a bond. The valence, lone pair, torsion, over coordination, under coordination and penalty energy, are calculated to determine the bond order, allowing the bond to break and consequently simulate reactions. Coulomb and van der Waals energy are also calculated by ReaxFF [128]. The Van der Waals energy is calculated by the Morse Potential, and the electronic charges

needed for evaluating the Coulomb electrostatic energy are obtained using the Charge Equilibration Method[247-250].

The ReaxFF was developed for the relationship between the C/H/O/S/Li/F/N atoms, the interactions among atoms were trained for LiBs materials [254,255,276]. Each cell was built with three different regions, which represent the solid lithium metal anode, the electrolyte and a bilayer of graphite. The thin graphite bilayer breaks the periodic boundary conditions (PBC) along the Z direction. The anode was obtained from the Li bcc structure with lattice parameter 3.442 Å[157,158], then the cell was cleaved along the [100] direction to build a slab with cell parameters of 55.2Å x 27.4Å x 67.2Å. Different solvents/additives have been tested, using as solvent 1,3 dioxolane (DOL), dimethyltrifluoroacetamide (DMTFA), ethylene carbonate (EC), fluoroethylene carbonate (FEC), dimethoxyethane (DME) and 1,4 dioxolane DX, and 1M of Trifluoromethanesulfonate (triflate) as salt was used in DOL and DXelectrolytes. Electrolytes tested include pure DOL (1.06g.cm^{-3}), DOL + 1M Li-triflate (1.06g.cm^{-3}), DOL:DMTFA (1:1, molar rate. 1.06g.cm^{-3}), DOL:EC (1:1, 1.20 g.cm^{-3}), DOL:FEC (1:1, 1.20 g.cm^{-3}), and pure DX (1.03g.cm^{-3}), DX + 1M Li-triflate (1.03g.cm^{-3}). After assembling the Li metal slab, the electrolyte, and the graphite layers, the simulation cell parameters changed to 55.2Å x 27.4Å x 164.8 Å.The simulations were carried out in the canonical ensemble at a constant number of particles N, volume V, and temperature T (NVT). The temperature was kept constant using the Nosé-Hoover thermostat[256] with a time step of 0.1 fs and a temperature of 300 K. In preview studies, we investigated the

evolution of the morphology of the Li-metal anode during Li metal dissolution (oxidation) [277].

High concentrated solutions of Li-triflate of ~4M in DOL were studied by AIMD simulations using the Vienna Ab-initio Simulation Package (VASP) interphase, within the plane-wave basis set approach[212-214,278]. Monkhorst-Pack k-point mesh [172] for the Brillouin zone (BZ) sampling were used to produce a k-point grid of 2×2×1. This plane-wave basis set is used to achieve both computational accuracy and efficiency with the cut-off energy set to 400 eV. Electron-ion interactions were described by the PAW pseudopotentials [169,170] as provided in the VASP databases. The Nosé thermostat was used to control the temperature oscillations during the simulation with a Nosé mass parameter of 0.5[216-218]. A conjugate-gradient algorithm was employed to relax the ions into their instantaneous ground state. Gaussian smearing with a width of 0.05 eV was also utilized. The convergence criteria for self-consistent electronic iteration and ionic relaxation were set to 10^{-4} eV and 10^{-3} eV, respectively. For the high concentration salt-electrolyte simulation, the lithium slab is also build up from a cleavage on the [100] surface with a thickness of 10.3Åx10.3Å, where 3 layers are fixed to represent to the bulk material, and 3 layers of the slab are allowed to relax over the surface. The electrolyte molecules (Li-triflate and DOL) were randomly placed, filling a vacuum of 20 Å with a density of 1.06g.cm^{-3}. Both in AIMD and ReaxFF simulations the electrolyte molecules were previously optimized using the Gaussian 09 (G09) package with a hybrid functional B3PW91 and the 6-311++G(p,d) basis set[279-281]. This level of theory was also used to calculate the Gibbs free energy of the molecules in an electron-

rich environment. In the electron-rich environment, the decomposition of the electrolyte was studied by adding electrons to the molecules, instead of implicitly add Li atoms to equilibrate the molecule's charge. The solvation effects were implicitly represented by the polarizable continuum model (PCM)[282] as implemented in the G09 software package using 1,3 Dioxolane as a solvent. After optimization of electrolyte molecules by DFT method, the electrolyte molecules have their positions optimized using[283,284] in the electrolyte, minimizing non-bonded energies. The Crystal Orbital Hamilton Population (COHP) and Crystal Overlap Hamilton Population (COOP) were calculated using the LOBSTER program[285,286] to understand the stability of the triflate bonds and its fragments during different times of High concentration Li-triflate simulation.

7.4. RESULTS AND DISCUSSION

When the electrolyte is in contact with the Li metal anode at open circuit potential, it instantaneously starts to decompose over the anode to form the species that will build the SEI. In all the electrolytes tested, the decomposition occurs exponentially during the first 100 ps of classical MD simulation time, and then the decomposition rate slows down. As shown in **Figure 7.1a**, the time evolution of species in 1,4 dioxane (DX) indicates that the main species present in the system are oxygen and ethylene. **Figure 7.1b**, for DOL, dioxymethane and ethylene are the most common species produced by the decomposition of DOL, while oxygen and formaldehyde appear in low concentration. DX is more reactive than DOL and also generates more oxygen, even though the initial amount of DOL is higher, this may be due to a certain stabilization of

O-CH_2-O in DOL. Because according to ReaxFF O-CH_2-O is relatively stable, it will slowly break yielding oxygen atoms or anions? that dissolve into the electrolyte. Therefore the concentration of species indicates that dioxymethane does not decompose fast in the anode, and compared with DX, it produces a smaller concentration of oxygen. When DOL is mixed with other electrolytes (1:1 DOL:X molar concentration, where X is another solvent), it is possible to observe that the reactivity of DOL changes. In other words, if the solvent added together with DOL is more reactive, it will consume Li thus reducing the amount of Li available to react with DOL (see **Figure C.1).** For electrolytes reacting faster than DOL, the electrolyte reduces the reactivity of DOL by consuming available Li In the case of ethylene carbonate (EC) and fluoroethylene carbonate (FEC) mixture, EC and FEC mixed with DOL reduce the reactivity of DOL. While in a mixture such as N,N-dimethyltrifluoroacetamide (DMTFA), DOL is more reactive. Therefore the simulations indicate that different solvents will not only contribute to a different distribution of species based on their different reactivities, but it also can stabilize radicals that may act on the formation of elastomers. The solvent will affect the SEI not only by the mechanism and species that it produces but also affecting the reactivity of other solvents.

In the case of DOL: FEC, after 500 ps of simulations, the formation of LiF was not observed during the decomposition of FEC as reported in the literature for LIBs[197,287-289]. The calculations indicate the following trend for the concentration of molecules O > CO_2 > CH_2CH_2, > O-CH_2-O. The decomposition of FEC is very similar to EC, breaking first carbon-oxygen bonds. Although the EC decomposition mechanism

that we most observed in ReaxFFsimulations produces more CO_2 than CO_3, both mechanism of EC decomposition is similar to those reported in literature[27,290-299]. However, the formation of CO_3 is more favorable than CO_2. According to ReaxFF, the decomposition of the DOL:EC electrolyte mostly produces the ethylene and oxygen radicals, followed by CO_2, O-CH_2-O, and 1,3-dioxolan-2-ylidene, indicating a predominance of one mechanism for EC decomposition. The breaking of the carbon-oxygen bond in the EC molecule to form 1,3-dioxolan-2-ylidene and oxygen is thermodynamically allowed in an electron-rich environment (see **Table A.2**). Because the simulations indicate a lower concentration of CO_3 than CO_2, this suggests that the mechanism that leads to CO_3 production is less favorable over lithium-metal than in Li-ion, thus in Li-ion batteries, others mechanisms of EC decomposition may be more favorable depending of the concentration of non-oxidized lithium atoms. The mechanism of decomposition of pure DOL and dimethoxyethane (DME) observed in the simulations (see **Figure C.2**) is also observed by Zhang et al. [300],[301]. In the simulations with DOL and DME each of the tree electrolytes tested, C-O bonds break from OCH_2 and O-CH_2-O producing CH_2. However, the composition of DOL, DX, and DME always produce a large amount of ethylene. These molecules may polymerize as detected experimentally, [258-261]. DX decomposes by breaking C-O bonds, producing ethylene and oxygen. The kinetic energy barriers calculated by Bedrov et al.[255] indicate similar values for ReaxFF and DFT calculations.

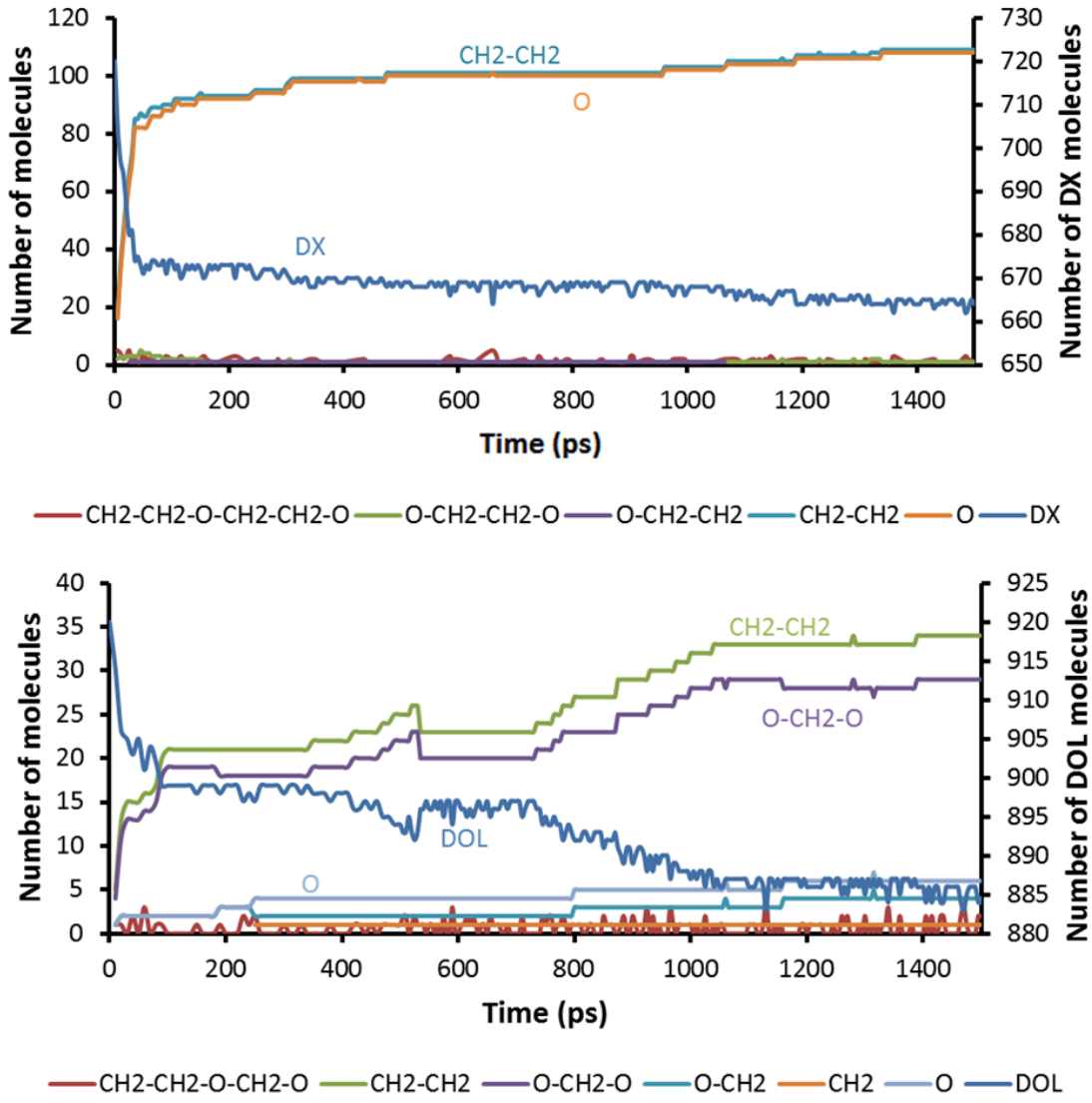

Figure 7.1: Results of classical MD simulations using ReaxFF. Evolution of the number of molecules over time, in the presence of pure DX (top) and pure DOL (bottom).

Lithium triflate (CF_3-SO_3) decomposed in many different ways (see **Figure C.3**). The most common mechanism for decomposition of triflate is the sequential breaking of C-F bonds, followed by the breaking of S-O bonds, while the C-S bond in the majority of the cases does not break. Nevertheless, it is possible to observe different mechanisms

of decomposition, which will deliver various possible intermediate species. However, those mechanisms in the majority of the cases will result in the formation of Li_2O and LiF, considering that oxygen and fluorine (that break from the electrolyte moleculesdecomposition) will produce insoluble inorganic salts as observed in preview studies[27,197,287,302-304]. In one of the possible mechanisms, the formation of CF_3 and SO_3 are observed after C-S bond breaking. Intermediate species also can react to generate other species. In one of the cases where two products of triflate react, it was possible to observe a carbon breaking from C-SO_2 forming C and SO_2, later this C reacts with S to form CS, just after breaking S-O bonds from SO_2. The exchange of atomic positions also happens in one of the species generated by triflate decomposition, where CF-SO_3 generates OCF-SO_2, therefore in the reaction S-O bond breaks to form a C-O bond. The C-O bond created in the reactions that yield species such as OCF-SO_2, can become free CO anion (or radical anion) in the electrolyte, and it can reduce the salt, consuming oxygen to produce CO_2.

The simulations indicate that CF_3-SO_3 is capable of reacting with the solvent (**Figure 7.2**). It was observed that the triflate salt could produce HFin the presence of DOL. One C-F bond breaks from the triflate, and the fluorine, removed from the salt, bonds to a hydrogen of a DOL molecule. Then the C-H bond breaks and liberates HF in the electrolyte. This mechanism indicates that triflate can react with the DOL to produce HF. In DX, it was also observed that fluorine could bond to DX through the formation of a F-H bond. One of the observed mechanisms, fluorine only temporarily bonds to DX and breaks again. In another mechanism, fluorine bonds to carbon from DX, the

molecule breaks one C-O bond from the same carbon, forming FCH_2-CH_2-O-CH_2-CH_2-O. The structure develops to generate the CH_2-O and CH_2-CH_2 species. The hydrolysis of salts (reactions with water) in LIBs has been observed in literature reactions with Li-hexafluorophosphate ($LiPF_6$) and Li-Bis(trifluoromethane)sulfonimide (LiTFSI). LiTFSI has a bigger resistance against hydrolysis than $LiPF_6$. Li-triflate has a certain resemblance with the atomistic configuration of LiTFSI. Interestingly, it also shows a similar mechanism of decomposition with that salt, breaking the C-F bonds. The hydrolysis mechanism proposed in the literature is in the presence of water[27,305-308]. However, in these simulations, HF species are found to appear without the presence of water, but by extraction of H from the solvent molecules. The exchange of oxygen from sulfur to carbon, as above mentioned, can generate CO anions during the decomposition salt fragments. One of the CO anions reacts with DX, consuming one oxygen molecule to produce CO_2 and breaking the DX molecule, which produces O-CH_2-CH_2. The O-CH_2-CH_2 supplies oxygen to SO_2-CO (which is a product of the exchange mechanism), producing SO_3-CO. Another exchange will happen with SO_3-CO, and the molecule becomes SO_2-CO_2.

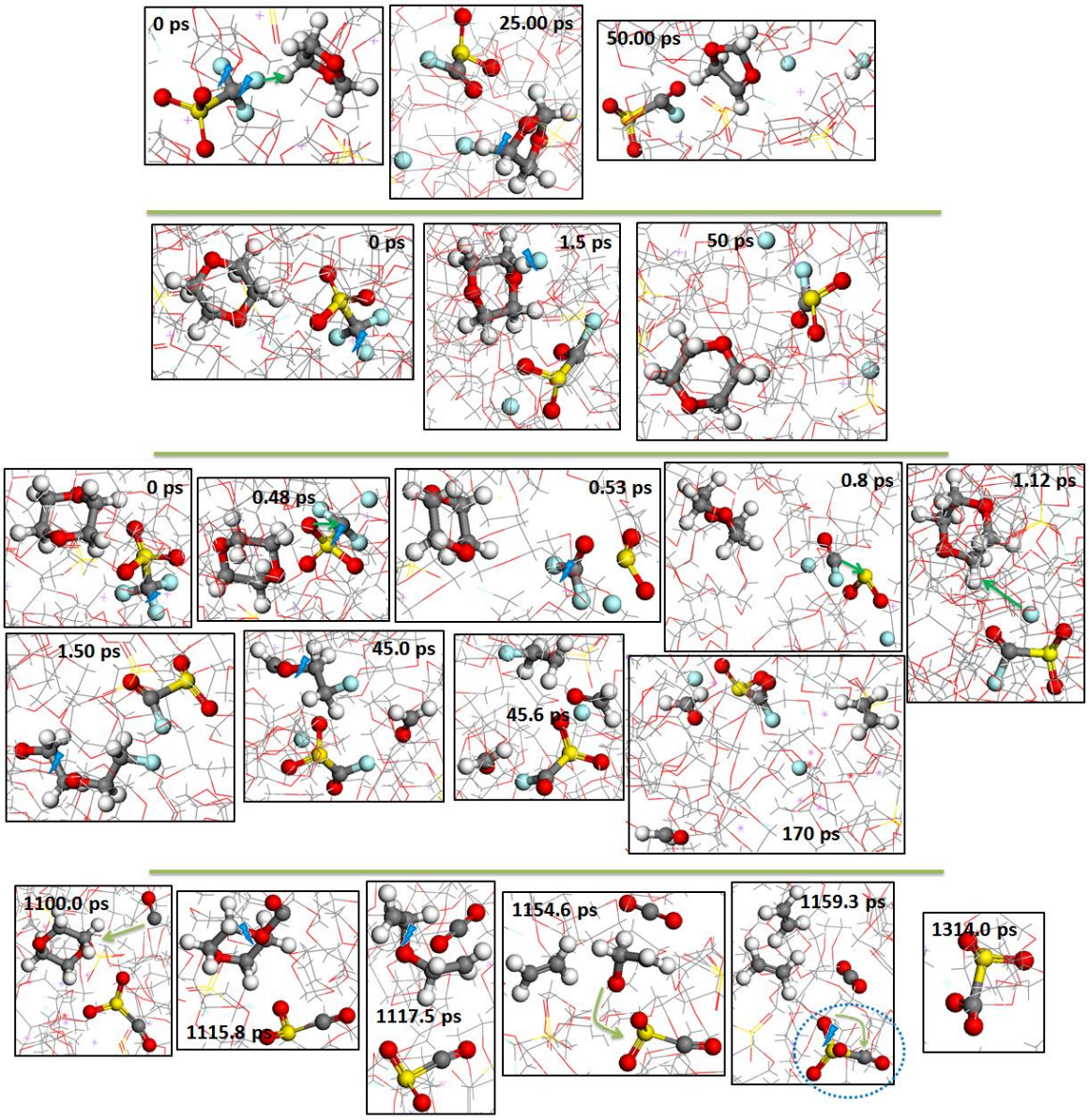

Figure 7.2: Mechanisms of reaction between the solvent and triflate, calculated by ReaxFF simulations. Carbon is colored by gray, fluorine by cyan, hydrogen by white, oxygen by red, sulfur by yellow and lithium is by purple dots.

Another important mechanism observed during the simulations is the polymerization of the CS species, reacting with other CS species or with species that are products of the decomposition of lithium triflate. Clusters were observed that locally

contain a high concentration of lithium atoms and poly(mono-carbonsulfide). Further analysis is necessary to determine if those clusters may play a role in the dendrite formation because the cluster has an uneven distribution of Li. Moreover, as proposed by Lu et al. [45], dendrites form due to an uneven distribution of lithium in the SEI and consequently an uneven distribution of the electric field, leading to a preferential path for lithium deposition and dendrite growth. Carbon disulfide (CS_2), have been used as an additive in lithium-sulfur batteries (Li-S), improving cycling and Coulombic efficiency. The mechanism proposed suggests that CS_2 can react with the anode and form polysulfide. Moreover, CS_2 creates a passivating layer over the lithium-metal anode against electrolyte decomposition, reducing the corrosion of the electrode [309,310]. The polymerization of CS isomers has been reported in the literature; those species can react with another CS and also CSO molecules to form different isomers (e.g.: $C\text{-}SO_3^{-3} + CS^{-2} = SO_3\text{-}C\text{-}C\text{-}S^{-2} + 3e^{-1}$). Alkali-metals, such as Na and Li, can be used to catalyze the reactions[310-316].

The polymerization of monocarbonsulfide is shown in **Figure 7.3**. The presence of CS radicals is due to the decomposition of triflate molecules, as above mentioned. After one molecule of triflate loses the fluorine atom, the species is attacked by a CS monomer, leading to the formation of an $SO_3\text{-}CF_2\text{-}S\text{-}C$ complex. Then the formed species sequentially loses the fluorine atoms to form $SO_3\text{-}C\text{-}S\text{-}C$. One of the C-S bonds breaks and the structure rearranges forming $SO_3\text{-}C\text{-}C\text{-}S$. In the next step, the structure loses two oxygens, forming O-S-C-C-S, which can exchange oxygen from one side to another by freeing one of oxygen in one side of the molecule, and bond with one of the

oxygen in the electrolyte, at the other side of the structure, therefore keeping the same formula. O-S-C-C-S reacts with another CS species forming O-S-C-C-S-C-S, which will be rearranged, loses the oxygen, rearranging to S-C-(CS)-S-C. The isomer formed will react with C-SO_3 forming SO_3-C-S-C-(CS)-S-C, which losses oxygen atoms with time. It is possible to observe that there is a tendency for the isomers $(CS)_n$ to keep polymerizing, by adding new CS monomers, rearranging the structure and losing oxygen and fluorine atoms of the newly formed isomers with time.

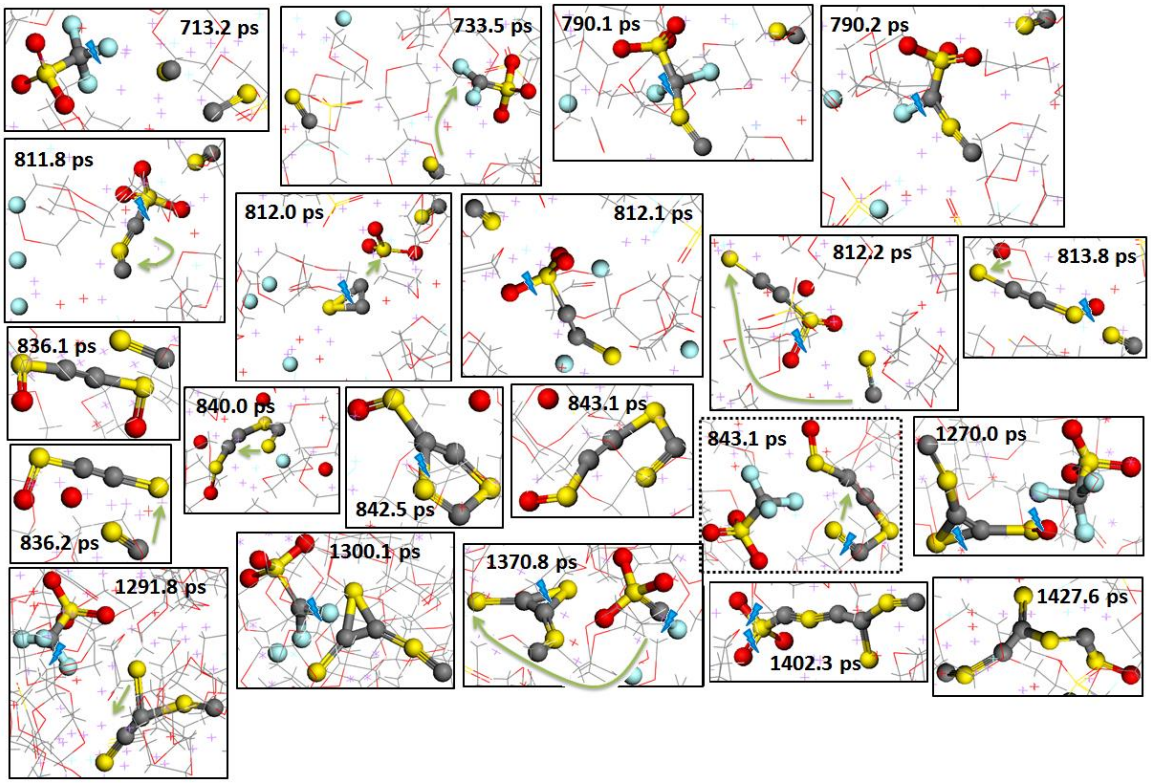

Figure 7.3: Mechanism of polymerization of carbon sulfide calculated by ReaxFF simulations. Carbon is colored gray, fluorine cyan, hydrogen white, oxygen red, sulfur yellow and lithium is represented by purple crosses.

To understand the decomposition of the electrolyte and compare the observed reaction using ReaxFF, DFT calculations of the reactions were carried out in some of the reactions. The calculations were done in a gas phase model using the b3pw91/6-311++g(d,p) method, and implicitly solvated by DOL (ξ=7.1, dielectric constant). The reactions were done by simulating an electron-rich environment, where Li metal is implicitly transferring electrons for the electrolyte to decompose. Electrochemical reactions using DFT calculations have already been investigated in literature to understand the electrolyte decomposition in an electron-rich environment[289,301,317,318]. The Gibbs free energy (at 298K) of the most stable anion of each molecule was used to calculate the proposed reactions Gibbs free energy (see **Table A.2**). The reactions were separated by groups, such as 1) Simple decomposition of salt; 2) Decomposition of solvent; 3) Exchange mechanism; 4) Decomposition of exchanged species; 5) Reactions between solvent and salt, and 6) Organosulfide polymerization and decomposition.

In the simple decomposition of the salt, the proposed reactions are done by progressively breaking each possible bond that exists on the triflate molecule, until it can completely break in individual species (carbon, fluorine, oxygen, and sulfur). The calculations indicate that the majority of the salt decomposition reactions are possible. The species $F_nC\text{-}SO_m$, F_nC, SO_m (where n and m are integer numbers between 0 and 3), CS, F, and O are thermodynamically favorable to decompose. The SO^{-2} species may not decompose into O^{-2} and S^{-2}, but it can react with C^{-4} to form CSO^{-2}. The reactions observed in the ReaxFF calculations (see **Figure C.3**) are thermodynamically favorable in the "simple decomposition of salt calculations".

On the decomposition of solvents calculations, it was investigated the reactions involving DOL, DME and DX solvents. Although the reactions were done in an electric-rich environment, the reactions assume the same tendency of bond breaking as observed in the literature, when the solvents are attacked by lithium progressively to obtain the mechanisms for decomposition[301,319]. The reactions observed in the ReaxFF calculations (see **Figure C.2**), they were also thermodynamic allowed in the "decomposition of solvents" calculations, except for the decomposition of OCH_2O^{-2} into OCH_2^{-1} and O^{-2}.

The "exchange mechanism" are the reactions in which the oxygen atoms originally bonded by the sulfur, break their bond with sulfur and bond to carbon atoms, creating species such as CF_nO_m-SO_i. Where n,m and i are integers that go from 0 to 2. Those reactions were also observed in the ReaxFF calculations (see **Figure 7.2**). The transformation reaction of $CFSO_3^{-3}$ into OCF-SO_2^{-1} is not allowed thermodynamically in accordance with the "exchange mechanism" calculations. Although this reaction happens in the ReaxFF calculations, the presence of many different ions on the electrolyte may change the dielectric constant of the environment, which could allow the reaction due to the low Gibbs free energy value involved (4.13kcal/mol). Moreover, the majority of the reactions involving the "exchange mechanism" are thermodynamically favorable according to DFT calculations in an electron-rich environment. The number of electrons added to the simulations for each reaction in an electron-rich environment can be seen on **Table A.2**.

The reactions calculated by ReaxFF related to the decomposition of the fragments involved in the exchange mechanism reactions, and also those between the

solvent and salt fragments (see **Figure 7.2**) were examined with DFT calculations. Reactions such as the formation of HF by the salt attack, or exchange of oxygen from S to C in triflate fragments, among others; are thermodynamically favorable. The results indicate that ReaxFF gives a good inside of the reactions that may be involved in the decomposition of salt and solvent and reactions between them. However, the reactions of carbosulfide polymerization (**Figure 7.3**) in some of the cases are not thermodynamically favorable. This may be associated with a possible exaggeration of the energy involved in a carbon-sulfur bond. In this hypothesis, the ReaxFF may consider the carbon-sulfur bond more stable, which can give the following consequence: The decomposition of triflate in CF_3 and SO_3 species may be kinetically affected, consequently, the amounts of CF_3 and SO_3 are reduced. Moreover, the ReaxFF may be stabilizing the organosulfide polymerization. Since the polymerization of CS_2 and CS species are observed in literature[310-316], an organosulfide may not be formed in an electron-rich environment. To understand the effect of ReaxFF in stabilizing the carbon-sulfur bond, the energies, in a DFT gas phase model, were scanned by changing the distance between carbon and sulfur, and optimizing to local minimum energy, the position of other atoms from $Li_2CF_3SO_3$. From each frame of the geometry configuration during scanning of $Li_2CF_3SO_3$ decomposition, a single point calculation was done using the position of the same atoms (see **Figure 7.4**). Comparing the DFT calculation with the ReaxFF calculation, it is possible to observe that in ReaxFF the carbon-sulfur bond is more stable than in DFT calculation. Also, the barrier for $Li_2CF_3SO_3$ break a carbon-sulfur bond is higher in ReaxFF than in DFT calculations. Although ReaxFF

demonstrates to have reasonable results in many observable reactions, training for energy calculation of $Li_2CF_3SO_3$ and other salts should be developed to better fit with DFT calculations, which can be done in future work.

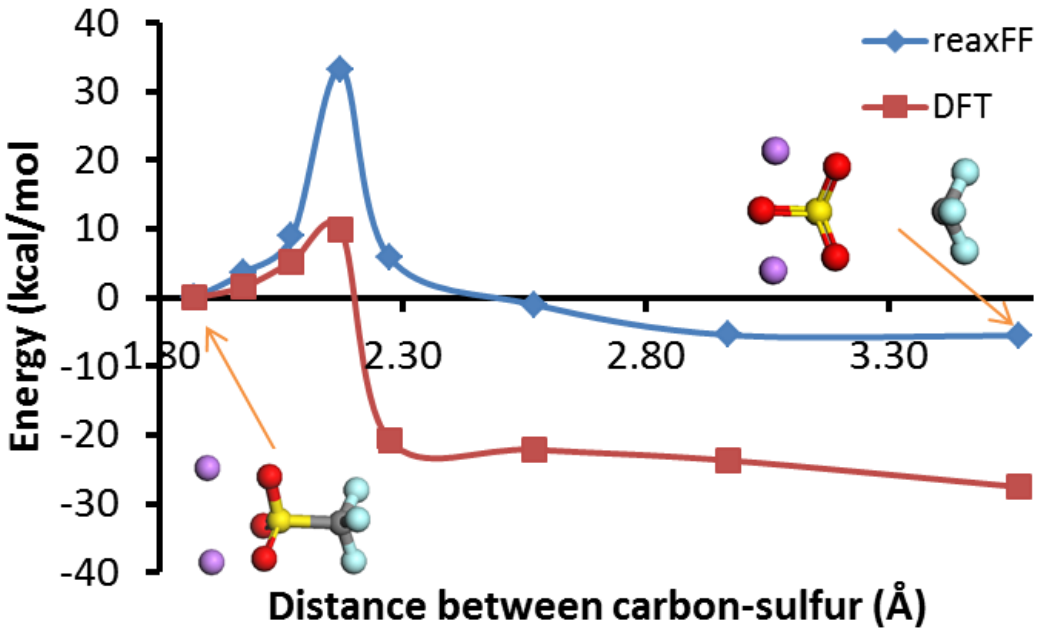

Figure 7.4: Scanned Energy profile by carbon-sulfur distance in DFT and ReaxFF.

The Li-triflate decomposition was evaluated by AIMD simulations in high concentration salt electrolyte of 5M in DOL solvent. Although the high concentration of triflate, it was possible to observe that during 20 ps of simulation, the decomposition of only one triflate molecule (see **Figure 7.5**) occurs. Different from ReaxFF, AIMD simulations show that the first bond to break on triflate is a carbon-sulfur bond. A triflate molecule starts to break at 7.0ps, where the oxygen atoms from the triflate molecule coordinate with lithium atoms from the anode. While in ReaxFF it would be expected to

break oxygen-sulfur bonds, in AIMD oxygen-sulfur bonds are stable. During the simulation period (20ps), SO_3 does not decompose over the surface, even though it is attached to the metal surface. The fragment CF_3, decomposes step by step forming F in every carbon-fluorine bond, and thus it is formed CF_2 and F at 9.0fs, CF at -9.2ps and C and F at 9.5ps. On the triflate, a negative charge volume concentrates (electron accumulation) between carbon-sulfur bond, which is the first one to break. SO_3 over all the frames has similar charge density distribution, where positive charge volume (electron depletion) accumulates around sulfur, and negative charge volume surrounds the oxygen atoms. CF_3 has a similar distribution of charges to SO_3, with positive charge volume encapsulating the C atoms, while CF_2 and CF have a more complex charge distribution.

The crystal orbital overlap population (COOP) is obtained by multiplying the overlap population by the Density of States, giving a dimension of bonding strength. The positive values of COOP give bonding interaction, while negative values give antibonding interaction. Therefore, the higher is the integral of COOP, the stronger is the bond between two atoms. As COOP measures the projection of DOS over the overlap population, the same can be done to the Hamiltonian of each element to obtain the crystal orbital Hamiltonian population. In the COHP, negative values will represent bonding interactions and positive values the antibonding interactions. Thus, the more negative is the integral of the COHP between two atoms, the stronger is the bond between them. The integrals of the COHP and COOP functions were done for some timeframes of **Figure 7.6**. Moreover, we can consider that the closer to the zero energy

value is the COHP and COOP integral, the weaker is the bond and the values of COOP and COHP go to zero when the atom is not bonded. The values of the COHP and COOP integrals for each bond that originally belongs to the same triflate molecule were tracked. Sulfur-carbon bond in the triflate (7.0ps) has the COHP closest to zero, and together with carbon-fluorine bonds, has the COOP closes to zero. This explains why in AIMD simulations the carbon-sulfur bond is the first to break over the anode. SO_3 has the furthest values from zero for COHP and COOP integral, what corroborates for the stability of the molecule and additionally corroborates the reasons for a non-observable decomposition of SO_3 in AIMD. When analyzing the distance evolution of carbon-sulfur and carbon-fluorine bonds (See **Figure C.4**), a destabilization of the carbon-fluorine bond happens between 7.9ps and 8.7ps, to finally break; thus the changes in the configuration that happens after 7.7ps affects change the values of COHP and COOP, as can be observed at 8.6ps on **Figure 7.6.** The carbon-fluorine bond that breaks from CF_3 has the smallest COOP, but does not have the weakest bond when seen the COHP value, thus the values that we obtained form COOP predicts better the bond that should breaks than COHP. CF_2 and CF also break the carbon-fluorine bond that is less unstable according to COHP and COOP integral results, thus CF_2 and CF have breaks the bonds closest to zero value for COHP and COOP integral.

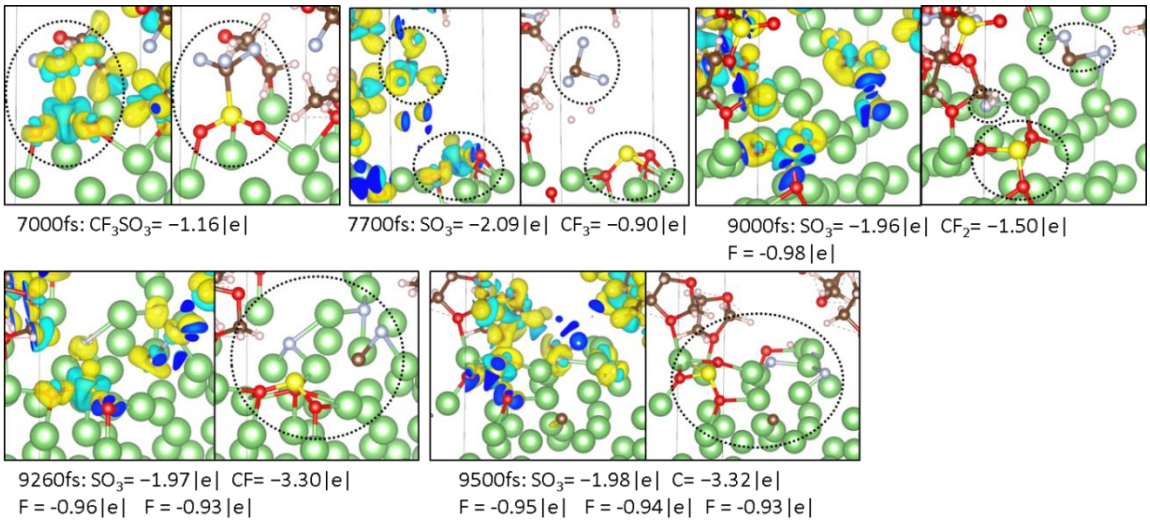

Figure 7.5: Decomposition of Triflate on Li metal anode over time, the charge of the fragments and charge density difference iso-surface with a 0.0175|e| value. The yellow iso-surface represents the concentration of negative charges, while the blue iso-surface confines positive charges. The atoms are colored in such a way that C is brown, F is blue, H is white, O is red and S is yellow.

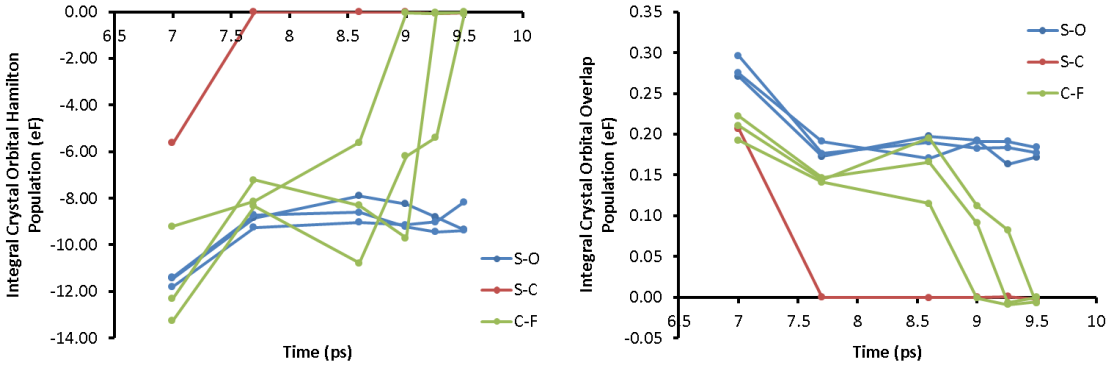

Figure 7.6: The Crystal Orbital Hamilton Population (COHP) and Crystal Orbital Overlap Population (COOP) of every bond from a triflate. *Left*) COHP of triflate and *Right*) COOP of triflate. In blue are the S-O bonds, in red S-C bond and in green C-F bonds.

7.5. CONCLUSION

The reactions happening between the lithium metal anode and different electrolytes were investigated. It is possible to observe that some solvents are more reactive than others, such as EC is more reactive than DOL. The reactivity of the

solvents changes for solvent mixtures, for example, the mixture DOL:EC, the reactivity of DOL slows down when compared to the pure DOL solvent. In general, the decomposition of the solvents tested gives species such as CH_2CH_2, OCH_2O, O, among others.

The decomposition of Lithium triflate by ReaxFF goes in the majority of the cases by progressively breaking carbon-fluorine and oxygen-sulfur bonds. Moreover, the decomposition yields a large number of monocarbosulfide, which appears to polymerize. Comparing the scanning energy of triflate decomposition by breaking carbon-sulfur bond in ReaxFF and DFT calculations, the calculations indicate that ReaxFF is over stabilizing the carbon-sulfur bond. This over stabilization of carbon-sulfur bond is also correlated with the polymerization of monocarbonsulfides, that it is probably non realistic. AIMD with a high concentration of triflate breaks first the carbon-sulfur bond and then sequentially breaks carbon-fluorine bonds, while oxygen-sulfur bonds are more stable. COHP and COOP integral correlate well with the sequence of decomposition of triflate, indicating carbon-sulfur bond as the weakest bond. Thus ReaxFF calculations may be delivering an excess of monocarbonsulfide.

ReaxFF also predicts reactions between the salt and the electrolyte fragments, and between salt fragments. The solvent can supply hydrogen to react with fluorine from the salt to form hydrogen fluoride. Also, in the triflate oxygen can exchange position, breaking an oxygen-sulfur bond and forming a carbon-oxygen bond. Therefore, ReaxFF indicates that variousreactions can happen between different fragments produced from electrolyte decomposition. The reactions in the majority of the cases are corroborated by

DFT calculations in electron-rich environments. However, some of them (such as the polymerization of CS bonds) are proved to be an artifact of the ReaxFF parametrization.

8. CONCLUSIONS AND RECOMMENDATIONS

The simulations involving decomposition of polysulfide (PS) on lithium bare surfaces indicate a high reactivity of the PS. Because of the formation of Li_2S over the anode surface, the decomposition of the first PS reduces the amount of Li sites available, but PS molecules keep being high reactive on the surface. Although Li_2S_8 decomposes in all the observed cases, it first breaks forming a chain with three and another with two S atoms. However the continuous decomposition of the PS can happen in different ways. The orientation of S on the Li_2S is parallel to the Li (110) plane, thus the Li_2S will have the orientation on the surface depending on the original cleavage plane of the lithium bare phase. The initial decomposition of PS on the Li (110) plane is faster than that in the (111) plane, which may be explained due to an initial high concentration of Li ions at the surface. However, over time PS agglomeration leads to cluster formation in the electrolyte far from the Li (110) plane., Instead, the PSs stay attached to the (111) plane allowing the PSs to decompose faster. Moreover, Li_2S can better accommodate in the (111) plane than in the (110) plane. Thus, the decomposition of PS will be no uniform due to the different orientation of the Li metal facets at the interface with the electrolyte.

The nature of the species that can be present in the SEI, such as Li_2O, Li_2SO_4, Li_3N, and LiF affects the decomposition of the polysulfide. These species are produced due to the decomposition of salts and additives such as LiTFSI and lithium nitrate. The simulations with a pure inorganic SEI covering the anode with a thickness of around 6Å, it indicates that not only the nature of the species that compose the SEI is important but also the exposed facet of the SEI modifies the reactivity of the PS (e.g. PS is more

reactive in $Li_2O(110)$ than in $Li_2O(100)$). The simulations indicate a higher reactivity of the PS in presence of some species (e.g. PS is more reactive in Li_3N than in Li_2O). When the thickness of the SEI is increased to around 10Å, the decomposition of PS still occurs. The density of states of Li_2O changes after PS decomposition, revealing changes in the elctronic structure of the covered surface. Since the electrons are transferring from the anode to the PS through the SEI, a change in the electronic properties of the SEI explains why the PS stabilizes over the surface in the simulations. Therefore, the inorganic layer of the SEI is important to reduce or eliminate the decomposition of the PS. And since the reactivity of PS changes depends on the species present in the SEI, the proportion and specific mixtures of additives and salts in the electrolyte should be controlled to achieve a higher concentration of some desirable species. One example of such additive is $LiNO_3$ in Li-S batteries that can prevent dendrite and create a SEI layer that protects against PS decomposition in the anode[320].

The simulations using ReaxFF suggest formation of nanoporous regions close to the anode surface (nest phase), and in zones close to the electrolyte a more even distribution of Li ions (disperse phase). In these phases, intact electrolyte molecules co-exist with species produced by decomposition of the electrolyte. The distribution of Li in the nest phase is uneven, and when an electric field is applied, it may result in an uneven distribution of charges. Additionally, a non-uniform distribution of the electric field may create preferential sites for Li ions deposition. Segregation of the products such as oxides and ethylene-derived fragments is observed, where ethylene (radicals and anions)

concentrate in the nest phase and oxides in the disperse phase. Further diffusion of these nucleated products is observed, which may lead to the final SEI distribution of phases.

The decomposition mechanism of the solvents using ReaxFF gives the same path of decomposition of solvent reported earlier by using DFT methods. However, ReaxFF does not necessarily produce the most thermodynamically and kinetically favorable products. The reactions pathways of electrolyte decomposition using DFT calculations indicate that the reactions predicted by ReaxFF are thermodynamically possible. However, some reactions such as polymerization of carbon monosulfide are not thermodynamically possible according to DFT calculations. Thus the ReaxFF prediction of this polymerization indicates that although overall ReaxFF does a sufficiently accurate job; some extra training would be needed to better simulate some specific electrolyte molecules decomposition.

We observed that the deposition of Cs and Li occur preferentially on the same Li cleavage surface and they prefer to deposit in low coordination sites. Thus, both atoms will mainly deposit on the nucleating dendrite surfaces. Cs maintains a positive charge when depositing above a Li surface. Cs will also deposit preferentially on the bare phase than in the SEI layer, consequently covering damaged regions of the SEI. The most stable site for Cs deposition is in the grain boundaries of the SEI. Since the positively charged CS will cover the nucleating dendrite, it will create repulsion for Li ions that will migrate to deposit to other regions without Cs coverage. Therefore, Cs will reduce the preferential path for Li deposition consequently reducing the probability of dendrite formation.

Possible avenues for continuation of this research could be the investigation of $LiNO_3$ decomposition on the Lithium-metal anode in order to understand the role of additives on the SEI build-up and how it can react with PS species. Another important aspect that should be investigated is the electric field effect. This additional study would provide a deeper understanding of the mechanism that delivers a dendrite growth. Explicit electrons reactive force fields (eReaxFF) extend the ReaxFF concept to incorporate explicit -electron or -hole description. ReaxFF cannot calculate accurate the electrons affinities and ionization potentials of the molecules, because of ReaxFF cannot calculate electrons transfer properly, moreover electrons only can be implicitly transferred by bond formation. Moreover, eReaxFF can better describe redox reactions that occur in lithium-metal anode surfaces[251,252]. Thus eReaxFF is another possibility to investigate the dendrite nucleation problem. Finally, ab-initio methods should be employed to investigate the further nucleation of the SEI, diffusion of ions through the SEI (e.g. Li-ion diffusion on different grain boundaries) and Li deposition in the anode under an electric-field.

REFERENCES

(1) Armand, M.; Tarascon, J. M. Building better batteries. *Nature* **2008**, *451*, 652-657.

(2) Yang, Z.; Gu, L.; Hu, Y.-S.; Li, H. Atomic-Scale Structure-Property Relationships in Lithium Ion Battery Electrode Materials. *Annual Review of Materials Research* **2017**, *47*, 175-198.

(3) Etacheri, V.; Marom, R.; Elazari, R.; Salitra, G.; Aurbach, D. Challenges in the development of advanced Li-ion batteries: a review. *Energy & Environmental Science* **2011**, *4*, 3243-3262.

(4) Aurbach, D.; McCloskey, B. D.; Nazar, L. F.; Bruce, P. G. Advances in understanding mechanisms underpinning lithium–air batteries. *Nature Energy* **2016**, *1*, 16128.

(5) Zhang, K.; Lee, G. H.; Park, M.; Li, W.; Kang, Y. M. Recent developments of the lithium metal anode for rechargeable non-aqueous batteries. *Advanced Energy Materials* **2016**.

(6) Park, M. S.; Ma, S. B.; Lee, D. J.; Im, D.; Doo, S.-G.; Yamamoto, O. A highly reversible lithium metal anode. *Scientific reports* **2014**, *4*, 3815.

(7) Armstrong, A. R.; Bruce, P. G. Synthesis of layered LiMnO2 as an electrode for rechargeable lithium batteries. *Nature* **1996**, *381*, 499-500.

(8) Zheng, G.; Lee, S. W.; Liang, Z.; Lee, H.-W.; Yan, K.; Yao, H.; Wang, H.; Li, W.; Chu, S.; Cui, Y. Interconnected hollow carbon nanospheres for stable lithium metal anodes. *Nature nanotechnology* **2014**, *9*, 618-623.

(9) Zhang, C.; Wu, H. B.; Yuan, C.; Guo, Z.; Lou, X. W. D. Confining sulfur in double-shelled hollow carbon spheres for lithium–sulfur batteries. *Angewandte Chemie* **2012**, *124*, 9730-9733.

(10) Hochgatterer, N.; Schweiger, M.; Koller, S.; Raimann, P.; Wöhrle, T.; Wurm, C.; Winter, M. Silicon/graphite composite electrodes for high-capacity anodes: influence of binder chemistry on cycling stability. *Electrochemical and Solid-State Letters* **2008**, *11*, A76-A80.

(11) Scrosati, B.; Garche, J. Lithium batteries: Status, prospects and future. *Journal of Power Sources* **2010**, *195*, 2419-2430.

(12) Stevens, D.; Dahn, J. High Capacity Anode Materials for Rechargeable Sodium-Ion Batteries. *Journal of the Electrochemical Society* **2000**, *147*, 1271-1273.

(13) Gilaki, M.; Francis, A.; Bautista, D.; Avdeev, I. In *Tilte*2016; American Society of Mechanical Engineers.

(14) Lisbona, D.; Snee, T. A review of hazards associated with primary lithium and lithium-ion batteries. *Process Safety and Environmental Protection* **2011**, *89*, 434-442.

(15) Tobishima, S.-i.; Yamaki, J.-i. A consideration of lithium cell safety. *Journal of Power Sources* **1999**, *81*, 882-886.

(16) Ritchie, A.; Howard, W. Recent developments and likely advances in lithium-ion batteries. *Journal of Power Sources* **2006**, *162*, 809-812.

(17) Goodenough, J. B.; Kim, Y. Challenges for rechargeable Li batteries. *Chemistry of materials* **2009**, *22*, 587-603.

(18) Dedryvère, R.; Leroy, S.; Martinez, H.; Blanchard, F.; Lemordant, D.; Gonbeau, D. XPS valence characterization of lithium salts as a tool to study electrode/electrolyte interfaces of Li-ion batteries. *The Journal of Physical Chemistry B* **2006**, *110*, 12986-12992.

(19) Scheers, J.; Fantini, S.; Johansson, P. A review of electrolytes for lithium–sulphur batteries. *Journal of Power Sources* **2014**, *255*, 204-218.

(20) Yim, T.; Park, M.-S.; Yu, J.-S.; Kim, K. J.; Im, K. Y.; Kim, J.-H.; Jeong, G.; Jo, Y. N.; Woo, S.-G.; Kang, K. S. Effect of chemical reactivity of polysulfide toward carbonate-based electrolyte on the electrochemical performance of Li–S batteries. *Electrochimica Acta* **2013**, *107*, 454-460.

(21) Gao, J.; Lowe, M. A.; Kiya, Y.; Abruña, H. c. D. Effects of liquid electrolytes on the charge–discharge performance of rechargeable lithium/sulfur batteries: electrochemical and in-situ X-ray absorption spectroscopic studies. *The Journal of Physical Chemistry C* **2011**, *115*, 25132-25137.

(22) Zhang, S. S. Liquid electrolyte lithium/sulfur battery: fundamental chemistry, problems, and solutions. *Journal of Power Sources* **2013**, *231*, 153-162.

(23) Aurbach, D.; Zinigrad, E.; Cohen, Y.; Teller, H. A short review of failure mechanisms of lithium metal and lithiated graphite anodes in liquid electrolyte solutions. *Solid State Ionics* **2002**, *148*, 405-416.

(24) Gireaud, L.; Grugeon, S.; Laruelle, S.; Yrieix, B.; Tarascon, J. M. Lithium metal stripping/plating mechanisms studies: A metallurgical approach. *Electrochemistry Communications* **2006**, *8*, 1639-1649.

(25) Ota, H.; Shima, K.; Ue, M.; Yamaki, J.-i. Effect of vinylene carbonate as additive to electrolyte for lithium metal anode. *Electrochimica Acta* **2004**, *49*, 565-572.

(26) Lee, Y. M.; Seo, J. E.; Lee, Y.-G.; Lee, S. H.; Cho, K. Y.; Park, J.-K. Effects of Triacetoxyvinylsilane as SEI Layer Additive on Electrochemical Performance of Lithium Metal Secondary Battery. *Electrochemical and Solid-State Letters* **2007**, *10*, A216-A219.

(27) Camacho-Forero, L. E.; Smith, T. W.; Bertolini, S.; Balbuena, P. B. Reactivity at the Lithium–Metal Anode Surface of Lithium–Sulfur Batteries. *The Journal of Physical Chemistry C* **2015**, *119*, 26828-26839.

(28) Camacho-Forero, L. E.; Balbuena, P. B. Elucidating electrolyte decomposition under electron-rich environments at the lithium-metal anode. *Physical Chemistry Chemical Physics* **2017**.

(29) Togasaki, N.; Momma, T.; Osaka, T. Enhanced cycling performance of a Li metal anode in a dimethylsulfoxide-based electrolyte using highly concentrated lithium salt for a lithium−oxygen battery. *Journal of Power Sources* **2016**, *307*, 98-104.

(30) Li, W.; Yao, H.; Yan, K.; Zheng, G.; Liang, Z.; Chiang, Y.-M.; Cui, Y. The synergetic effect of lithium polysulfide and lithium nitrate to prevent lithium dendrite growth. *Nat Commun* **2015**, *6*.

(31) Hirai, T.; Yoshimatsu, I.; Yamaki, J. i. Effect of additives on lithium cycling efficiency. *Journal of The Electrochemical Society* **1994**, *141*, 2300-2305.

(32) Shiraishi, S.; Kanamura, K.; Takehara, Z. i. Surface Condition Changes in Lithium Metal Deposited in Nonaqueous Electrolyte Containing HF by Dissolution-Deposition Cycles. *Journal of The Electrochemical Society* **1999**, *146*, 1633-1639.

(33) Xiong, S.; Xie, K.; Diao, Y.; Hong, X. Properties of surface film on lithium anode with LiNO3 as lithium salt in electrolyte solution for lithium–sulfur batteries. *Electrochimica Acta* **2012**, *83*, 78-86.

(34) Xu, K.; von Cresce, A. Interfacing electrolytes with electrodes in Li ion batteries. *Journal of Materials Chemistry* **2011**, *21*, 9849-9864.

(35) Winter, M. The solid electrolyte interphase–the most important and the least understood solid electrolyte in rechargeable Li batteries. *Zeitschrift für physikalische Chemie* **2009**, *223*, 1395-1406.

(36) Peled, E.; Tow, D. B.; Merson, A.; Gladkich, A.; Burstein, L.; Golodnitsky, D. Composition, depth profiles and lateral distribution of materials in the SEI built on HOPG-TOF SIMS and XPS studies. *Journal of power sources* **2001**, *97*, 52-57.

(37) Bridges, C. A.; Sun, X.-G.; Zhao, J.; Paranthaman, M. P.; Dai, S. In situ observation of solid electrolyte interphase formation in ordered mesoporous hard carbon

by small-angle neutron scattering. *The Journal of Physical Chemistry C* **2012**, *116*, 7701-7711.

(38) Zhuang, G. V.; Xu, K.; Yang, H.; Jow, T. R.; Ross, P. N. Lithium ethylene dicarbonate identified as the primary product of chemical and electrochemical reduction of EC in 1.2 M LiPF6/EC: EMC electrolyte. *The Journal of Physical Chemistry B* **2005**, *109*, 17567-17573.

(39) Mukherjee, P.; Lagutchev, A.; Dlott, D. D. In situ probing of solid-electrolyte interfaces with nonlinear coherent vibrational spectroscopy. *Journal of The Electrochemical Society* **2012**, *159*, A244-A252.

(40) Nakagawa, H.; Domi, Y.; Doi, T.; Ochida, M.; Tsubouchi, S.; Yamanaka, T.; Abe, T.; Ogumi, Z. In situ Raman study on degradation of edge plane graphite negative-electrodes and effects of film-forming additives. *Journal of Power Sources* **2012**, *206*, 320-324.

(41) Sacci, R. L.; Black, J. M.; Balke, N.; Dudney, N. J.; More, K. L.; Unocic, R. R. Nanoscale Imaging of Fundamental Li Battery Chemistry: Solid-Electrolyte Interphase Formation and Preferential Growth of Lithium Metal Nanoclusters. *Nano Letters* **2015**, *15*, 2011-2018.

(42) Chen, Y.; Ouyang, C.; Song, L.; Sun, Z. Electrical and lithium ion dynamics in three main components of solid electrolyte interphase from density functional theory study. *The Journal of Physical Chemistry C* **2011**, *115*, 7044-7049.

(43) Aurbach, D. Review of selected electrode–solution interactions which determine the performance of Li and Li ion batteries. *Journal of Power Sources* **2000**, *89*, 206-218.

(44) Cohen, Y. S.; Cohen, Y.; Aurbach, D. Micromorphological studies of lithium electrodes in alkyl carbonate solutions using in situ atomic force microscopy. *The Journal of Physical Chemistry B* **2000**, *104*, 12282-12291.

(45) Lu, D.; Shao, Y.; Lozano, T.; Bennett, W. D.; Graff, G. L.; Polzin, B.; Zhang, J.; Engelhard, M. H.; Saenz, N. T.; Henderson, W. A. Failure mechanism for fast-charged lithium metal batteries with liquid electrolytes. *Advanced Energy Materials* **2015**, *5*.

(46) López, C. M.; Vaughey, J. T.; Dees, D. W. Morphological transitions on lithium metal anodes. *Journal of The Electrochemical Society* **2009**, *156*, A726-A729.

(47) Wood, K. N.; Kazyak, E.; Chadwick, A. F.; Chen, K.-H.; Zhang, J.-G.; Thornton, K.; Dasgupta, N. P. Dendrites and pits: untangling the complex behavior of lithium metal anodes through operando video microscopy. *ACS central science* **2016**, *2*, 790-801.

(48) Wood, K. N.; Kazyak, E.; Chadwick, A. F.; Chen, K.-H.; Zhang, J.-G.; Thornton, K.; Dasgupta, N. P. In *Tilte*2017; The Electrochemical Society.

(49) Xu, X.; Wang, S.; Wang, H.; Xu, B.; Hu, C.; Jin, Y.; Liu, J.; Yan, H. The suppression of lithium dendrite growth in lithium sulfur batteries: A review. *Journal of Energy Storage* **2017**, *13*, 387-400.

(50) Jana, A.; Ely, D. R.; García, R. E. Dendrite-separator interactions in lithium-based batteries. *Journal of Power Sources* **2015**, *275*, 912-921.

(51) Arbizzani, C.; Gabrielli, G.; Mastragostino, M. Thermal stability and flammability of electrolytes for lithium-ion batteries. *Journal of Power Sources* **2011**, *196*, 4801-4805.

(52) Aurbach, D.; Talyosef, Y.; Markovsky, B.; Markevich, E.; Zinigrad, E.; Asraf, L.; Gnanaraj, J. S.; Kim, H.-J. Design of electrolyte solutions for Li and Li-ion batteries: a review. *Electrochimica Acta* **2004**, *50*, 247-254.

(53) Zhang, S. S. A review on the separators of liquid electrolyte Li-ion batteries. *Journal of Power Sources* **2007**, *164*, 351-364.

(54) Xie, K.; Wei, W.; Yuan, K.; Lu, W.; Guo, M.; Li, Z.; Song, Q.; Liu, X.; Wang, J.-G.; Shen, C. Toward dendrite-free lithium deposition via structural and interfacial synergistic effects of 3D graphene@ Ni scaffold. *ACS applied materials & interfaces* **2016**, *8*, 26091-26097.

(55) Fergus, J. W. Ceramic and polymeric solid electrolytes for lithium-ion batteries. *Journal of Power Sources* **2010**, *195*, 4554-4569.

(56) Rao, M.; Geng, X.; Li, X.; Hu, S.; Li, W. Lithium-sulfur cell with combining carbon nanofibers–sulfur cathode and gel polymer electrolyte. *Journal of power sources* **2012**, *212*, 179-185.

(57) Yu, B.-C.; Park, K.; Jang, J.-H.; Goodenough, J. B. Cellulose-based porous membrane for suppressing Li dendrite formation in lithium–sulfur battery. *ACS Energy Letters* **2016**, *1*, 633-637.

(58) Chi, S. S.; Liu, Y.; Song, W. L.; Fan, L. Z.; Zhang, Q. Prestoring Lithium into Stable 3D Nickel Foam Host as Dendrite-Free Lithium Metal Anode. *Advanced Functional Materials* **2017**, *27*.

(59) Liang, Z.; Lin, D.; Zhao, J.; Lu, Z.; Liu, Y.; Liu, C.; Lu, Y.; Wang, H.; Yan, K.; Tao, X. Composite lithium metal anode by melt infusion of lithium into a 3D conducting scaffold with lithiophilic coating. *Proceedings of the National Academy of Sciences* **2016**, *113*, 2862-2867.

(60) Zhang, A.; Fang, X.; Shen, C.; Liu, Y.; Zhou, C. A carbon nanofiber network for stable lithium metal anodes with high Coulombic efficiency and long cycle life. *Nano Research* **2016**, *9*, 3428-3436.

(61) Liu, Y.; Lin, D.; Liang, Z.; Zhao, J.; Yan, K.; Cui, Y. Lithium-coated polymeric matrix as a minimum volume-change and dendrite-free lithium metal anode. *Nature communications* **2016**, *7*, 10992.

(62) Lee, H.; Lee, D. J.; Kim, Y.-J.; Park, J.-K.; Kim, H.-T. A simple composite protective layer coating that enhances the cycling stability of lithium metal batteries. *Journal of Power Sources* **2015**, *284*, 103-108.

(63) Ma, G.; Wen, Z.; Wu, M.; Shen, C.; Wang, Q.; Jin, J.; Wu, X. A lithium anode protection guided highly-stable lithium–sulfur battery. *Chemical Communications* **2014**, *50*, 14209-14212.

(64) Chen, L.; Shaw, L. L. Recent advances in lithium–sulfur batteries. *Journal of Power Sources* **2014**, *267*, 770-783.

(65) Xu, G.; Ding, B.; Pan, J.; Nie, P.; Shen, L.; Zhang, X. High performance lithium–sulfur batteries: advances and challenges. *Journal of Materials Chemistry A* **2014**, *2*, 12662-12676.

(66) Xiong, S.; Kai, X.; Hong, X.; Diao, Y. Effect of LiBOB as additive on electrochemical properties of lithium–sulfur batteries. *Ionics* **2012**, *18*, 249-254.

(67) Liang, X.; Wen, Z.; Liu, Y.; Wu, M.; Jin, J.; Zhang, H.; Wu, X. Improved cycling performances of lithium sulfur batteries with LiNO3-modified electrolyte. *Journal of Power Sources* **2011**, *196*, 9839-9843.

(68) Trofimov, B. A.; Markova, M. V.; Morozova, L. V.; Prozorova, G. F.; Korzhova, S. A.; Cho, M. D.; Annenkov, V. V.; Al'bina, I. M. Protected bis (hydroxyorganyl) polysulfides as modifiers of Li/S battery electrolyte. *Electrochimica Acta* **2011**, *56*, 2458-2463.

(69) Zhang, X. Q.; Cheng, X. B.; Chen, X.; Yan, C.; Zhang, Q. Fluoroethylene carbonate additives to render uniform Li deposits in lithium metal batteries. *Advanced Functional Materials* **2017**, *27*.

(70) Kim, J. S.; Yoo, D. J.; Min, J.; Shakoor, R. A.; Kahraman, R.; Choi, J. W. Poreless Separator and Electrolyte Additive for Lithium–Sulfur Batteries with High Areal Energy Densities. *ChemNanoMat* **2015**, *1*, 240-245.

(71) Li, W.; Yao, H.; Yan, K.; Zheng, G.; Liang, Z.; Chiang, Y.-M.; Cui, Y. The synergetic effect of lithium polysulfide and lithium nitrate to prevent lithium dendrite growth. *Nature communications* **2015**, *6*, 7436.

(72) Jeong, S.-K.; Seo, H.-Y.; Kim, D.-H.; Han, H.-K.; Kim, J.-G.; Lee, Y. B.; Iriyama, Y.; Abe, T.; Ogumi, Z. Suppression of dendritic lithium formation by using concentrated electrolyte solutions. *Electrochemistry Communications* **2008**, *10*, 635-638.

(73) Ding, F.; Xu, W.; Graff, G. L.; Zhang, J.; Sushko, M. L.; Chen, X.; Shao, Y.; Engelhard, M. H.; Nie, Z.; Xiao, J. Dendrite-free lithium deposition via self-healing electrostatic shield mechanism. *Journal of the American Chemical Society* **2013**, *135*, 4450-4456.

(74) Ellis, B. L.; Lee, K. T.; Nazar, L. F. Positive electrode materials for Li-ion and Li-batteries. *Chemistry of Materials* **2010**, *22*, 691-714.

(75) Wang, J.-Z.; Lu, L.; Choucair, M.; Stride, J. A.; Xu, X.; Liu, H.-K. Sulfur-graphene composite for rechargeable lithium batteries. *Journal of Power Sources* **2011**, *196*, 7030-7034.

(76) Aurbach, D.; Pollak, E.; Elazari, R.; Salitra, G.; Kelley, C. S.; Affinito, J. On the surface chemical aspects of very high energy density, rechargeable Li–sulfur batteries. *Journal of The Electrochemical Society* **2009**, *156*, A694-A702.

(77) Ji, X.; Lee, K. T.; Nazar, L. F. A highly ordered nanostructured carbon–sulphur cathode for lithium–sulphur batteries. *Nature materials* **2009**, *8*, 500.

(78) Mikhaylik, Y. V.; Akridge, J. R. Polysulfide shuttle study in the Li/S battery system. *Journal of the Electrochemical Society* **2004**, *151*, A1969-A1976.

(79) Yang, Y.; Zheng, G.; Misra, S.; Nelson, J.; Toney, M. F.; Cui, Y. High-capacity micrometer-sized Li2S particles as cathode materials for advanced rechargeable

lithium-ion batteries. *Journal of the American Chemical Society* **2012**, *134*, 15387-15394.

(80) Chen, Y.-X.; Kaghazchi, P. Metalization of Li 2 S particle surfaces in Li–S batteries. *Nanoscale* **2014**, *6*, 13391-13395.

(81) Yang, Y.; Zheng, G.; Cui, Y. Nanostructured sulfur cathodes. *Chemical Society Reviews* **2013**, *42*, 3018-3032.

(82) Schneider, H.; Gollub, C.; Weiß, T.; Kulisch, J.; Leitner, K.; Schmidt, R.; Safont-Sempere, M. M.; Mikhaylik, Y.; Kelley, T.; Scordilis-Kelley, C. On the electrode potentials in lithium-sulfur batteries and their solvent-dependence. *Journal of The Electrochemical Society* **2014**, *161*, A1399-A1406.

(83) Hofmann, A. F.; Fronczek, D. N.; Bessler, W. G. Mechanistic modeling of polysulfide shuttle and capacity loss in lithium–sulfur batteries. *Journal of Power Sources* **2014**, *259*, 300-310.

(84) Zhang, B.; Qin, X.; Li, G.; Gao, X. Enhancement of long stability of sulfur cathode by encapsulating sulfur into micropores of carbon spheres. *Energy & Environmental Science* **2010**, *3*, 1531-1537.

(85) Li, X.; Cao, Y.; Qi, W.; Saraf, L. V.; Xiao, J.; Nie, Z.; Mietek, J.; Zhang, J.-G.; Schwenzer, B.; Liu, J. Optimization of mesoporous carbon structures for lithium–sulfur battery applications. *Journal of Materials Chemistry* **2011**, *21*, 16603-16610.

(86) Liang, C.; Dudney, N. J.; Howe, J. Y. Hierarchically structured sulfur/carbon nanocomposite material for high-energy lithium battery. *Chemistry of Materials* **2009**, *21*, 4724-4730.

(87) Zheng, W.; Liu, Y.; Hu, X.; Zhang, C. Novel nanosized adsorbing sulfur composite cathode materials for the advanced secondary lithium batteries. *Electrochimica Acta* **2006**, *51*, 1330-1335.

(88) Su, Y.-S.; Fu, Y.; Manthiram, A. Self-weaving sulfur–carbon composite cathodes for high rate lithium–sulfur batteries. *Physical Chemistry Chemical Physics* **2012**, *14*, 14495-14499.

(89) Manthiram, A.; Su, Y.-S.: Binder-free sulfur—carbon nanotube composite cathodes for rechargeable lithium—sulfur batteries and methods of making the same. Google Patents, 2015.

(90) Zheng, G.; Yang, Y.; Cha, J. J.; Hong, S. S.; Cui, Y. Hollow carbon nanofiber-encapsulated sulfur cathodes for high specific capacity rechargeable lithium batteries. *Nano letters* **2011**, *11*, 4462-4467.

(91) Ji, L.; Rao, M.; Aloni, S.; Wang, L.; Cairns, E. J.; Zhang, Y. Porous carbon nanofiber–sulfur composite electrodes for lithium/sulfur cells. *Energy & Environmental Science* **2011**, *4*, 5053-5059.

(92) Guo, J.; Xu, Y.; Wang, C. Sulfur-impregnated disordered carbon nanotubes cathode for lithium–sulfur batteries. *Nano letters* **2011**, *11*, 4288-4294.

(93) Ye, H.; Yin, Y.-X.; Xin, S.; Guo, Y.-G. Tuning the porous structure of carbon hosts for loading sulfur toward long lifespan cathode materials for Li–S batteries. *Journal of Materials Chemistry A* **2013**, *1*, 6602-6608.

(94) Tao, X.; Chen, X.; Xia, Y.; Huang, H.; Gan, Y.; Wu, R.; Chen, F. Highly mesoporous carbon foams synthesized by a facile, cost-effective and template-free

Pechini method for advanced lithium–sulfur batteries. *Journal of Materials Chemistry A* **2013**, *1*, 3295-3301.

(95) Wei, S.; Zhang, H.; Huang, Y.; Wang, W.; Xia, Y.; Yu, Z. Pig bone derived hierarchical porous carbon and its enhanced cycling performance of lithium–sulfur batteries. *Energy & Environmental Science* **2011**, *4*, 736-740.

(96) Zhang, B.; Lai, C.; Zhou, Z.; Gao, X. Preparation and electrochemical properties of sulfur–acetylene black composites as cathode materials. *Electrochimica Acta* **2009**, *54*, 3708-3713.

(97) Jayaprakash, N.; Shen, J.; Moganty, S. S.; Corona, A.; Archer, L. A. Porous hollow carbon@ sulfur composites for high-power lithium–sulfur batteries. *Angewandte Chemie* **2011**, *123*, 6026-6030.

(98) Yuan, L.; Yuan, H.; Qiu, X.; Chen, L.; Zhu, W. Improvement of cycle property of sulfur-coated multi-walled carbon nanotubes composite cathode for lithium/sulfur batteries. *Journal of Power Sources* **2009**, *189*, 1141-1146.

(99) Song, M.-S.; Han, S.-C.; Kim, H.-S.; Kim, J.-H.; Kim, K.-T.; Kang, Y.-M.; Ahn, H.-J.; Dou, S.; Lee, J.-Y. Effects of nanosized adsorbing material on electrochemical properties of sulfur cathodes for Li/S secondary batteries. *Journal of the Electrochemical Society* **2004**, *151*, A791-A795.

(100) Zhang, Y.; Zhao, Y.; Yermukhambetova, A.; Bakenov, Z.; Chen, P. Ternary sulfur/polyacrylonitrile/Mg 0.6 Ni 0.4 O composite cathodes for high performance lithium/sulfur batteries. *Journal of Materials Chemistry A* **2013**, *1*, 295-301.

(101) Choi, Y.; Jung, B.; Lee, D.; Jeong, J.; Kim, K.; Ahn, H.; Cho, K.; Gu, H. Electrochemical properties of sulfur electrode containing nano Al2O3 for lithium/sulfur cell. *Physica Scripta* **2007**, *2007*, 62.

(102) Ji, X.; Evers, S.; Black, R.; Nazar, L. F. Stabilizing lithium–sulphur cathodes using polysulphide reservoirs. *Nature communications* **2011**, *2*, 325.

(103) Evers, S.; Yim, T.; Nazar, L. F. Understanding the nature of absorption/adsorption in nanoporous polysulfide sorbents for the Li–S battery. *The Journal of Physical Chemistry C* **2012**, *116*, 19653-19658.

(104) Yang, Y.; Yu, G.; Cha, J. J.; Wu, H.; Vosgueritchian, M.; Yao, Y.; Bao, Z.; Cui, Y. Improving the performance of lithium–sulfur batteries by conductive polymer coating. *ACS nano* **2011**, *5*, 9187-9193.

(105) Li, W.; Zheng, G.; Yang, Y.; Seh, Z. W.; Liu, N.; Cui, Y. High-performance hollow sulfur nanostructured battery cathode through a scalable, room temperature, one-step, bottom-up approach. *Proceedings of the National Academy of Sciences* **2013**, *110*, 7148-7153.

(106) Jin, Z.; Xie, K.; Hong, X.; Hu, Z.; Liu, X. Application of lithiated Nafion ionomer film as functional separator for lithium sulfur cells. *Journal of Power Sources* **2012**, *218*, 163-167.

(107) Huang, J.-Q.; Zhang, Q.; Peng, H.-J.; Liu, X.-Y.; Qian, W.-Z.; Wei, F. Ionic shield for polysulfides towards highly-stable lithium–sulfur batteries. *Energy & environmental science* **2014**, *7*, 347-353.

(108) Zhang, S. S. Role of LiNO3 in rechargeable lithium/sulfur battery. *Electrochimica Acta* **2012**, *70*, 344-348.

(109) Zhang, S. S. Effect of discharge cutoff voltage on reversibility of lithium/sulfur batteries with LiNO3-contained electrolyte. *Journal of The Electrochemical Society* **2012**, *159*, A920-A923.

(110) Lee, J. G.: *Computational materials science: an introduction*; Crc Press, 2016.

(111) Cai, W.; Li, J.; Yip, S.: 1.09 - Molecular Dynamics. In *Comprehensive Nuclear Materials*; Konings, R. J. M., Ed.; Elsevier: Oxford, 2012; pp 249-265.

(112) Leach, A. R.: *Molecular Modelling: Principles and Applications*; Second ed.; Prentice Hall: Harlow, England, 2001.

(113) Verlet, L. Computer" experiments" on classical fluids. I. Thermodynamical properties of Lennard-Jones molecules. *Physical review* **1967**, *159*, 98.

(114) Hoover, W. G. Constant-pressure equations of motion. *Physical Review A* **1986**, *34*, 2499.

(115) Nosé, S. An extension of the canonical ensemble molecular dynamics method. *Molecular Physics* **1986**, *57*, 187-191.

(116) Frenkel, D.; Smit, B.: Understanding molecular simulation: From algorithms to applications. Elsevier (formerly published by Academic Press), 2002; Vol. 1; pp 1-638.

(117) Slater, J. C. The current state of solid-state and molecular theory. *International Journal of Quantum Chemistry* **1967**, *1*, 37-102.

(118) *Cerius2 User Guide*; Molecular Simulations Inc.: San Diego, CA, 1997.

(119) Dawid, T.; Christian, D. L.; Nikolaos, R.; Natalia, M.; Lev, K. Temperature control in molecular dynamic simulations of non-equilibrium processes. *Journal of Physics: Condensed Matter* **2010**, *22*, 074205.

(120) Schneider, T.; Stoll, E. Molecular-dynamics study of a three-dimensional one-component model for distortive phase transitions. *Physical Review B* **1978**, *17*, 1302-1322.

(121) Bussi, G.; Parrinello, M. Accurate sampling using Langevin dynamics. *Physical Review E* **2007**, *75*, 056707.

(122) Berendsen, H. J.; Postma, J. v.; van Gunsteren, W. F.; DiNola, A.; Haak, J. Molecular dynamics with coupling to an external bath. *The Journal of chemical physics* **1984**, *81*, 3684-3690.

(123) Andersen, H. C. Molecular dynamics simulations at constant pressure and/or temperature. *The Journal of chemical physics* **1980**, *72*, 2384-2393.

(124) Braga, C.; Travis, K. P. A configurational temperature Nosé-Hoover thermostat. *The Journal of chemical physics* **2005**, *123*, 134101.

(125) Shinoda, W.; Shiga, M.; Mikami, M. Rapid estimation of elastic constants by molecular dynamics simulation under constant stress. *Physical Review B* **2004**, *69*, 134103.

(126) Parrinello, M.; Rahman, A. Polymorphic transitions in single crystals: A new molecular dynamics method. *Journal of Applied physics* **1981**, *52*, 7182-7190.

(127) Martyna, G. J.; Tobias, D. J.; Klein, M. L. Constant pressure molecular dynamics algorithms. *The Journal of Chemical Physics* **1994**, *101*, 4177-4189.

(128) Chenoweth, K.; Van Duin, A. C.; Goddard, W. A. ReaxFF reactive force field for molecular dynamics simulations of hydrocarbon oxidation. *The Journal of Physical Chemistry A* **2008**, *112*, 1040-1053.

(129) Mortier, W. J.; Van Genechten, K.; Gasteiger, J. Electronegativity equalization: application and parametrization. *Journal of the American Chemical Society* **1985**, *107*, 829-835.

(130) Busch, P.; Heinonen, T.; Lahti, P. Heisenberg's uncertainty principle. *Physics Reports* **2007**, *452*, 155-176.

(131) Kohn, W.; Sham, L. J. Self-consistent equations including exchange and correlation effects. *Physical review* **1965**, *140*, A1133.

(132) Kohanoff, J.: *Electronic structure calculations for solids and molecules: theory and computational methods*; Cambridge University Press, 2006.

(133) Sholl, D. S.; Steckel, J. A.: *What is density functional theory?*; Wiley Online Library, 2009.

(134) Fiolhais, C.; Nogueira, F.; Marques, M. A.: *A primer in density functional theory*; Springer Science & Business Media, 2003; Vol. 620.

(135) Monkhorst, H. J.; Pack, J. D. Special points for Brillouin-zone integrations. *Physical review B* **1976**, *13*, 5188.

(136) Hacene, M.; Anciaux-Sedrakian, A.; Rozanska, X.; Klahr, D.; Guignon, T.; Fleurat-Lessard, P. Accelerating VASP electronic structure calculations using graphic processing units. *Journal of computational chemistry* **2012**, *33*, 2581-2589.

(137) Zhou, L. Progress and problems in hydrogen storage methods. *Renewable and Sustainable Energy Reviews* **2005**, *9*, 395-408.

(138) Tachan, Z.; Rühle, S.; Zaban, A. Dye-sensitized solar tubes: A new solar cell design for efficient current collection and improved cell sealing. *Sol Energ Mat Sol C* **2010**, *94*, 317-322.

(139) Lu, L.; Yang, H.; Burnett, J. Investigation on wind power potential on Hong Kong islands—an analysis of wind power and wind turbine characteristics. *Renewable Energy* **2002**, *27*, 1-12.

(140) Tarascon, J. M. Key challenges in future Li-battery research. *Philos T R Soc A* **2010**, *368*, 3227-3241.

(141) Tarascon, J. M.; Armand, M. Issues and challenges facing rechargeable lithium batteries. *Nature* **2001**, *414*, 359-367.

(142) Lu, L.; Han, X.; Li, J.; Hua, J.; Ouyang, M. A review on the key issues for lithium-ion battery management in electric vehicles. *J Power Sources* **2013**, *226*, 272-288.

(143) Thackeray, M. M.; Wolverton, C.; Isaacs, E. D. Electrical energy storage for transportation-approaching the limits of, and going beyond, lithium-ion batteries. *Energy & Environmental Science* **2012**, *5*, 7854-7863.

(144) Bruce, P. G.; Hardwick, L. J.; Abraham, K. M. Lithium-air and lithium-sulfur batteries. *Mrs Bulletin* **2011**, *36*, 506-512.

(145) Bruce, P. G.; Freunberger, S. A.; Hardwick, L. J.; Tarascon, J.-M. Li-O2 and Li-S batteries with high energy storage. *Nat Mater* **2012**, *11*, 19-29.

(146) Son, Y.; Lee, J. S.; Son, Y.; Jang, J. H.; Cho, J. Recent Advances in Lithium Sulfide Cathode Materials and Their Use in Lithium Sulfur Batteries. *Advanced Energy Materials* **2015**.

(147) Ji, X.; Nazar, L. F. Advances in Li-S batteries. *Journal of Materials Chemistry* **2010**, *20*, 9821-9826.

(148) Yuan, L.; Qiu, X.; Chen, L.; Zhu, W. New insight into the discharge process of sulfur cathode by electrochemical impedance spectroscopy. *J Power Sources* **2009**, *189*, 127-132.

(149) Barchasz, C.; Leprêtre, J.-C.; Alloin, F.; Patoux, S. New insights into the limiting parameters of the Li/S rechargeable cell. *J Power Sources* **2012**, *199*, 322-330.

(150) Viswanathan, V.; Thygesen, K. S.; Hummelshøj, J.; Nørskov, J. K.; Girishkumar, G.; McCloskey, B.; Luntz, A. Electrical conductivity in Li2O2 and its role in determining capacity limitations in non-aqueous Li-O2 batteries. *The Journal of chemical physics* **2011**, *135*, 214704.

(151) Bruce, P. G.; Freunberger, S. A.; Hardwick, L. J.; Tarascon, J. M. Li-O-2 and Li-S batteries with high energy storage. *Nature Materials* **2012**, *11*, 19-29.

(152) Bruce, P. G.; Freunberger, S. A.; Hardwick, L. J.; Tarascon, J.-M. Li-O-2 and Li-S batteries with high energy storage. *Nature Materials* **2012**, *11*, 19-29.

(153) Scheers, J.; Fantini, S.; Johansson, P. A review of electrolytes for lithium-sulphur batteries. *Journal of Power Sources* **2014**, *255*, 204-218.

(154) Chen, Y.-X.; Kaghazchi, P. Metalization of Li2S particle surfaces in Li-S batteries. *Nanoscale* **2014**, *6*, 13391-13395.

(155) Schneider, H.; Gollub, C.; Weiss, T.; Kulisch, J.; Leitner, K.; Schmidt, R.; Safont-Sempere, M. M.; Mikhaylik, Y.; Kelley, T.; Scordilis-Kelley, C.; Laramie, M.; Du, H. On the Electrode Potentials in Lithium-Sulfur Batteries and Their Solvent-Dependence. *Journal of the Electrochemical Society* **2014**, *161*, A1399-A1406.

(156) Hofmann, A. F.; Fronczek, D. N.; Bessler, W. G. Mechanistic modeling of polysulfide shuttle and capacity loss in lithium-sulfur batteries. *Journal of Power Sources* **2014**, *259*, 300-310.

(157) Anderson, M. S.; Swenson, C. A. Experimental equations of state for cesium and lithium metals to 20 kbar and the high-pressure behavior of the alkali metals. *Physical Review B* **1985**, *31*, 668-680.

(158) Doll, K.; Harrison, N. M.; Saunders, V. R. A density functional study of lithium bulk and surfaces. *Journal of Physics: Condensed Matter* **1999**, *11*, 5007.

(159) Frisch, M. J.; Trucks, G. W.; Schlegel, H. B.; Scuseria, G. E.; Robb, M. A.; Cheeseman, J. R.; Scalmani, G.; Barone, V.; Mennucci, B.; Petersson, G. A.; Nakatsuji, H.; Caricato, M.; Li, X.; Hratchian, H. P.; Izmaylov, A. F.; Bloino, J.; Zheng, G.; Sonnenberg, J. L.; Hada, M.; Ehara, M.; Toyota, K.; Fukuda, R.; Hasegawa, J.; Ishida, M.; Nakajima, T.; Honda, Y.; Kitao, O.; Nakai, H.; Vreven, T.; Montgomery Jr., J. A.; Peralta, J. E.; Ogliaro, F. o.; Bearpark, M. J.; Heyd, J.; Brothers, E. N.; Kudin, K.

N.; Staroverov, V. N.; Kobayashi, R.; Normand, J.; Raghavachari, K.; Rendell, A. P.; Burant, J. C.; Iyengar, S. S.; Tomasi, J.; Cossi, M.; Rega, N.; Millam, N. J.; Klene, M.; Knox, J. E.; Cross, J. B.; Bakken, V.; Adamo, C.; Jaramillo, J.; Gomperts, R.; Stratmann, R. E.; Yazyev, O.; Austin, A. J.; Cammi, R.; Pomelli, C.; Ochterski, J. W.; Martin, R. L.; Morokuma, K.; Zakrzewski, V. G.; Voth, G. A.; Salvador, P.; Dannenberg, J. J.; Dapprich, S.; Daniels, A. D.; Farkas, Ã. d. n.; Foresman, J. B.; Ortiz, J. V.; Cioslowski, J.; Fox, D. J.: Gaussian 09. Gaussian, Inc.: Wallingford, CT, USA, 2009.

(160) Becke, A. D. Density-functional thermochemistry. III. The role of exact exchange. *The Journal of Chemical Physics* **1993**, *98*, 5648-5652.

(161) Perdew, J. P.; Chevary, J. A.; Vosko, S. H.; Jackson, K. A.; Pederson, M. R.; Singh, D. J.; Fiolhais, C. Atoms, molecules, solids, and surfaces: Applications of the generalized gradient approximation for exchange and correlation. *Physical Review B* **1992**, *46*, 6671-6687.

(162) Gejji, S. P.; Suresh, C. H.; Babu, K.; Gadre, S. R. Ab initio structure and vibrational frequencies of (CF3SO2)(2)N-Li+ ion pairs. *J. Phys. Chem. A* **1999**, *103*, 7474-7480.

(163) Rey, I.; Johansson, P.; Lindgren, J.; Lassegues, J. C.; Grondin, J.; Servant, L. Spectroscopic and theoretical study of (CF3SO2)(2)N- (TFSI-) and (CF3SO2)(2)NH (HTFSI). *J. Phys. Chem. A* **1998**, *102*, 3249-3258.

(164) Bauschlicher, C. W.; Haskins, J. B.; Bucholz, E. W.; Lawson, J. W.; Borodin, O. Structure and Energetics of Li+-(BF4-)(n ') Li+-(FSI-)(n '), and Li+-(TFSI-

)(n): Ab Initio and Polarizable Force Field Approaches. *J. Phys. Chem. B* **2014**, *118*, 10785-10794.

(165) Liu, Z.; Bertolini, S.; Balbuena, P. B.; Mukherjee, P. P. Li2S film formation on lithium anode surface of Li–S batteries. *ACS applied materials & interfaces* **2016**, *8*, 4700-4708.

(166) Kresse, G.; Furthmuller, J. Efficiency of ab-initio total energy calculations for metals and semiconductors using a plane-wave basis set. *Computational Materials Science* **1996**, *6*, 15-50.

(167) Kresse, G.; Hafner, J. Ab initio molecular dynamics for liquid metals. *Physical Review B* **1993**, *47*, 558-561.

(168) Kresse, G.; Hafner, J. Ab initio molecular-dynamics simulation of the liquid-metalamorphous-semiconductor transition in germanium. *Physical Review B* **1994**, *49*, 14251-14269.

(169) Blöchl, P. E. Projector augmented-wave method. *Physical Review B* **1994**, *50*, 17953-17979.

(170) Kresse, G.; Joubert, D. From ultrasoft pseudopotentials to the projector augmented-wave method. *Physical Review B* **1999**, *59*, 1758-1775.

(171) Perdew, J. P.; Burke, K.; Ernzerhof, M. Generalized Gradient Approximation Made Simple. *Physical Review Letters* **1996**, *77*, 3865-3868.

(172) Monkhorst, H. J.; Pack, J. D. Special Points for Brillouin-Zone Integrations. *Phys Rev B* **1976**, *13*, 5188-5192.

(173) MATERIALS STUDIO. *Accelrys Sofware Inc* **2011**.

(174) Tang, W.; Sanville, E.; Henkelman, G. A grid-based Bader analysis algorithm without lattice bias. *Journal of Physics Condensed Matter* **2009**, *21*.

(175) Sanville, E.; Kenny, S. D.; Smith, R.; Henkelman, G. Improved grid-based algorithm for Bader charge allocation. *J. Comput. Chem.* **2007**, *28*, 899-908.

(176) Henkelman, G.; Arnaldsson, A.; Jónsson, H. A fast and robust algorithm for Bader decomposition of charge density. *Computational Materials Science* **2006**, *36*, 354-360.

(177) Grimme, S.; Ehrlich, S.; Goerigk, L. Effect of the damping function in dispersion corrected density functional theory. *Journal of Computational Chemistry* **2011**, *32*, 1456-1465.

(178) Yao, H.; Yan, K.; Li, W.; Zheng, G.; Kong, D.; Seh, Z. W.; Narasimhan, V. K.; Liang, Z.; Cui, Y. Improved lithium-sulfur batteries with a conductive coating on the separator to prevent the accumulation of inactive S-related species at the cathode-separator interface. *Energy & Environmental Science* **2014**, *7*, 3381-3390.

(179) Zhang, K.; Wang, L.; Hu, Z.; Cheng, F.; Chen, J. Ultrasmall Li 2 S nanoparticles anchored in graphene nanosheets for high-energy lithium-ion batteries. *Scientific reports* **2014**, *4*, 6467.

(180) Nagao, M.; Hayashi, A.; Tatsumisago, M. High-capacity Li 2 S–nanocarbon composite electrode for all-solid-state rechargeable lithium batteries. *Journal of Materials Chemistry* **2012**, *22*, 10015-10020.

(181) Liu, Z.; Hubble, D.; Balbuena, P. B.; Mukherjee, P. P. Adsorption of insoluble polysulfides Li 2 S x (x= 1, 2) on Li 2 S surfaces. *Physical Chemistry Chemical Physics* **2015**, *17*, 9032-9039.

(182) Zintl, E.; Harder, A.; Dauth, B. Gitterstruktur der Oxyde, Sulfide, Selenide und Telluride des Lithiums, Natriums und Kaliums. *Zeitschrift für Elektrochemie und angewandte physikalische Chemie* **1934**, *40*, 588-593.

(183) Wang, L.; Zhang, T.; Yang, S.; Cheng, F.; Liang, J.; Chen, J. A quantum-chemical study on the discharge reaction mechanism of lithium-sulfur batteries. *Journal of Energy Chemistry* **2013**, *22*, 72-77.

(184) Vijayakumar, M.; Govind, N.; Walter, E.; Burton, S. D.; Shukla, A.; Devaraj, A.; Xiao, J.; Liu, J.; Wang, C.; Karim, A.; Thevuthasan, S. Molecular structure and stability of dissolved lithium polysulfide species. *Physical Chemistry Chemical Physics* **2014**, *16*, 10923-10932.

(185) Partovi-Azar, P.; Kühne, T. D.; Kaghazchi, P. Evidence for the existence of Li<inf>2</inf>S<inf>2</inf> clusters in lithium-sulfur batteries: Ab initio Raman spectroscopy simulation. *Physical Chemistry Chemical Physics* **2015**, *17*, 22009-22014.

(186) Camacho-Forero, L. E.; Smith, T. W.; Bertolini, S.; Balbuena, P. B. Reactivity at the Lithium-Metal Anode Surface of Lithium-Sulfur Batteries. *J. Phys. Chem. C* **2015**, *119*, 26828-26839.

(187) Yin, Y.-X.; Xin, S.; Guo, Y.-G.; Wan, L.-J. Lithium–Sulfur Batteries: Electrochemistry, Materials, and Prospects. *Angewandte Chemie International Edition* **2013**, *52*, 13186-13200.

(188) Manthiram, A.; Fu, Y.; Su, Y.-S. Challenges and Prospects of Lithium–Sulfur Batteries. *Accounts of Chemical Research* **2013**, *46*, 1125-1134.

(189) Evers, S.; Nazar, L. F. New Approaches for High Energy Density Lithium–Sulfur Battery Cathodes. *Accounts of Chemical Research* **2013**, *46*, 1135-1143.

(190) Xu, W.; Wang, J.; Ding, F.; Chen, X.; Nasybulin, E.; Zhang, Y.; Zhang, J.-G. Lithium metal anodes for rechargeable batteries. *Energy & Environmental Science* **2014**, *7*, 513-537.

(191) Peled, E.; Golodnitsky, D.; Ardel, G. Advanced model for solid electrolyte interphase electrodes in liquid and polymer electrolytes. *Journal of the Electrochemical Society* **1997**, *144*, L208-L210.

(192) Peled, E.; Menkin, S. Review-SEI: Past, Present, and Future. *J. Electrochem. Soc.* **2017**, *164*, A1703-A1719.

(193) Peled, E.; Golodnitsky, D.; Menachem, C.; Bar-Tow, D. An advanced tool for the selection of electrolyte components for rechargeable lithium batteries. *Journal of the Electrochemical Society* **1998**, *145*, 3482-3486.

(194) Verma, P.; Maire, P.; Novák, P. A review of the features and analyses of the solid electrolyte interphase in Li-ion batteries. *Electrochimica Acta* **2010**, *55*, 6332-6341.

(195) Xiong, S.; Xie, K.; Diao, Y.; Hong, X. Characterization of the solid electrolyte interphase on lithium anode for preventing the shuttle mechanism in lithium–sulfur batteries. *Journal of Power Sources* **2014**, *246*, 840-845.

(196) Leung, K.; Budzien, J. L. Ab initio molecular dynamics simulations of the initial stages of solid-electrolyte interphase formation on lithium ion battery graphitic anodes. *Physical Chemistry Chemical Physics* **2010**, *12*, 6583-6586.

(197) Martinez de la Hoz, J. M.; Soto, F. A.; Balbuena, P. B. Effect of the Electrolyte Composition on SEI Reactions at Si Anodes of Li-Ion Batteries. *The Journal of Physical Chemistry C* **2015**, *119*, 7060-7068.

(198) Leung, K.; Rempe, S. B.; Foster, M. E.; Ma, Y.; Martinez del la Hoz, J. M.; Sai, N.; Balbuena, P. B. Modeling Electrochemical Decomposition of Fluoroethylene Carbonate on Silicon Anode Surfaces in Lithium Ion Batteries. *Journal of The Electrochemical Society* **2014**, *161*, A213-A221.

(199) Aurbach, D.; Ein-Eli, Y.; Zaban, A. The Surface Chemistry of Lithium Electrodes in Alkyl Carbonate Solutions. *J. Electrochem. Soc.* **1994**, *141*, L1.

(200) Kim, H. S.; Jeong, T.-G.; Choi, N.-S.; Kim, Y.-T. The cycling performances of lithium–sulfur batteries in TEGDME/DOL containing LiNO3 additive. *Ionics* **2013**, *19*, 1795-1802.

(201) Liang, X.; Wen, Z.; Liu, Y.; Wu, M.; Jin, J.; Zhang, H.; Wu, X. Improved cycling performances of lithium sulfur batteries with LiNO 3-modified electrolyte. *Journal of Power Sources* **2011**, *196*, 9839-9843.

(202) Rosenman, A.; Elazari, R.; Salitra, G.; Markevich, E.; Aurbach, D.; Garsuch, A. The effect of interactions and reduction products of LiNO3, the anti-shuttle agent, in Li-S battery systems. *Journal of The Electrochemical Society* **2015**, *162*, A470-A473.

(203) Li, W.; Yao, H.; Yan, K.; Zheng, G.; Liang, Z.; Chiang, Y.-M.; Cui, Y. The synergetic effect of lithium polysulfide and lithium nitrate to prevent lithium dendrite growth. *Nature communications* **2015**, *6*.

(204) Hong, N. H.; Sakai, J.; Poirot, N.; Brizé, V. Room-temperature ferromagnetism observed in undoped semiconducting and insulating oxide thin films. *Physical Review B* **2006**, *73*, 132404.

(205) Sensato, F. R.; Custódio, R.; Calatayud, M.; Beltrán, A.; Andrés, J.; Sambrano, J. R.; Longo, E. Periodic study on the structural and electronic properties of bulk, oxidized and reduced SnO 2 (110) surfaces and the interaction with O 2. *Surface Science* **2002**, *511*, 408-420.

(206) Beltran, A.; Andres, J.; Sambrano, J.; Longo, E. Density functional theory study on the structural and electronic properties of low index rutile surfaces for TiO2/SnO2/TiO2 and SnO2/TiO2/SnO2 composite systems. *The Journal of Physical Chemistry A* **2008**, *112*, 8943-8952.

(207) Hassan, A.; Irfan, M.; Jiang, Y. Quantum confinement effect and size-dependent photoluminescence in laser ablated ultra-thin GZO films. *Materials Letters* **2018**, *210*, 358-362.

(208) Urban, A.; Seo, D.-H.; Ceder, G. Computational understanding of Li-ion batteries. *Npj Computational Materials* **2016**, *2*, 16002.

(209) Nandasiri, M.; Camacho-Forero, L. E.; Schwarz, A.; Shutthanandan, V.; Thevuthasan, S.; Balbuena, P. B.; Mueller, K.; Vijayakumar, M. In-situ chemical

imaging of solid-electrolyte interphase layer evolution in Li-S batteries. *Chem. Mater.* **2017**, *29*, 4728-4737.

(210) Kohn, W.; Sham, L. J. Self-Consistent Equations Including Exchange and Correlation Effects. *Physical Review* **1965**, *140*, 1133.

(211) Jones, R. O.; Gunnarsson, O. The Density Functional Formalism, Its Applications and Prospects. *Rev Mod Phys* **1989**, *61*, 689-746.

(212) Car, R.; Parrinello, M. Unified Approach for Molecular-Dynamics and Density-Functional Theory. *Phys Rev Lett* **1985**, *55*, 2471-2474.

(213) Payne, M. C.; Teter, M. P.; Allan, D. C.; Arias, T. A.; Joannopoulos, J. D. Iterative minimization techniques for ab initio total-energy calculations: molecular dynamics and conjugate gradients. *Rev Mod Phys* **1992**, *64*, 1045-1097.

(214) Kresse, G.; Hafner, J. Ab initio molecular dynamics for open-shell transition metals. *Physical Review B* **1993**, *48*, 13115.

(215) Kresse, G.; Furthmüller, J. Efficient iterative schemes for ab initio total-energy calculations using a plane-wave basis set. *Physical Review B* **1996**, *54*, 11169-11186.

(216) Nosé, S. A unified formulation of the constant temperature molecular dynamics methods. *The Journal of Chemical Physics* **1984**, *81*, 511-519.

(217) Shuichi, N. Constant Temperature Molecular Dynamics Methods. *Progress of Theoretical Physics Supplement* **1991**, *103*, 1-46.

(218) Bylander, D. M.; Kleinman, L. Energy fluctuations induced by the Nos\'e thermostat. *Physical Review B* **1992**, *46*, 13756-13761.

(219) Lejaeghere, K.; Van Speybroeck, V.; Van Oost, G.; Cottenier, S. Error Estimates for Solid-State Density-Functional Theory Predictions: An Overview by Means of the Ground-State Elemental Crystals. *Critical Reviews in Solid State and Materials Sciences* **2014**, *39*, 1-24.

(220) Gomez-Ballesteros, J. L.; Balbuena, P. B. Reduction of Electrolyte Components on a Coated Si Anode of Lithium-Ion Batteries. *The Journal of Physical Chemistry Letters* **2017**, *8*, 3404-3408.

(221) Heyd, J.; Scuseria, G. E.; Ernzerhof, M. Hybrid functionals based on a screened Coulomb potential. *The Journal of Chemical Physics* **2003**, *118*, 8207-8215.

(222) Heyd, J.; Scuseria, G. E. Efficient hybrid density functional calculations in solids: Assessment of the Heyd–Scuseria–Ernzerhof screened Coulomb hybrid functional. *The Journal of Chemical Physics* **2004**, *121*, 1187-1192.

(223) Heyd, J.; Scuseria, G. E.; Ernzerhof, M. Erratum: “Hybrid functionals based on a screened Coulomb potential” [J. Chem. Phys. 118, 8207 (2003)]. *The Journal of Chemical Physics* **2006**, *124*, 219906.

(224) Krukau, A. V.; Vydrov, O. A.; Izmaylov, A. F.; Scuseria, G. E. Influence of the exchange screening parameter on the performance of screened hybrid functionals. *The Journal of Chemical Physics* **2006**, *125*, 224106.

(225) Farley, T.; Hayes, W.; Hull, S.; Hutchings, M.; Vrtis, M. Investigation of thermally induced Li+ ion disorder in Li2O using neutron diffraction. *Journal of Physics: Condensed Matter* **1991**, *3*, 4761.

(226) KAWADA, I.; ISOBE, M.; OKAMURA, F. P.; WATANABE, H.; OHSUMI, K.; HORIUCHI, H.; ISHII, T. Time-of-flight neutron diffractton study of Li3N at high temperature. *Mineralogical Journal* **1986**, *13*, 28-33.

(227) Ott, H. XI. Die Strukturen von MnO, MnS, AgF, NiS, SnJ4, SrCl2, BaF2; Präzisionsmessungen einiger Alkalihalogenide. *Zeitschrift für Kristallographie-Crystalline Materials* **1926**, *63*, 222-230.

(228) Albright, J. G. The Crystal Structure of Lithium Sulphate. *Zeitschrift für Kristallographie-Crystalline Materials* **1933**, *84*, 150-158.

(229) Lin, B.; Ouyang, X. Energy demand in China: Comparison of characteristics between the US and China in rapid urbanization stage. *Energy Conversion and Management* **2014**, *79*, 128-139.

(230) Bilgen, S. Structure and environmental impact of global energy consumption. *Renewable and Sustainable Energy Reviews* **2014**, *38*, 890-902.

(231) Mohr, S. H.; Wang, J.; Ellem, G.; Ward, J.; Giurco, D. Projection of world fossil fuels by country. *Fuel* **2015**, *141*, 120-135.

(232) Jacobson, M. Z.; Delucchi, M. A. Providing all global energy with wind, water, and solar power, Part I: Technologies, energy resources, quantities and areas of infrastructure, and materials. *Energy Policy* **2011**, *39*, 1154-1169.

(233) McGlade, C.; Ekins, P. The geographical distribution of fossil fuels unused when limiting global warming to 2 [deg]C. *Nature* **2015**, *517*, 187-190.

(234) Victor, D. G. Toward Effective International Cooperation on Climate Change: Numbers, Interests and Institutions. *Global Environmental Politics* **2006**, *6*, 90-103.

(235) Deng, D.; Kim, M. G.; Lee, J. Y.; Cho, J. Green energy storage materials: Nanostructured TiO 2 and Sn-based anodes for lithium-ion batteries. *Energy & Environmental Science* **2009**, *2*, 818-837.

(236) Liu, N.; Lu, Z.; Zhao, J.; McDowell, M. T.; Lee, H.-W.; Zhao, W.; Cui, Y. A pomegranate-inspired nanoscale design for large-volume-change lithium battery anodes. *Nat Nano* **2014**, *9*, 187-192.

(237) Peled, E.: Lithium Stability and Film Formation in Organic and Inorganic Electrolyte for Lithium Battery Systems. In *Lithium Batteries*; Gabano, J. P., Ed.; Academic Press, 1983.

(238) Li, N. W.; Yin, Y. X.; Yang, C. P.; Guo, Y. G. An artificial solid electrolyte interphase layer for stable lithium metal anodes. *Advanced Materials* **2016**, *28*, 1853-1858.

(239) Menkin, S.; Golodnitsky, D.; Peled, E. Artificial solid-electrolyte interphase (SEI) for improved cycleability and safety of lithium–ion cells for EV applications. *Electrochemistry Communications* **2009**, *11*, 1789-1791.

(240) Miao, R.; Yang, J.; Xu, Z.; Wang, J.; Nuli, Y.; Sun, L. A new ether-based electrolyte for dendrite-free lithium-metal based rechargeable batteries. *Scientific reports* **2016**, *6*, 21771.

(241) Qian, J.; Henderson, W. A.; Xu, W.; Bhattacharya, P.; Engelhard, M.; Borodin, O.; Zhang, J.-G. High rate and stable cycling of lithium metal anode. *Nature communications* **2015**, *6*.

(242) Kim, H. S.; Jeong, T.-G.; Choi, N.-S.; Kim, Y.-T. The cycling performances of lithium–sulfur batteries in TEGDME/DOL containing LiNO3 additive. *Ionics* **2013**, *12*, 1795-1802.

(243) Aurbach, D.; Zinigrad, E.; Cohen, Y.; Teller, H. A short review of failure mechanisms of lithium metal and lithiated graphite anodes in liquid electrolyte solutions. *Solid state ionics* **2002**, *148*, 405-416.

(244) Aurbach, D.; Youngman, O.; Gofer, Y.; Meitav, A. The electrochemical behaviour of 1, 3-dioxolane—LiClO 4 solutions—I. Uncontaminated solutions. *Electrochimica acta* **1990**, *35*, 625-638.

(245) Gofer, Y.; Ben-Zion, M.; Aurbach, D. Solutions of LiAsF6 in 1, 3-dioxolane for secondary lithium batteries. *Journal of power sources* **1992**, *39*, 163-178.

(246) vanDuin, A. C. T.; Dasgupta, S.; Lorant, F.; Goddard, W. A. ReaxFF: A reactive force field for hydrocarbons. *J. Phys. Chem. A* **2001**, *105*, 9396-9409.

(247) Mortier, W. J.; Ghosh, S. K.; Shankar, S. Electronegativity-equalization method for the calculation of atomic charges in molecules. *Journal of the American Chemical Society* **1986**, *108*, 4315-4320.

(248) Tersoff, J. Empirical Interatomic Potential for Carbon, with Applications to Amorphous Carbon. *Physical Review Letters* **1988**, *61*, 2879-2882.

(249) Brenner, D. W. Empirical potential for hydrocarbons for use in simulating the chemical vapor deposition of diamond films. *Physical Review B* **1990**, *42*, 9458-9471.

(250) Girifalco, L. A.; Weizer, V. G. Application of the Morse potential function to cubic metals. *Physical Review* **1959**, *114*, 687.

(251) Islam, M. M.; Kolesov, G.; Verstraelen, T.; Kaxiras, E.; van Duin, A. C. T. eReaxFF: A Pseudoclassical Treatment of Explicit Electrons within Reactive Force Field Simulations. *J. Chem. Theory Comput.* **2016**, *12*, 3463-3472.

(252) Islam, M. M.; van Duin, A. C. T. Reductive Decomposition Reactions of Ethylene Carbonate by Explicit Electron Transfer from Lithium: An eReaxFF Molecular Dynamics Study. *The Journal of Physical Chemistry C* **2016**, *120*, 27128-27134.

(253) Yun, K.-S.; Pai, S. J.; Yeo, B. C.; Lee, K.-R.; Kim, S.-J.; Han, S. S. Simulation Protocol for Prediction of a Solid-Electrolyte Interphase on the Silicon-based Anodes of a Lithium-Ion Battery: ReaxFF Reactive Force Field. *The Journal of Physical Chemistry Letters* **2017**, *8*, 2812-2818.

(254) Islam, M. M.; Bryantsev, V. S.; van Duin, A. C. ReaxFF reactive force field simulations on the influence of Teflon on electrolyte decomposition during Li/SWCNT anode discharge in lithium-sulfur batteries. *Journal of The Electrochemical Society* **2014**, *161*, E3009-E3014.

(255) Bedrov, D.; Smith, G. D.; Van Duin, A. C. Reactions of singly-reduced ethylene carbonate in lithium battery electrolytes: a molecular dynamics simulation study using the ReaxFF. *The Journal of Physical Chemistry A* **2012**, *116*, 2978-2985.

(256) Nose, S. A molecular dynamics method for simulations in the canonical ensemble (Reprinted from Molecular Physics, vol 52, pg 255, 1984). *Mol. Phys.* **2002**, *100*, 191-198.

(257) Plimpton, S. Fast parallel algorithms for short-range molecular dynamics. *J. Comput. Phys.* **1995**, *117*, 1-19.

(258) Shkrob, I. A.; Zhu, Y.; Marin, T. W.; Abraham, D. Reduction of carbonate electrolytes and the formation of solid-electrolyte interface (SEI) in Lithium-ion batteries. 1. spectroscopic observations of radical intermediates generated in one-electron reduction of carbonates. *The Journal of Physical Chemistry C* **2013**, *117*, 19255-19269.

(259) Soto, F. A.; Ma, Y.; Martinez de la Hoz, J. M.; Seminario, J. M.; Balbuena, P. B. Formation and growth mechanisms of solid-electrolyte interphase layers in rechargeable batteries. *Chemistry of Materials* **2015**, *27*, 7990-8000.

(260) Burkhardt, S. E. Impact of Chemical Follow-up Reactions for Lithium Ion Electrolytes: Generation of Nucleophilic Species, Solid Electrolyte Interphase, and Gas Formation. *Journal of The Electrochemical Society* **2017**, *164*, A684-A690.

(261) Peled, E.; Golodnitsky, D.; Menachem, C.; Bar-Tow, D. An advanced tool for the selection of electrolyte components for rechargeable lithium batteries. *Journal of the electrochemical Society* **1998**, *145*, 3482-3486.

(262) Teng, X.; Zhan, C.; Bai, Y.; Ma, L.; Liu, Q.; Wu, C.; Wu, F.; Yang, Y.; Lu, J.; Amine, K. In situ analysis of gas generation in lithium-ion batteries with different carbonate-based electrolytes. *ACS applied materials & interfaces* **2015**, *7*, 22751-22755.

(263) Li, T.; Balbuena, P. B. Theoretical studies of lithium perchlorate in ethylene carbonate, propylene carbonate, and their mixtures. *Journal of the Electrochemical society* **1999**, *146*, 3613-3622.

(264) Umebayashi, Y.; Mitsugi, T.; Fukuda, S.; Fujimori, T.; Fujii, K.; Kanzaki, R.; Takeuchi, M.; Ishiguro, S.-I. Lithium ion solvation in room-temperature ionic liquids involving bis (trifluoromethanesulfonyl) imide anion studied by Raman spectroscopy and DFT calculations. *The Journal of Physical Chemistry B* **2007**, *111*, 13028-13032.

(265) Borodin, O.; Smith, G. D. LiTFSI structure and transport in ethylene carbonate from molecular dynamics simulations. *The Journal of Physical Chemistry B* **2006**, *110*, 4971-4977.

(266) Morita, M.; Asai, Y.; Yoshimoto, N.; Ishikawa, M. A Raman spectroscopic study of organic electrolyte solutions based on binary solvent systems of ethylene carbonate with low viscosity solvents which dissolve different lithium salts. *Journal of the Chemical Society, Faraday Transactions* **1998**, *94*, 3451-3456.

(267) Jeong, S.-K.; Inaba, M.; Iriyama, Y.; Abe, T.; Ogumi, Z. Surface film formation on a graphite negative electrode in lithium-ion batteries: AFM study on the effects of co-solvents in ethylene carbonate-based solutions. *Electrochimica acta* **2002**, *47*, 1975-1982.

(268) Martin, F.; Zipse, H. Charge distribution in the water molecule—a comparison of methods. *Journal of computational chemistry* **2005**, *26*, 97-105.

(269) Assowe, O.; Politano, O.; Vignal, V.; Arnoux, P.; Diawara, B.; Verners, O.; Van Duin, A. Reactive molecular dynamics of the initial oxidation stages of Ni (111)

in pure water: Effect of an applied electric field. *The Journal of Physical Chemistry A* **2012**, *116*, 11796-11805.

(270) Peled, E.; Menkin, S. SEI: Past, Present and Future. *Journal of The Electrochemical Society* **2017**, *164*, A1703-A1719.

(271) Bertolini, S.; Balbuena, P. B. Effect of solid electrolyte interphase on the reactivity of polysulfide over lithium-metal anode. *Electrochimica Acta* **2017**, *258*, 1320-1328.

(272) Wang, Y.; Nakamura, S.; Tasaki, K.; Balbuena, P. B. Theoretical studies to understand surface chemistry on carbon anodes for lithium-ion batteries: How does vinylene carbonate play its role as an electrolyte additive? *J. Am. Chem. Soc.* **2002**, *124*, 4408-4421.

(273) Wang, Y.; Nakamura, S.; Ue, M.; Balbuena, P. B. Theoretical studies to understand surface chemistry on carbon anodes for lithium-ion batteries: Reduction mechanisms of ethylene carbonate. *J. Am. Chem. Soc.* **2001**, *123*, 11708-11718.

(274) Islam, M. M.; Kolesov, G.; Verstraelen, T.; Kaxiras, E.; van Duin, A. C. eReaxFF: A pseudoclassical treatment of explicit electrons within reactive force field simulations. *Journal of chemical theory and computation* **2016**, *12*, 3463-3472.

(275) Islam, M. M.; van Duin, A. C. Reductive Decomposition Reactions of Ethylene Carbonate by Explicit Electron Transfer from Lithium: An eReaxFF Molecular Dynamics Study. *The Journal of Physical Chemistry C* **2016**, *120*, 27128-27134.

(276) Castro-Marcano, F.; Kamat, A. M.; Russo, M. F.; van Duin, A. C.; Mathews, J. P. Combustion of an Illinois No. 6 coal char simulated using an atomistic

char representation and the ReaxFF reactive force field. *Combustion and Flame* **2012**, *159*, 1272-1285.

(277) Bertolini, S.; Balbuena, P. B. Buildup of Solid Electrolyte Interphase on Lithium-Metal Anode: Reactive Molecular Dynamics Study. *The Journal of Physical Chemistry C* **2018**.

(278) Kresse, G.; Furthmuller, J. Efficient iterative schemes for ab initio total-energy calculations using a plane-wave basis set. *Phys Rev B* **1996**, *54*, 11169-11186.

(279) Frisch, M.; Trucks, G.; Schlegel, H.; Scuseria, G.; Robb, M.; Cheeseman, J.; Scalmani, G.; Barone, V.; Mennucci, B.; Petersson, G.: Gaussian 09, revision D. 01. Gaussian, Inc., Wallingford CT, 2009.

(280) Becke, A. D. Density-functional thermochemistry. III. The role of exact exchange. *The Journal of chemical physics* **1993**, *98*, 5648-5652.

(281) Perdew, J. P.; Chevary, J. A.; Vosko, S. H.; Jackson, K. A.; Pederson, M. R.; Singh, D. J.; Fiolhais, C. Atoms, molecules, solids, and surfaces: Applications of the generalized gradient approximation for exchange and correlation. *Physical Review B* **1992**, *46*, 6671.

(282) Tomasi, J.; Mennucci, B.; Cammi, R. Quantum Mechanical Continuum Solvation Models. *Chemical Reviews* **2005**, *105*, 2999-3094.

(283) Casewit, C.; Colwell, K.; Rappe, A. Application of a universal force field to organic molecules. *Journal of the American chemical society* **1992**, *114*, 10035-10046.

(284) Rappe, A.; Colwell, K.; Casewit, C. Application of a universal force field to metal complexes. *Inorganic Chemistry* **1993**, *32*, 3438-3450.

(285) Deringer, V. L.; Tchougréeff, A. L.; Dronskowski, R. Crystal orbital Hamilton population (COHP) analysis as projected from plane-wave basis sets. *The Journal of Physical Chemistry A* **2011**, *115*, 5461-5466.

(286) Maintz, S.; Deringer, V. L.; Tchougréeff, A. L.; Dronskowski, R. LOBSTER: A tool to extract chemical bonding from plane-wave based DFT. *Journal of computational chemistry* **2016**, *37*, 1030-1035.

(287) Leung, K.; Rempe, S. B.; Foster, M. E.; Ma, Y.; del la Hoz, J. M. M.; Sai, N.; Balbuena, P. B. Modeling electrochemical decomposition of fluoroethylene carbonate on silicon anode surfaces in lithium ion batteries. *Journal of The Electrochemical Society* **2014**, *161*, A213-A221.

(288) Okuno, Y.; Ushirogata, K.; Sodeyama, K.; Tateyama, Y. Decomposition of the fluoroethylene carbonate additive and the glue effect of lithium fluoride products for the solid electrolyte interphase: an ab initio study. *Physical Chemistry Chemical Physics* **2016**, *18*, 8643-8653.

(289) Tasaki, K. Solvent decompositions and physical properties of decomposition compounds in Li-ion battery electrolytes studied by DFT calculations and molecular dynamics simulations. *The Journal of Physical Chemistry B* **2005**, *109*, 2920-2933.

(290) Xing, L.; Li, W.; Wang, C.; Gu, F.; Xu, M.; Tan, C.; Yi, J. Theoretical investigations on oxidative stability of solvents and oxidative decomposition mechanism

of ethylene carbonate for lithium ion battery use. *The Journal of Physical Chemistry B* **2009**, *113*, 16596-16602.

(291) Aurbach, D.; Gofer, Y.; Ben-Zion, M.; Aped, P. The behaviour of lithium electrodes in propylene and ethylene carbonate: Te major factors that influence Li cycling efficiency. *Journal of Electroanalytical Chemistry* **1992**, *339*, 451-471.

(292) Yu, J.; Balbuena, P. B.; Budzien, J.; Leung, K. Hybrid DFT functional-based static and molecular dynamics studies of excess electron in liquid ethylene carbonate. *Journal of The Electrochemical Society* **2011**, *158*, A400-A410.

(293) Wang, Y.; Nakamura, S.; Tasaki, K.; Balbuena, P. B. Theoretical studies to understand surface chemistry on carbon anodes for lithium-ion batteries: how does vinylene carbonate play its role as an electrolyte additive? *Journal of the American Chemical Society* **2002**, *124*, 4408-4421.

(294) Wang, Y.; Balbuena, P. B. Theoretical studies on cosolvation of Li ion and solvent reductive decomposition in binary mixtures of aliphatic carbonates. *International journal of quantum chemistry* **2005**, *102*, 724-733.

(295) Wang, Y.; Balbuena, P. B. Theoretical insights into the reductive decompositions of propylene carbonate and vinylene carbonate: density functional theory studies. *The Journal of Physical Chemistry B* **2002**, *106*, 4486-4495.

(296) de la Hoz, J. M. M.; Balbuena, P. B. Reduction mechanisms of additives on Si anodes of Li-ion batteries. *Physical Chemistry Chemical Physics* **2014**, *16*, 17091-17098.

(297) Xing, L.; Borodin, O. Oxidation induced decomposition of ethylene carbonate from DFT calculations–importance of explicitly treating surrounding solvent. *Physical Chemistry Chemical Physics* **2012**, *14*, 12838-12843.

(298) Han, Y.-K.; Lee, S. U.; Ok, J.-H.; Cho, J.-J.; Kim, H.-J. Theoretical studies of the solvent decomposition by lithium atoms in lithium-ion battery electrolyte. *Chemical physics letters* **2002**, *360*, 359-366.

(299) Ushirogata, K.; Sodeyama, K.; Okuno, Y.; Tateyama, Y. Additive effect on reductive decomposition and binding of carbonate-based solvent toward solid electrolyte interphase formation in lithium-ion battery. *Journal of the American Chemical Society* **2013**, *135*, 11967-11974.

(300) Chen, X.; Hou, T.-Z.; Li, B.; Yan, C.; Zhu, L.; Guan, C.; Cheng, X.-B.; Peng, H.-J.; Huang, J.-Q.; Zhang, Q. Towards stable lithium-sulfur batteries: Mechanistic insights into electrolyte decomposition on lithium metal anode. *Energy Storage Materials* **2017**.

(301) Camacho-Forero, L. E.; Balbuena, P. B. Elucidating electrolyte decomposition under electron-rich environments at the lithium-metal anode. *Physical Chemistry Chemical Physics* **2017**, *19*, 30861-30873.

(302) Leung, K.; Soto, F.; Hankins, K.; Balbuena, P. B.; Harrison, K. L. Stability of solid electrolyte interphase components on lithium metal and reactive anode material surfaces. *The Journal of Physical Chemistry C* **2016**, *120*, 6302-6313.

(303) Camacho-Forero, L. E.; Smith, T. W.; Balbuena, P. B. Effects of high and low salt concentration in electrolytes at lithium–metal anode surfaces. *The Journal of Physical Chemistry C* **2016**, *121*, 182-194.

(304) Nandasiri, M. I.; Camacho-Forero, L. E.; Schwarz, A. M.; Shutthanandan, V.; Thevuthasan, S.; Balbuena, P. B.; Mueller, K. T.; Murugesan, V. In Situ Chemical Imaging of Solid-Electrolyte Interphase Layer Evolution in Li–S Batteries. *Chemistry of Materials* **2017**, *29*, 4728-4737.

(305) Schmidt, M.; Heider, U.; Kuehner, A.; Oesten, R.; Jungnitz, M.; Ignat'ev, N.; Sartori, P. Lithium fluoroalkylphosphates: a new class of conducting salts for electrolytes for high energy lithium-ion batteries. *Journal of power sources* **2001**, *97*, 557-560.

(306) Han, H.-B.; Zhou, S.-S.; Zhang, D.-J.; Feng, S.-W.; Li, L.-F.; Liu, K.; Feng, W.-F.; Nie, J.; Li, H.; Huang, X.-J. Lithium bis (fluorosulfonyl) imide (LiFSI) as conducting salt for nonaqueous liquid electrolytes for lithium-ion batteries: Physicochemical and electrochemical properties. *Journal of Power Sources* **2011**, *196*, 3623-3632.

(307) Aravindan, V.; Gnanaraj, J.; Madhavi, S.; Liu, H. K. Lithium-Ion Conducting Electrolyte Salts for Lithium Batteries. *Chemistry-A European Journal* **2011**, *17*, 14326-14346.

(308) Ensling, D.; Stjerndahl, M.; Nytén, A.; Gustafsson, T.; Thomas, J. O. A comparative XPS surface study of Li 2 FeSiO 4/C cycled with LiTFSI-and LiPF 6-based electrolytes. *Journal of Materials Chemistry* **2009**, *19*, 82-88.

(309) Gu, S.; Wen, Z.; Qian, R.; Jin, J.; Wang, Q.; Wu, M.; Zhuo, S. Carbon Disulfide Cosolvent Electrolytes for High-Performance Lithium Sulfur Batteries. *ACS applied materials & interfaces* **2016**, *8*, 34379-34386.

(310) Ein-Eli, Y. Dithiocarbonic anhydride (CS 2)—a new additive in Li-ion battery electrolytes. *Journal of Electroanalytical Chemistry* **2002**, *531*, 95-99.

(311) Tsukuda, T.; Hirose, T.; Nagata, T. Negative-ion photoelectron spectroscopy of (CS2) n−: coexistence of electronic isomers. *Chemical physics letters* **1997**, *279*, 179-184.

(312) Sülzle, D.; Schwarz, H. CCS and S (C4) S: The laboratory generation of interstellar molecules and their radical cations. *European Journal of Inorganic Chemistry* **1989**, *122*, 1803-1805.

(313) Moltzen, E. K.; Klabunde, K. J.; Senning, A. Carbon monosulfide: A review. *Chemical reviews* **1988**, *88*, 391-406.

(314) Tanaka, K.; Koike, T.; Kobashi, M.; Nishino, H.; Yamabe, T. Electronic structures of poly (carbon disulfide) and poly (carbon diselenide). *Synthetic metals* **1991**, *39*, 281-289.

(315) Hiraoka, K.; Fujimaki, S.; Aruga, K.; Yamabe, S. Frontier-Controlled Structures of the Gas-Phase A.+-.(CS2) n Clusters, A.+-.= S2+, CS2+, S2-, and CS2. *The Journal of Physical Chemistry* **1994**, *98*, 1802-1809.

(316) Tsukamoto, J.; Takahashi, A. Polymeric product of carbon disulfide and its electrical properties. *Japanese journal of applied physics* **1986**, *25*, L338.

(317) Vollmer, J. M.; Curtiss, L. A.; Vissers, D. R.; Amine, K. Reduction Mechanisms of Ethylene, Propylene, and Vinylethylene Carbonates A Quantum Chemical Study. *Journal of The Electrochemical Society* **2004**, *151*, A178-A183.

(318) Howlett, P. C.; Izgorodina, E. I.; Forsyth, M.; MacFarlane, D. R. Electrochemistry at negative potentials in bis (trifluoromethanesulfonyl) amide ionic liquids. *Zeitschrift für Physikalische Chemie* **2006**, *220*, 1483-1498.

(319) Chen, X.; Hou, T.-Z.; Li, B.; Yan, C.; Zhu, L.; Guan, C.; Cheng, X.-B.; Peng, H.-J.; Huang, J.-Q.; Zhang, Q. Towards stable lithium-sulfur batteries: Mechanistic insights into electrolyte decomposition on lithium metal anode. *Energy Storage Materials* **2017**, *8*, 194-201.

(320) Cheng, X.-B.; Zhang, R.; Zhao, C.-Z.; Wei, F.; Zhang, J.-G.; Zhang, Q. A Review of Solid Electrolyte Interphases on Lithium Metal Anode. *Advanced Science* **2015**, n/a-n/a.

APPENDIX A

SUPPORTING INFORMATIONS FOR SECTION 4 AND 5

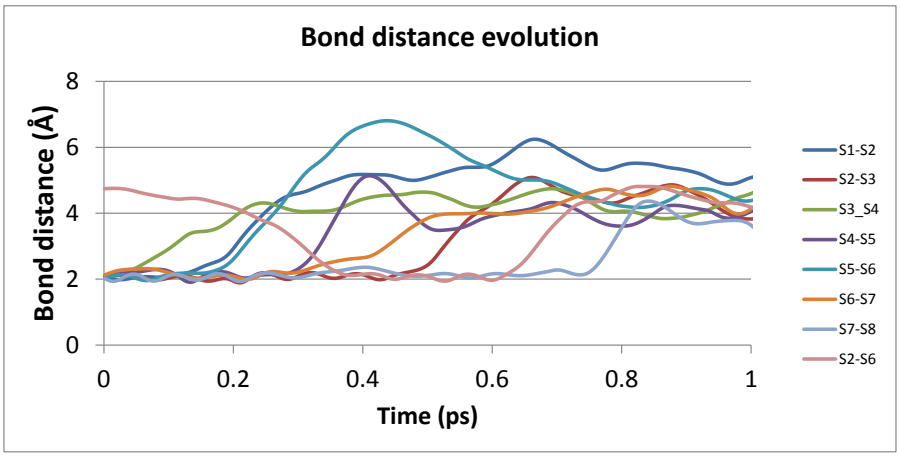

Figure A.1: Time evolution of S-S bond distance on one PS's molecule at the slab surface. The reconstruction of a chain occurs around 0.38 ps, the mechanism S3 + S2 = S4 + S represents the modification of chain size.

In the thin film calculations, the schematic configurations of the cells are shown on Figure S1. The cells have a square base of 10.33Å, and in the Z direction, the cells are separated by the lithium metal phase, the SEI phase, the electrolyte and a helium monolayer. The lithium metal anode has 3 layers frozen at the bottom of the cell and 3 free layers at the top, interfacing with the SEI layer. The SEI layers are obtained by cleaving over the (100) and (110) planes of Li_2O, Li_3N, LiF and Li_2SO_4. The electrolyte is composed by 1M of polysulfide (PS) Li_2S_8 and Lithium Bis(trifluoromethanesulfonyl)imide (LiTFSI) in 1,3 dioxolane (DOL) as the solvent having a density of 1.06 g/cm³. The PS is placed in the electrolyte closer of the SEI surface; the PS is set at the same distance from the SEI surface in every cell. The PS has a ring structure, formed by the sulfur-sulfur bonds and closed by two lithium atoms. As

can be observed in **Figure A.2**, the PS ring is placed against the SEI surface and the LiTFSI is placed closer to the helium monolayer separating simulation cells. The helium monolayer is used to mitigate the reaction between the electrolytes with the bottom side of the anode.

The charge analyses of the SEI layer (**Figure A.3**) indicates that the Li charge in the SEI layer oscillates in opposite sense that the lithium charge on metal, but is Li from the metal phase that releases electrons for the PS decomposition. In the **Figure A.4**, the variation of the charge per Li atom can be neglected for the Li from the SEI layers (right vertical axis), while the charge increases in the metal phase (left vertical axis). In Figure S3, it is possible to observe that the SEI affects the evolution of the charge in the anode phase. When the SEI is composed by Li_2O, the increase of charge per lithium atom in the metal phase is slower than in LiF and in Li_2SO_4. The charge per lithium atom starts almost zero for Li_2O and LiF, while for Li_2SO_4 it starts already with a positive charge. After 32ps, the charge per lithium metal in the presence of LiF and Li_2SO_4 is similar, indicating that during this period, the Li in the metal phase in presence of LiF comparatively has a higher increase in the value of charge per Li atom.

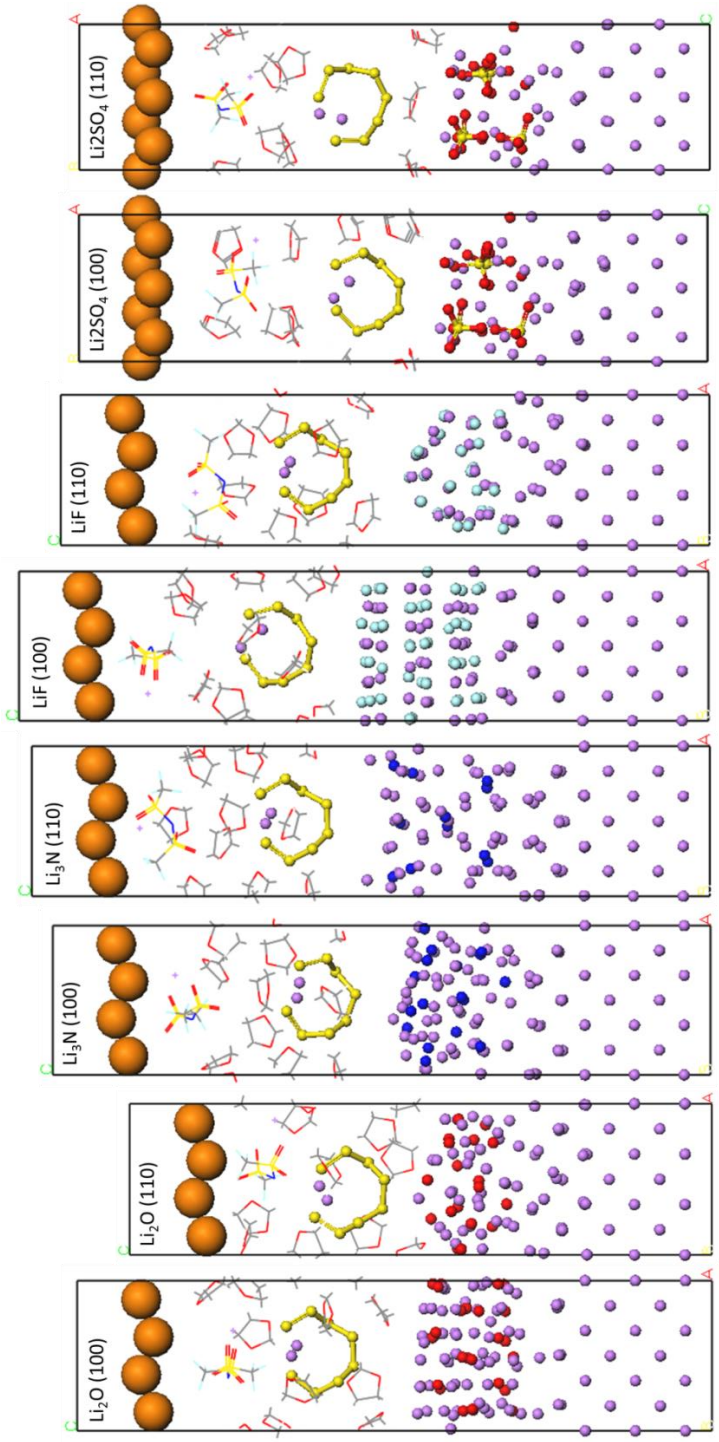

Figure A.2: Schematic configuration of assemblies used to simulate the reactivity of polysulfide in thin films. Lithium is represented by the purple color, oxygen by red, carbon by gray, sulfur by yellow, nitrogen by blue, fluorine by cyan, hydrogen by white and helium by orange.

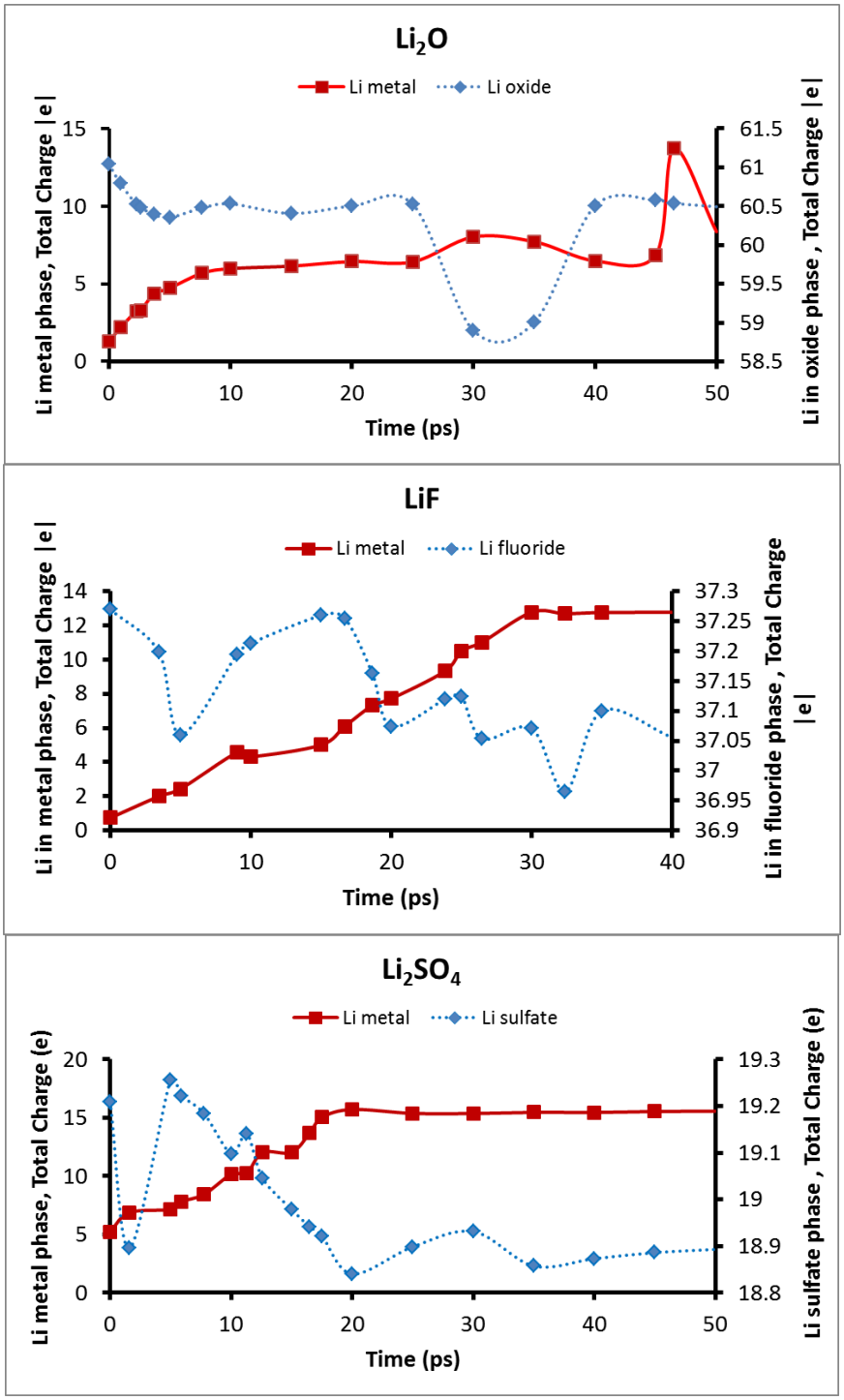

Figure A.3: Total charge of Li atoms in the metal phase (left vertical axis) and in the SEI (right vertical axis) in the thich layer simulations. The SEI is composed by oxide, fluoride and sulfate respectively.

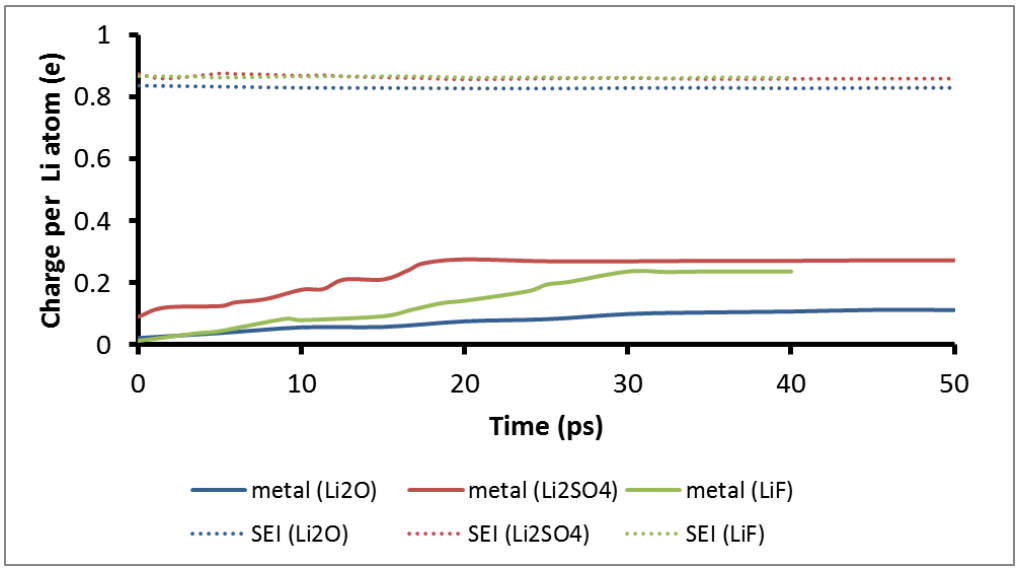

Figure A.4: Charge evolution per Li atom in the metal phase and in the SEI for thick layer simulation, where the SEI is composed by Li_2O, LiF and Li_2SO_4.

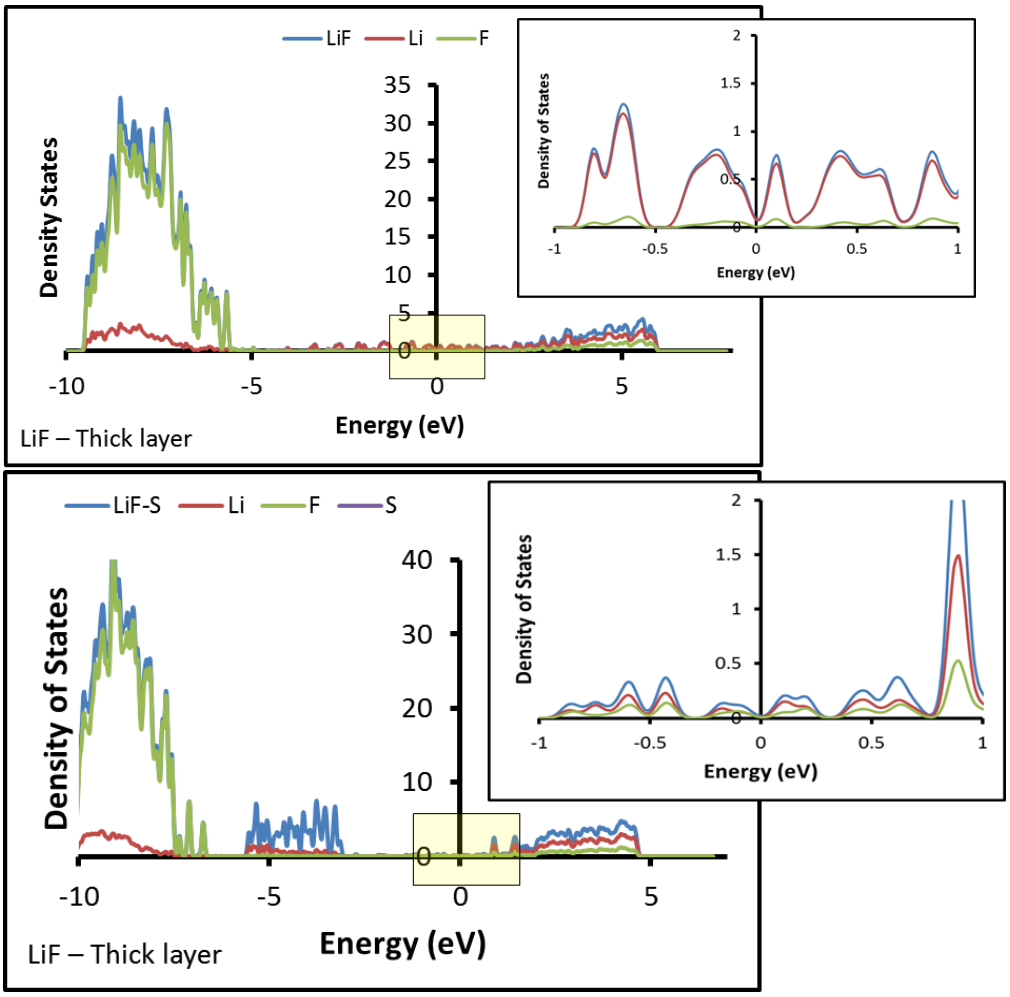

Figure A.5: Density of States of the SEI composed by LiF using hybrid functional HSE06. The graphs show intermediate states between the main valence and conduction band. Fermi level energy is set at 0eV. The DOS correspond to the 10 nm SEI layer at the initial and last calculated frame in each simulation.

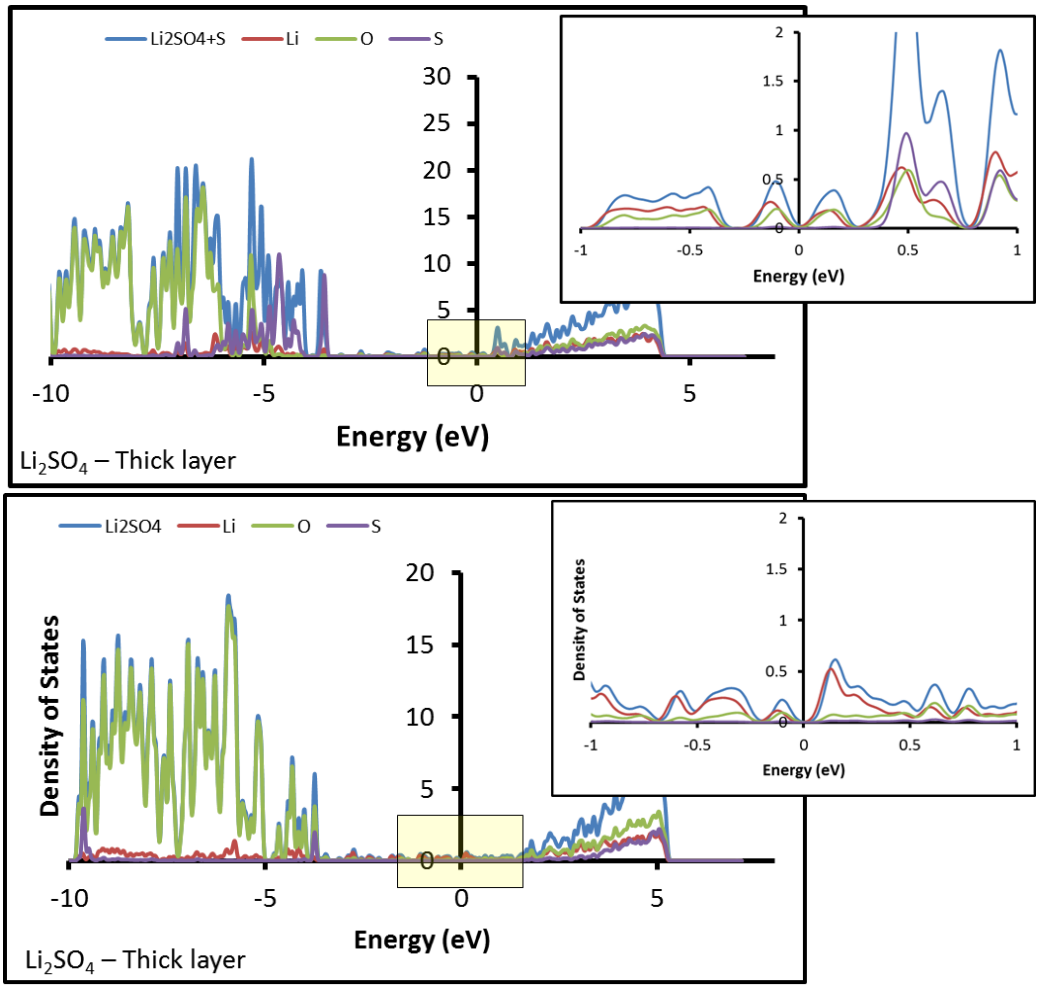

Figure A.6: Density of States of the SEI composed by Li_2SO_4 using hybrid functional HSE06. The graphs show intermediate states between the main valence and conduction band. Fermi level energy is set at 0eV. The DOS correspond to the 10 nm SEI layer at the beginning and the last calculated frame in each simulation.

APPENDIX B

SUPPORTING INFORMATIONS FOR SECTION 6

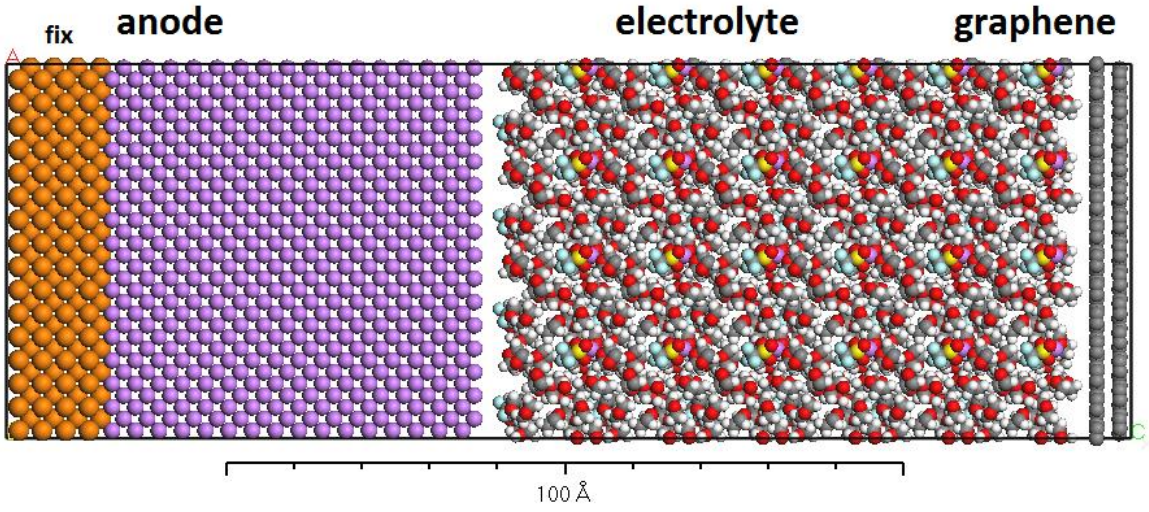

Figure B.1: Initial configuration of simulation cell. The Li-metal surface is simulated by adding an extra layer with atoms fixed in their positions to represent the bulk material. The reactions take place on top of the anode surface and the graphene layer separates and forbid the reactions of the bottom anode surface with the electrolyte. Color code: frozen lithium atoms: orange, Li: purple, O: red, C: gray, H: white, F: cyan and S: yellow.

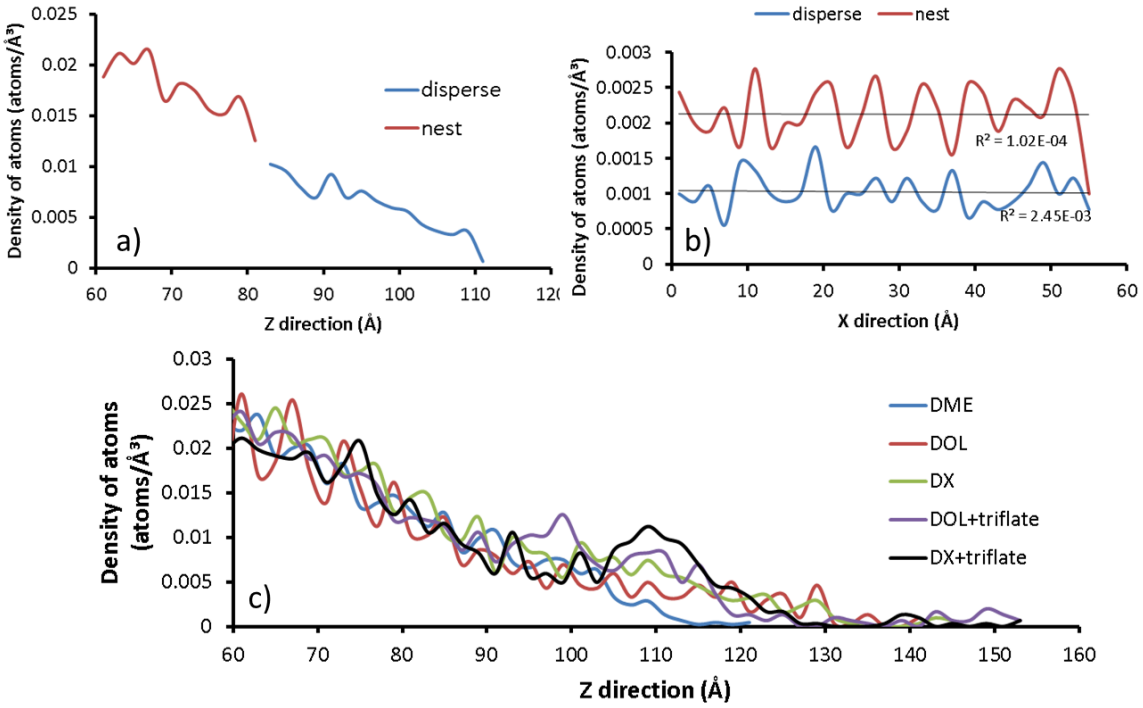

Figure B.2: Density profile of (a) Li atoms in Z (perpendicular to the Li metal surface) and (b) X directions for the nest and disperse phases in DX with Li-Triflate. (c) Z-density profile of Li atoms in different electrolytes at 2ns. The profile of Density of Li atoms starts from the dense phase (60Å) and it goes up to the location of the farther lithium on the disperse phase. The interphase between the disperse phase localized between 80 Å and 90 Å.

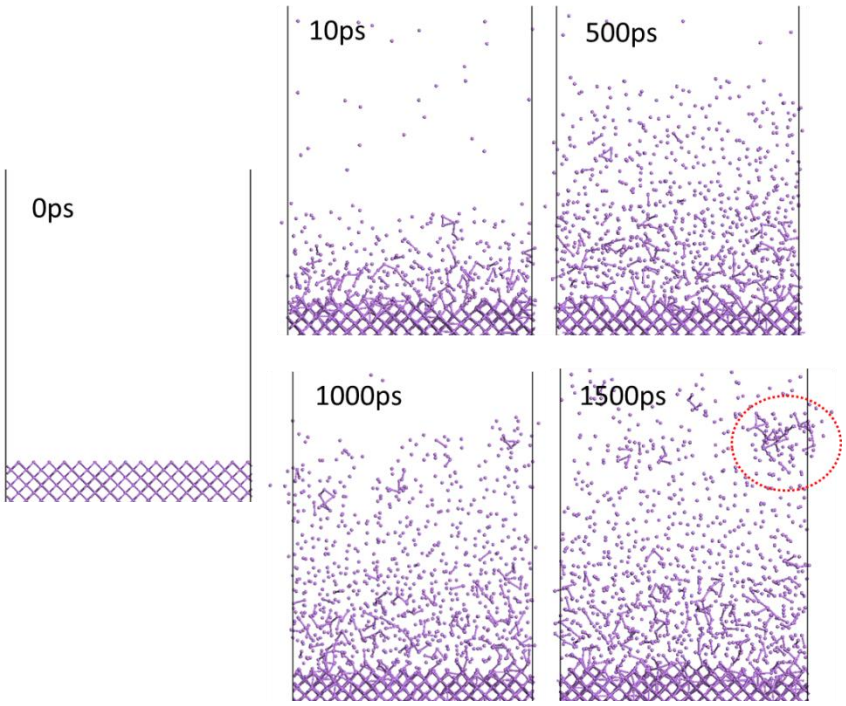

Figure B.3: Distribution of Li atoms over the Li-metal anode surface over time and formation of Li clusters.

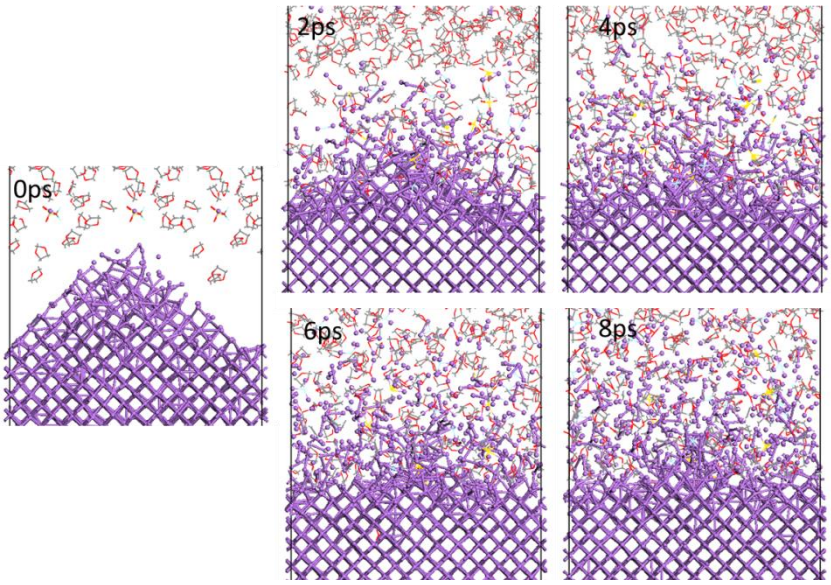

Figure B.4: Nano tip dissolution in the electrolyte phase

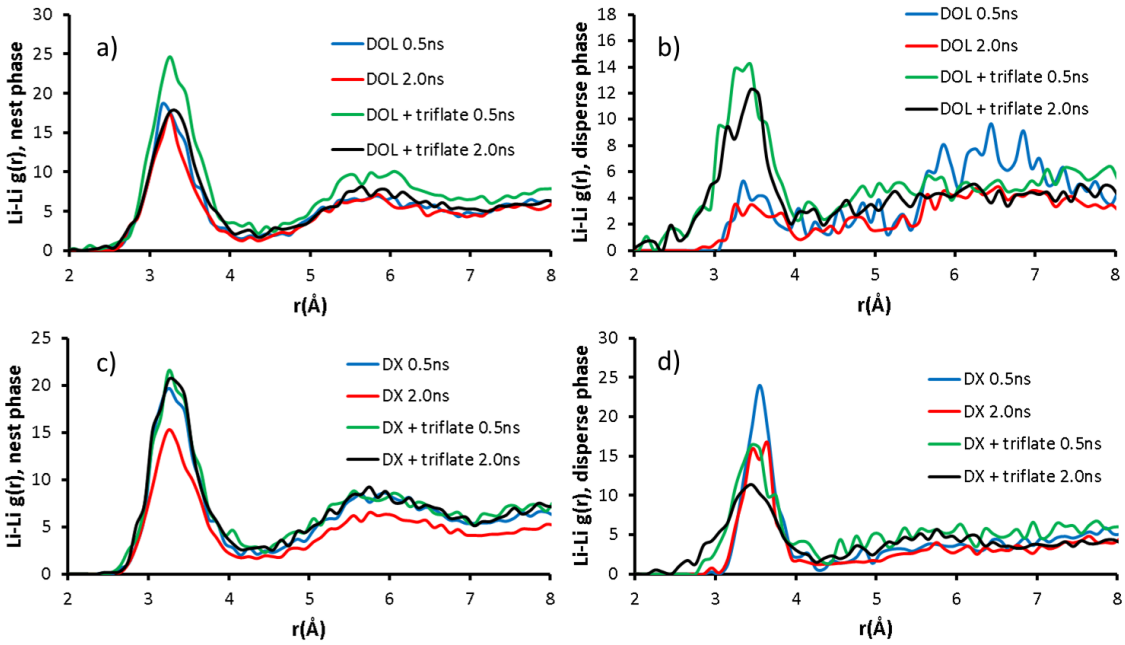

Figure B.5: Li-Li Radial Pair Distribution Functions time evolution of Li structure in different electrolytes. a) nest phase in DOL and DOL:Litriflate, during 0.5ns and 2.0ns. b) disperse phase in DOL and DOL:Litriflate, during 0.5ns and 2.0ns. c) nest phase in DX and DX:Litriflate, during 0.5ns and 2.0ns. b) disperse phase in DX and DX:Litriflate, during 0.5ns and 2.0ns

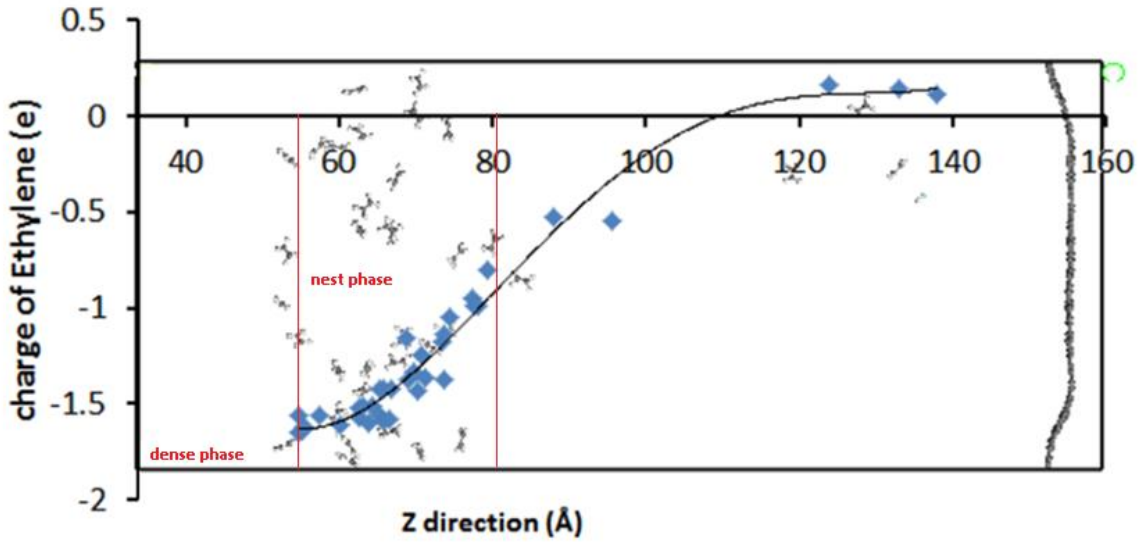

Figure B.6: Variation of the total charge on the ethylene molecule in the z direction of the cell using ReaxFF to calculate the charges.

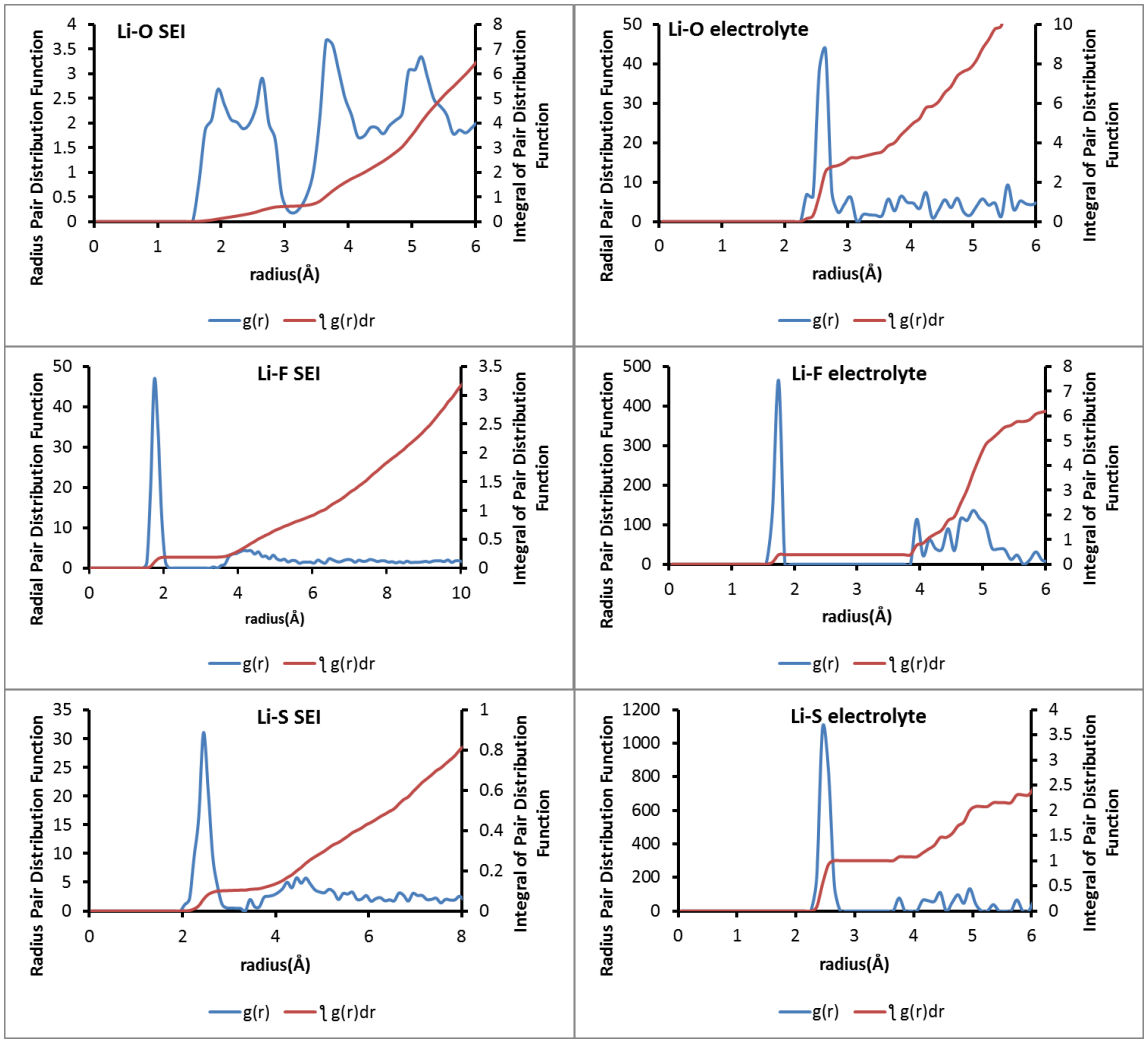

Figure B.7: Li-X Radial Pair Distribution Function (RPDF) and integral of RPDF (X = oxygen, fluorine, or sulfur).

As it is well known, the electronic charges on the atoms or atomic sites are not direct observables, and the fractional numbers are just artifact of the computational method that assigns a number based on the distribution of electronic density. Thus, the fractional charge (shown in **Figure B.6**, **B.8** and **Table A.1**) does not correspond to a physical quantity, and it only provides an estimate of the oxidation state of the particular atom or atomic site.

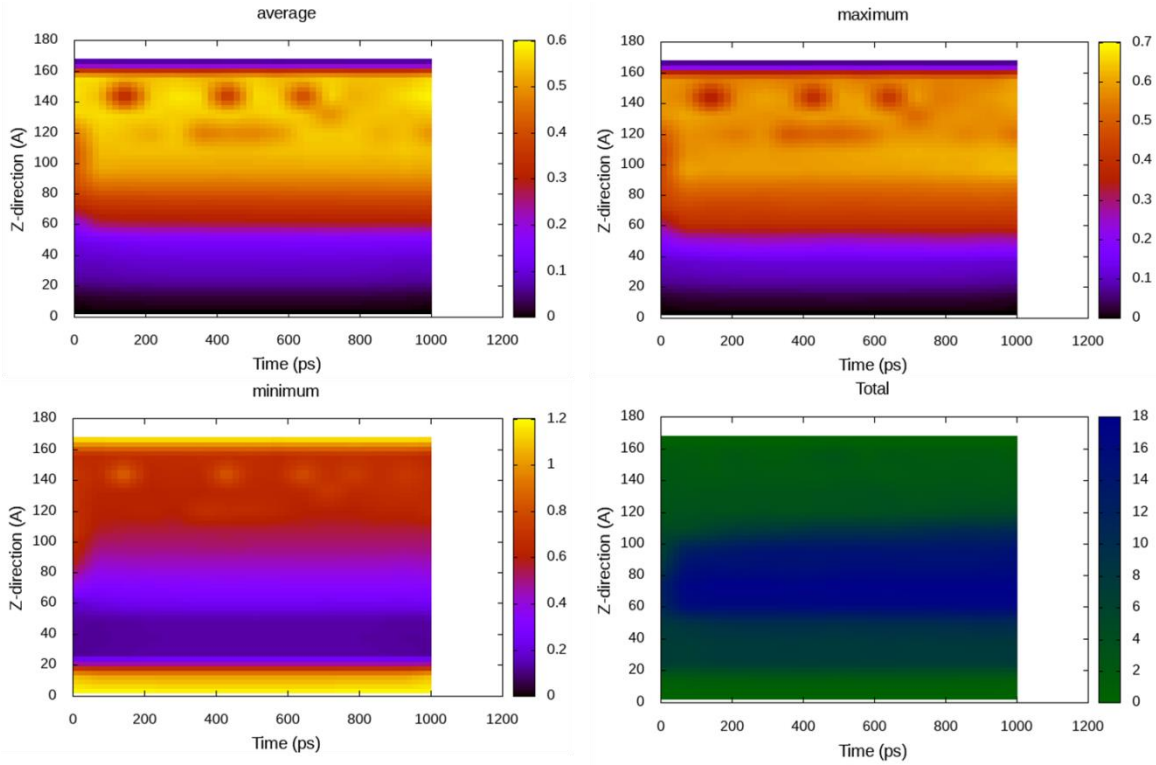

Figure B.8 Time evolution of charge distribution of Li through the z direction, using 1M Li-triflate in DOL as electrolyte.The charge are plot from blocks of 2Å in the Z direction. The lithium atoms of each block are counted to plot the average, maximum, minimum and total charge of the block.

Table B.1: Charge analyses by ReaxFF and Bader calculations of the cluster found at 2ns immersed on electrolyte composed by DX and triflate. Δ is the average difference between ReaxFF and Bader charges, minΔ and maxΔ are minimum and maximum differences respectively.

	ReaxFF	Bader charges	Δ	minΔ	maxΔ
Li	0.64	0.85	0.21	0.02	0.45
O	-0.53	-1.18	0.65	0.36	0.90
C	-0.13	0.00	0.13	0.08	1.08
F	-0.72	-0.84	0.12	0.00	0.26
S	-0.18	0.57	0.75	0.13	2.54

APPENDIX C

SUPPORTING INFORMATIONS FOR SECTION 7

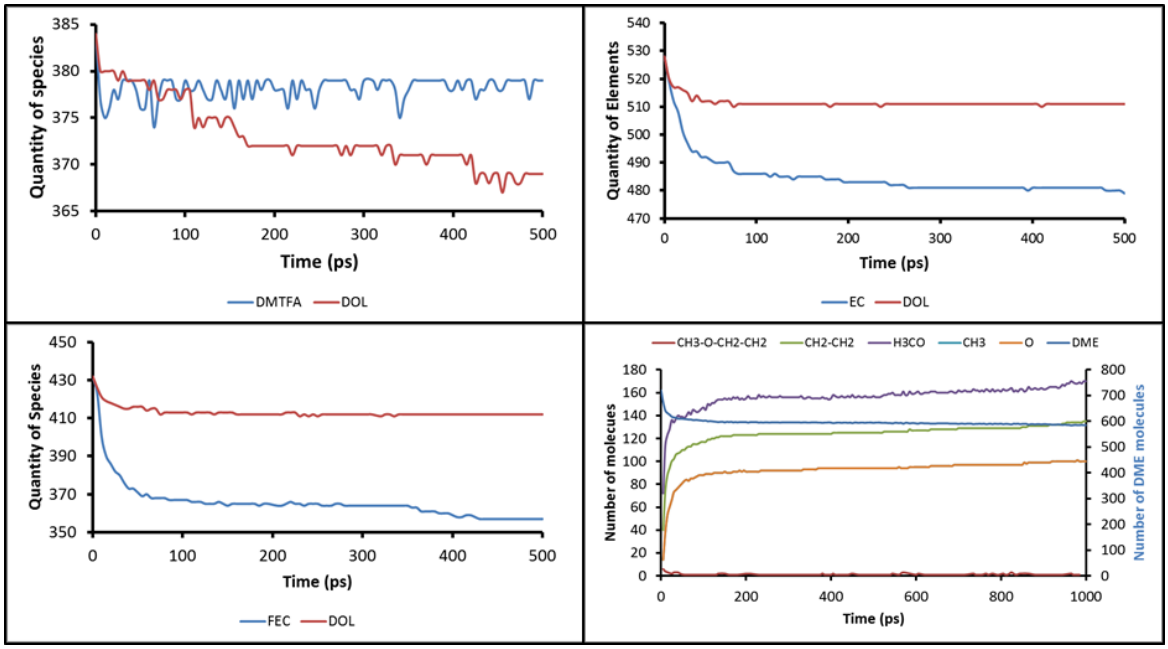

Figure C.1: Evolution of species quantity over time in presence of DOL:DMTFA, DOL:EC, DOL:FEC and DME

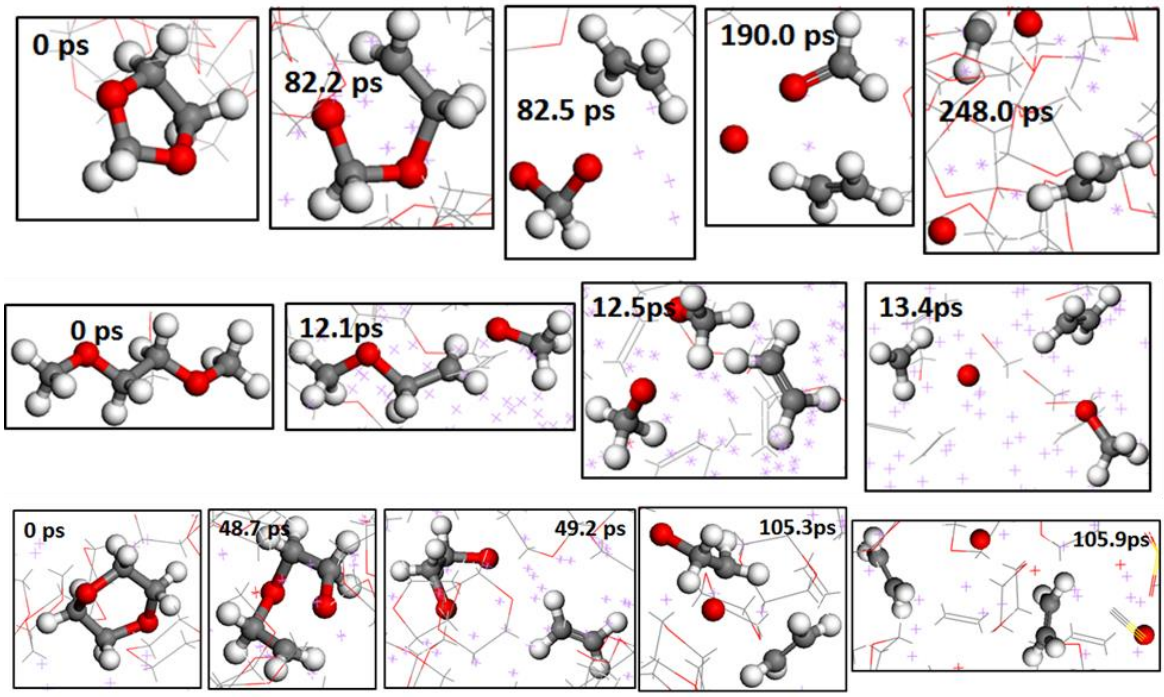

Figure C.2: Mechanism of decomposition of DOL, DME and DX in ReaxFF. Carbon is colored by gray, fluorine by cyan, hydrogen by white, oxygen by red, sulfur by yellow and lithium is by purple dots.

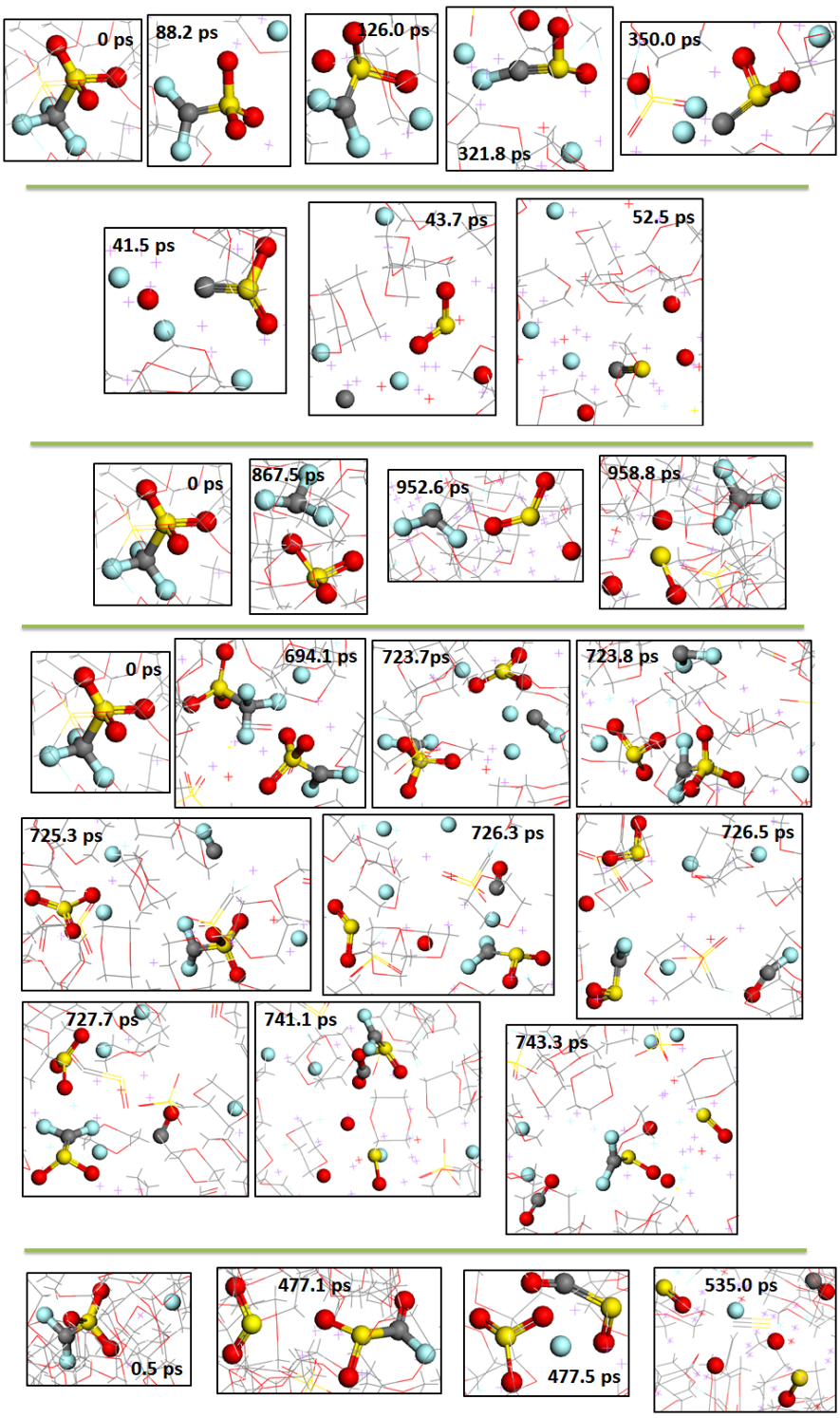

Figure C.3: Reactions between triflate fragments. Carbon is colored by gray, fluorine by cyan, hydrogen by white, oxygen by red, sulfur by yellow and lithium is by purple dots.

Table C.1: DFT [b3pw91/6-311++g(d,p)] calculation for electrochemical reaction using DOL in an implicit solvation model

simple salt decomposition	ΔG(kcal/mol)
CF3-SO3(-1) + 2e(-1) = CF2-SO3(-2) + F(-1)	-116.59
CF3-SO3(-1) + 2e(-1) = CF3-SO2(-1) + O(-2)	-40.47
CF2-SO3(-2) + 1e(-1) = CF-SO3(-2) + F(-1)	-62.96
CF2-SO3(-2) + 2e(-1) = CF2-SO2(-2) +O(-2)	-34.77
CF-SO3(-1) + 3e(-1) = C-SO3(-3) + F(-1)	-59.64
CF-SO3(-1) + 4e(-1) = CF-SO2(-3) + O(-2)	-27.97
CF3-SO2(-1) + 2e(-1) = CF2-SO2(-2) + F(-1)	-110.89
CF3-SO2(-1) + 2e(-1) = CF3-SO(-2) + O(-2)	-43.78
CF2-SO2(-2) + 2e(-1) = CF-SO2(-3) + F(-1)	-56.17
CF2-SO2(-2) + 2e(-1) = CF2-SO(-2) + O(-2)	-39.07
CF-SO2(-3) + 1e(-1) = C-SO2(-2) + F(-1)	-63.85
CF-SO2(-3) + 2e(-1) = CF-SO(-2) + O(-2)	-35.83
CF3-SO(-1) + 2e(-1) = CF2-SO(-2) + F(-1)	-106.18
CF3-SO(-1) + 2e(-1) = CF3-S(-1) + O(-2)	-80.08
CF2-SO(-2) + 2e(-1) = CF-SO(-2) + F(-1)	-52.92
CF2-SO(-2) + 2e(-1) = CF2-S(-2) + O(-2)	-63.35
CF-SO(-2) + 1e(-1) = C-SO(-2) + F(-1)	-82.98
CF-SO(-2) + 2e(-1) = CF-S(-2) + O(-2)	-65.52
CF3-S(-1) + 2e(-1) = CF2-S(-2) + F(-1)	-89.45
CF2-S(-2) + 1e(-1) = CF-S(-2) + F(-1)	-55.09
CF-S(-2) + 2e(-1) = CS(-2) + F(-1)	-33.13
C-SO3(-3) + 2e(-1) = C-SO2(-3) + O(-2)	-32.19
C-SO2(-3) + 1e(-1) = C-SO(-2) + O(-2)	-54.96
C-SO(-2) + 2e(-1) = CS(-2) + O(-2)	-15.66
CF3-SO3(-1) + 2e(-1) = CF3(-1) + SO3(-2)	-118.12
CF3(-1) + 1e(-1) = CF2(-1) + F(-1)	-48.73
CF2(-1) + 1e(-1) = CF(-1) + F(-1)	-45.68
CF(-1) + 2e(-1) = C(-2) + F(-1)	-54.67
SO3(-2) + 2e(-1) = SO2(-2) + O(-2)	-10.82
SO2(-2) + 2e(-1) = SO(-2) + O(-2)	-42.30
SO(-2) + 2e(-1) = S(-2) + O(-2)	95.99
CF2-SO3(-2) + 1e(-1) = CF2(-1) + SO3(-2)	-50.26
CF-SO3(-2) +1e(-1) = CF(-1) + SO3(-2)	-32.98
C-SO3(-3) + 1e(-1) = C(-2) + SO3(-2)	-28.02
CF3-SO2(-1) + 2e(-1) = CF3(-1) + SO2(-2)	-88.47
CF2-SO2(-2) + 1e(-1) = CF2(-1) + SO2(-2)	-26.32
CF-SO2(-3) = CF(-1) + SO2(-2)	-15.83
C-SO2(-3) + 1e(-1) = C(-2) + SO2(-1)	-6.65
CF3-SO(-1) + 2e(-1) = CF3(-1) + SO(-2)	-86.98
CF2-SO(-2) + 1e(-1) = CF2(-1) + SO(-2)	-29.54
CF-SO(-2) + 1e(-1) = CF(-1) + SO(-2)	-22.30
C-SO(-2) + 2e(-1) = C(-4) + SO(-2)	6.01
Decomposition of solvent	**ΔG(kcal/mol)**
DOL +2e(-1) = O-CH2-O-CH2-CH2(-2)	-76.69
O-CH2-O-CH2-CH2(-2) = O-CH2-O(-2) + CH2CH2	-42.27
O-CH2-O(-2) + 1e(-1) = OCH2(-1) + O(-2)	10.66
OCH2(-1) + 3e- = CH2(-2) + O(-2)	-13.92
DME + 3e(-1) = CH3-O-CH2-CH2(-2) + OCH3(-1)	-93.25
CH3-O-CH2-CH2(-2) = OCH3(-1) + CH2CH2 + 1e(-1)	-43.73
OCH3(-1) + 2e(-1)= CH3(-1) + O(-2)	-13.90
DOX + 2e(-1) = O-CH2-CH2-O-CH2-CH2(-2)	-19.18
O-CH2-CH2-O-CH2-CH2(-2) = CH2-CH2 + O-CH2-CH2-O(-2)	-94.19
O-CH2-CH2-O(-2) + 2e(-1)= O-CH2-CH2(-2) + O(-2)	-4.83
O-CH2-CH2(-2) = CH2-CH2 + O(-2)	-3.89
OCH2CH2OCH2CH2F(-2) + 1e(-1) = OCH2(-1) + CH2OCH2CH2F(-2)	-0.36
CH2-O-CH2-CH2-F(-2) = CH2-CH2-F(-1) + OCH2(-1)	-8.75
CH2-CH2-F(-1) = CH2-CH2 + F(-1)	-117.01
EC + 3e- = O(-2) + 1,3-dioxolan-2-ylidene(-1)	-21.96

exchange mechanism	ΔG(kcal/mol)
CF-SO3(-3) = OCF-SO2(-1) + 2e(-1)	4.13
CF-SO2(-3) = OCF-SO(-1) + 2e(-1)	-24.80
CF-SO(-2) = OCF-S(-1) + 1e(-1)	-64.66
C-SO3(-3) = CO-SO2(-2) + 1e(-1)	-48.27
C-SO2(-3) = CO-SO(-2) + 1e(-1)	-57.61
C-SO(-2) = OCS(-1) + 1e(-1)	-31.61
CO-SO3(-2) = CO2-SO2(-2)	-77.88
Decomposition of exchanged species	**ΔG(kcal/mol)**
OCF-SO2(-1) + 2e(-1) = CO-SO2(-2) + F(-1)	-112.04
OCF-SO2(-1) + 2e(-1) = OCF-SO(-1) + O(-2)	-56.90
OCF-SO(-1) + 2e(-1) = CO-SO(-2) + F(-1)	-96.66
OCF-SO(-1) + 2e(-1) = OCF-S(-1) + O(-2)	-75.69
OCF-S(-1) +1e(-1)= OCS(-1) + F(-1)	-49.94
CO-SO2(-2) + 2e(-1)= CO-SO(-2) + O(-2)	-41.52
CO-SO(-2) + 1e(-1) = OCS(-1) + O(-2)	-28.97
OCF-SO2(-1) + 2e(-1) = OCF(-1) + SO2(-2)	-31.67
OCF-SO(-1) + 2e(-1) = OCF(-1) + SO(-2)	-17.07
OCF-S(-1) + 2e(-1) = OCF(-1) + S(-2)	-13.58
CO-SO2(-2) + 1e(-1) = CO(-1) + SO2(-2)	-29.09
CO-SO(-2) + 1e(-1) = CO(-1) + SO(-2)	-29.87
OCS(-1) + 2e(-1) = CO(-1) + S(-2)	-73.10
CO2-SO2(-2) + 2e(-1) = CO2(-2) + SO2(-2)	-45.65
CO2-SO2(-2) + 2e(-1) = CO2-SO(-2) + O(-2)	-44.78
CO2-SO(-2) + 2e(-1) = CO2(-2) + SO(-2)	-43.16
CO2-SO(-2) + 3e(-1) = CO2-S(-3) + O(-2)	-64.62
CO2-S(-3) -1e(-1) = CO2(-2) + S(-2)	-50.74
Reactions between solvent and salt	**ΔG(kcal/mol)**
DOL + CF3SO3(-1) + 3e(-1) = CF2SO3(-2) + HF + [-CH2CHOCH2O-](-1)	-71.79
DX + CF2SO3(-2) + 1e(-1) = OCH2CH2OCH2CH2F(-2) + OCFSO2(-1)	-32.33
DX + CO(-1) + 3e(-1) = CH2-CH2-O-CH2-CH2(-2) + CO2(-2)	-107.56
O-CH2-CH2(-2) + CO-SO2(-2) = CH2-CH2(-1) + CO-SO3(-2) + 1e(-1)	60.47
O-CH2-CH2(-2) + CO-SO2(-2) = CH2-CH2(-1) + CO2-SO2(-2) + 1e(-1)	-17.41
Organosufide polymerization and decomposition	**ΔG(kcal/mol)**
CF2-SO3(-2) + CS(-2) = C-S-CF2-SO3(-1) + 3e(-1)	142.95
C-S-CF2-SO3(-1) + 3e-= C-S-CF-SO3(-3) + F(-1)	-167.86
CF-SO3(-1) + CS(-2) = C-S-CF-SO3(-3)	38.05
C-SO3(-3) + CS(-2) = SO3-C-S-C(-3) + 2e(-1)	25.98
C-SO3(-3) + CS(-2) = SO3-C-C-S(-2) + 3e(-1)	-52.94
C-S-CF-SO3(-3) +1e(-1) = C-S-C-SO3(-3) + F(-1)	-71.71
C-S-C-SO3(-3) = S-C-C-SO3(-2) + 1e(-1)	-78.92
S-C-C-SO3(-2) + 2e(-1) = S-C-C-SO2(-2) + O(-2)	-32.69
S-C-C-SO2(-2) + 2e(-1) = SO-C-C-S(-2) + O(-2)	-41.90
SO-C-C-S(-2) + CS(-2) = SO-C-C-S-C-S(-4)	36.49

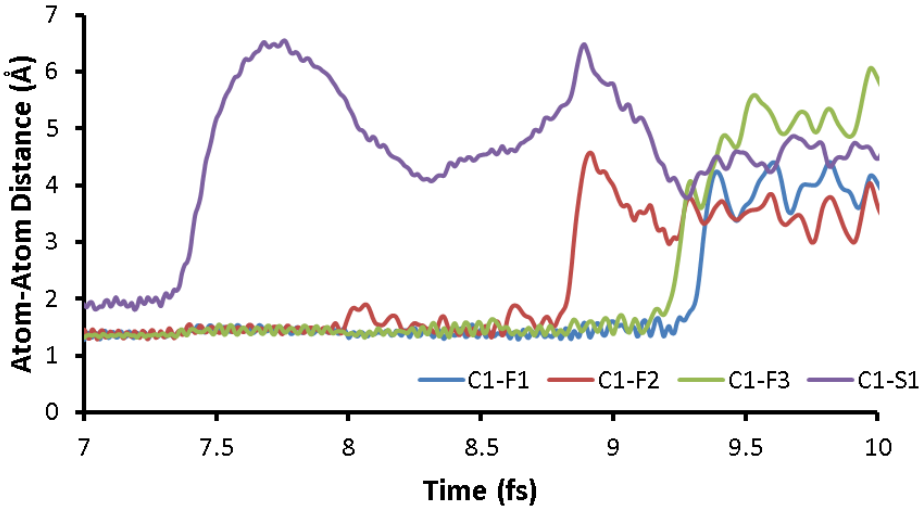

Figure A.18: Atom-Atom distance evolution over time of carbon-sulfur and carbon-fluorine bond from a triflate molecule.